



HAL
open science

Numerical study of dynamic relaxation methods and contribution to the modelling of inflatable lifejackets

Javier Rodriguez Garcia

► **To cite this version:**

Javier Rodriguez Garcia. Numerical study of dynamic relaxation methods and contribution to the modelling of inflatable lifejackets. Mechanical engineering [physics.class-ph]. Université de Bretagne Sud, 2011. English. NNT: . tel-00659669

HAL Id: tel-00659669

<https://theses.hal.science/tel-00659669>

Submitted on 13 Jan 2012

HAL is a multi-disciplinary open access archive for the deposit and dissemination of scientific research documents, whether they are published or not. The documents may come from teaching and research institutions in France or abroad, or from public or private research centers.

L'archive ouverte pluridisciplinaire **HAL**, est destinée au dépôt et à la diffusion de documents scientifiques de niveau recherche, publiés ou non, émanant des établissements d'enseignement et de recherche français ou étrangers, des laboratoires publics ou privés.



THESE / UNIVERSITE DE BRETAGNE-SUD
sous le sceau de l'Université européenne de Bretagne
pour obtenir le titre de
DOCTEUR DE L'UNIVERSITE DE BRETAGNE-SUD
Mention : Sciences de l'Ingénieur
Ecole doctorale SICMA

présentée par
Javier RODRIGUEZ GARCIA

Numerical study of dynamic relaxation methods and contribution to the modelling of inflatable lifejackets

Thèse soutenue le 7 Décembre 2011
devant le jury composé de :

Francisco CHINESTA
Professeur – EC Nantes / *président*

Karol MILLER
Professeur – University of Western Australia / *rapporteur*

David RODNEY
MdC HDR – INP Grenoble / *rapporteur*

Mohammed HJIAJ
Professeur – INSA Rennes / *rapporteur*

Anne JOLY
Ingénieur – Recherche & Développement, Plastimo / *invitée*

Bernard GENEAU
Ingénieur – Ex- Recherche & Développement, Plastimo / *invité*

Gérard RIO
Co-directeur de thèse
Jean-Marc CADOU
Co-directeur de thèse

*A mis padres,
que me lo han dado todo y a quienes debo mis logros,
y a mi abuelo,
al que he perdido en este período de mi vida
y que seguro que se sentiría orgulloso de mí*

Acknowledgements

First of all, I would like to deeply thank my two supervisors, Gérard Rio and Jean-Marc Cadou, for trusting me and giving me the chance of carrying out this work. I have found in them the best supervisors one could imagine: always helpful, dynamic and motivating. I will always be thankful for the knowledge they shared with me, their patience, their precious time and their dedication.

I want to thank *Région Bretagne* and *Conséil Général du Morbihan* for their financial support. Also, thanks to *Navimo/Plastimo* for help funding this research. And I am particularly thankful to Anne Joly and Bernard Genau, representing Pastimo, with whom I had periodical meetings, for their advise and for contributing with their industrial point of view.

Of course, I am profoundly thankful to my family, who despite the distance have always encouraged me to pursuit my goals. Specially my parents, who at the beginning disliked the idea of my departure, but who understand it better now and feel proud of me.

My thanks also go to all the LIMATB members for making the lab a second home for me. I could cite a long list of people that helped me in some way during my stay at this lab and that I could call friends rather than colleagues. Special thanks to the several office mates -now friends- that I have had during this period, for putting up with my many jokes: Tai Thu Nguyen, Faiza Boumediene, Pierre Tronet, Hamid Khelifi, Ji-Xing Meng, Jean-Marc Deux and Abderrahim El Ouakili.

I am also grateful to all the friends that filled my life at Lorient these past years with good moments. There is an endless list of people that I could cite here, from the very first friends as Gijo Raj, Maxence Legrand, Meysam Hamid-Pourian or Farnaz Gorjizadeh to the multiple "generations" of Erasmus I have spent some of my time with: Sara, Alberto, Inés, Sabela, Dimitri, Antonio, Yanira, Samuel, Mario, Diego, Kristina, Dilek, Frederik, Juanma, Laura, Ugur, John, Raquel, and so on...

Last but not least, I address special thanks to Almudena Vargas, with whom (and also thanks to whom), during the past two years, I have had some of the best times of my life.

Abstract

Dynamic relaxation (DR) is a numerical method introduced in 1965 by A.S. Day in the book "The Engineer". From 1983, with the works presented by P. Underwood, it became more and more used. Since then, many applications were found, and several authors presented different improvements on the method in order to optimize the calculations. Nowadays, its use is widely spread in fields as structural dynamics (particularly in form-finding), geomechanics or biomechanics.

When using DR in numerical simulations, researchers followed two different paths in the choice of a damping strategy for the oscillations: some used DR combined with a viscous damping and others used DR combined with kinetic damping. However, it is difficult to find comparisons between both methods to help deciding whether one is better than the other for a particular application.

Focused in the field of form-finding of thin structures, the main objective of this thesis is to make a contribution to the development of DR methods and a review of the existing DR methods in order to compare them. Therefore, a scientific paper is presented in this thesis comparing different DR methods with both kinetic and viscous damping in the case of form-finding of inflatable structures. Also, another paper is detailed where an extension for the DR method with kinetic damping is proposed.

Then, as an application for the studied DR methods, a contribution to the modelling of inflatable lifejackets will be presented. The aim of this part of the work is to present some contributions to the creation of a numerical tool permitting to test the functioning of an inflatable lifejacket by means of Finite Elements calculations.

This work covers the creation of a parameterized mannequin, a rough characterization of the involved technic textile, improvements in the numerical simulation of the inflation of the lifejacket using the DR method, and also a first approach to the water dynamics and contact mechanics that will be involved in the final simulation.

Keywords: Form-finding, dynamic relaxation, viscous damping, kinetic damping, inflatable structures, inflatable lifejackets

Résumé

La Relaxation Dynamique (RD) est une méthode numérique présentée en 1965 par A.S. Day dans l'ouvrage "The Engineer". Depuis 1983, avec les travaux présentés par P. Underwood, la méthode est de plus en plus utilisée. Depuis ces travaux fondateurs, la méthode de RD a trouvé de nombreuses applications, et plusieurs auteurs ont introduit différentes améliorations de la méthode en cherchant l'optimisation des calculs. Désormais, son utilisation s'est largement étendue aux domaines tels que la dynamique des structures (particulièrement la recherche de forme), la geomécanique ou la biomécanique.

Dans le cadre de l'utilisation de la RD les chercheurs ont suivi deux chemins différents pour le choix d'une stratégie d'amortissement des oscillations: certains ont utilisé la RD combinée avec un amortissement visqueux et d'autres ont utilisé la RD combinée avec un amortissement cinétique. Néanmoins, très peu de comparaisons entre ces deux méthodes ont été exposées ayant par but d'aider à choisir l'une ou l'autre pour une application en particulier.

Focalisés dans la recherche de forme de structures minces, le principal objectif de cette thèse est d'apporter une contribution au développement des méthodes de RD parallèlement à une revue des méthodes existantes en vue de les comparer. Un premier article scientifique est ainsi détaillé dans ce travail en comparant les différentes méthodes de RD avec les deux types d'amortissement, cinétique et visqueux, pour le cas particulier de la recherche de forme de structures gonflables. Puis un second papier est décrit, où une extension pour la méthode de RD avec amortissement cinétique est proposée.

En tant qu'application des méthodes de RD étudiées, une contribution à la modélisation des gilets de sauvetage gonflables est exposée. Le but de cette partie de la thèse est d'introduire quelques contributions à la création d'un outil numérique permettant de tester le fonctionnement d'un gilet de sauvetage gonflable en situation en utilisant la méthode des Eléments Finis.

Ce travail comprend la création d'un mannequin paramétré, une caractérisation grossière du textile technique impliqué, des améliorations concernant la simulation numérique du gonflage du gilet en utilisant la méthode de RD, et finalement une première approche à la dynamique de l'eau et la mécanique du contact qui seront présents dans la simulation globale.

Keywords: Recherche de forme, relaxation dynamique, amortissement visqueux, amortissement cinétique, structures gonflables, gilets de sauvetage gonflables

Contents

1	Introduction	11
1.1	Background and motivation	11
1.2	Industrial and academic objectives	13
1.3	Thesis overview	15
2	FE Software and validation	17
2.1	FE software	17
2.1.1	Introduction	17
2.1.2	Algorithms	17
2.2	Validation	18
2.2.1	Geometry and calculation parameters	19
2.2.2	Analytical calculation	20
2.2.3	Herezh++ calculation and comparison with analytical results . . .	26
2.2.4	Conclusions	28
3	Dynamic Relaxation Method	31
3.1	Introduction	31
3.2	Numerical study of dynamic relaxation with kinetic damping applied to inflatable fabric structures with extensions for 3D solid element and non-linear behavior	33
3.2.1	Introduction	33
3.2.2	Dynamic Relaxation Method	34
3.2.3	Numerical case studies	42
3.2.4	Conclusions and discussion	50
3.2.5	Acknowledgements	51
3.3	Comparison of several dynamic relaxation methods in the case of large displacements of membrane structures	52
3.3.1	Introduction	52
3.3.2	DR methods	53
3.3.3	Numerical case studies	61
3.3.4	Conclusions and discussion	68
3.3.5	Acknowledgements	69

4	3D measuring	71
4.1	Introduction	71
4.2	Description of the devices used in the measuring	72
4.3	System calibration and sample preparation	74
4.4	Limitations and objectives of the experimentation	76
4.5	Numerical simulation	77
4.6	Measuring results	78
4.7	Conclusions	80
5	Tensile tests on fabric	83
5.1	Introduction	83
5.2	Technic textile	83
5.3	Tensile test preparation	85
5.4	Results	87
5.5	Conclusions and discussion	87
6	Human body model	91
6.1	Introduction	91
6.2	Software's choice	92
6.3	Geometric considerations	93
6.4	Development in Gmsh	95
6.5	C++ programming and testing	96
6.6	Dummy's design improving	99
	6.6.1 General dimensions	99
	6.6.2 Joints	99
6.7	Conclusions and discussion	103
7	Lifejacket modeling and contact mechanics	105
7.1	Introduction	105
7.2	Creation and meshing of the lifejacket model	106
7.3	Numerical simulation of inflation	107
7.4	Contact mechanics	109
	7.4.1 How contact is implemented	109
	7.4.2 Numerical examples of contact (validation tests)	112
	7.4.3 Application to the case of lifejacket and mannequin	113
7.5	Conclusions and discussion	115
8	Water modelling	119
8.1	Introduction	119
8.2	Hydrostatic pressure	120
8.3	Hydrodynamic forces	121
8.4	Added mass and impact force	125
	8.4.1 Impact force	126
8.5	Conclusions and discussion	133

9	General conclusion and perspectives	135
9.1	Conclusions	135
9.2	Perspectives	136

Chapter 1

Introduction

1.1 Background and motivation

Numerical simulations using finite elements are widely used in the industry. They allow to test all kind of products before their manufacturing in order to detect defects and to prevent errors in the first stages of the design process. Also, numerical simulations allow to optimize the design and operation conditions of all kind of devices or pieces, and they have a particular interest when the behavior of the studied element is governed by complex equations that cannot be solved by using analytical methods.

Nowadays, any competitive enterprise needs to use the numerical simulations on their products or processes to predict and correct eventual problems that could appear. The field of application of the numerical simulations is very wide, and it can go from the simulation of a small piece of a mechanism to a large mechanical structure or even a human organ in a biomedical application.

The most spread application of FE simulations is the design of products. They allow to virtually test prototypes, being therefore possible to leave for the final stage the development and testing, once the ideal configuration has been numerically calculated.

Plastimo is an enterprise located in Lorient (France) that designs and manufactures all kind of boating equipments. Among them, they also manufacture inflatable lifejackets, with different buoyancy aids (100N, 150N and 275N).

Since July 1st, 1995, all lifejackets and buoyancy aids must comply with the European Standards (CEN), to get the CE mark which testifies that the buoyancy aid has successfully passed all the tests and that materials and fabrics used also comply with the European standard. For 100N lifejackets, the normative to comply is EN395, EN396 is for 150N lifejackets, and EN399 for 275N lifejackets.

The inflation of these lifejackets can be triggered in 3 ways:

- **Oral inflation** : Possible in all Plastimo's lifejackets; this way allows the user to "pump up".
- **Manual inflation** : firing the CO_2 gas cylinder is done by pulling a cord handle.



Figure 1.1: Inflatable lifejackets manufactured by Plastimo

- **Automatic inflation** : the lifejacket inflates automatically on immersion in the water.

In the manufacturing of these lifejackets, Plastimo carries out tests to check if they work adequately. For this, they set the lifejacket on a mannequin, and they drop it into a pool. But they found that this is far from being a good testing procedure, mainly due to lack of repeatability. This is because there are a lot of parameters that are impossible or very difficult to control, such as the initial position when dropped into water, the morphology (they just have one kind of mannequin), and so on... Also, it is an uncomfortable and expensive test (because not only they waste a lifejacket; they also need to have access of a pool, and several people carrying out the tests).

Due to all these reasons, they thought of carrying out the tests by means of a computer, in a numerical simulation. This way, all parameters could be controlled, and any kind of morphology could be, theoretically, made. Therefore, this is the context that motivated this work.

Three kinds of lifejacket manufactured by Plastimo were mentioned. In this paper we address the automatic one. This means that the person wearing it might be unconscious, and due to this, he/she would not move by him/herself. In other case, the numerical simulation would be more complex (and time consuming) and eventually not possible since random movements cannot be predicted for any single person.

The idea of Plastimo is to be able to simulate all the testing procedure with the maximum number of parameters included and to check the good working of a certain conception of lifejacket. The agents involved in the simulation will be: the mannequin, the inflatable lifejacket and water. The simulation they intend to carry out includes the following steps :

- The mannequin, fully parameterized (any morphology should be feasible), porting an inflatable lifejacket, falls freely into water in a random position
- The mannequin reaches the water, and he is subjected to a water impact and hydrostatic/hydrodynamic forces

- The lifejacket inflates inside water in less than a specified maximum time
- The mannequin is expelled to the surface, with its airways upwards and outside the water

Because there are several physical phenomena, such as the contact problem, the forces created by the fluid, etc, the work must be divided in several parts. This work will focus specially in the numerical simulation of the inflation. Also, the creation of a parameterized mannequin, a rough characterization of the used technic textile and a first approach to the water dynamics and the contact mechanics will be covered.

1.2 Industrial and academic objectives

The industrial objective, as indicated previously, is to finally obtain a tool that allows to check the functioning of any kind of lifejacket being worn by any kind of person. It is a very ambitious objective for a 3-year thesis, so all the possible advancements are welcomed. It can set the basis for a future complete tool for simulating the whole process of lifejackets' testing.

It is important to remark that *the final aim is not to obtain a numerical tool that reproduces exactly the reality*. That would be currently impossible, since the real conditions of a person falling into water change if he/she feels stressed during the fall and reacts in certain way, if there are a certain kind of waves, or if the person wears a particular brand of boots, etc. The aim of the numerical tool is to allow to *observe the tendencies* in the behavior of eventual different models of lifejackets, by keeping all the rest of the testing conditions fixed. However, even if we are not trying to reproduce exactly the reality, we try to include as many physical factors involved as possible. This way, the tool would permit for example, to check how a modification in the lifejacket's shape could affect the final result.

This work can be considered as a continuation of the thesis work of Julien Troufflard [1], who made an efficient tool to mesh and simulate the inflation of membrane structures. He created a tool that is currently being used by Plastimo, serving to the dimensioning of lifejackets. This tool had to be simple so Plastimo's staff with a rough knowledge in finite elements could use it. But while his aim was to create a tool usable in the industry, the aim of this work is *mainly academic* but keeping in mind that the background is the look for an industrial applicability: establishing the basis to create a more complex numerical tool.

Besides the fact of contributing to the creation of a tool useful for the industry, there are some interesting research possibilities, and we particularly focused on the improvement of the simulation of membrane inflatable structures. The simulation of a lifejacket's inflation is probably the most time-consuming part on the global simulation. That is why it seemed interesting to work on that point, by doing some research in that field.

Nowadays, the field of form-finding of membrane structures is booming. There are two main branches: the form-finding of structural membranes and the form-finding of inflatable structures.

In the case of structural membranes, they are employed due to its lightness and/or aesthetic characteristics in the façades of modern buildings, sports stadiums' covers, etc... (see figure 1.2 for some examples).



Figure 1.2: From left to right: Burj Al Arab Hotel in Dubai (with a textile façade); the Beijing's Water Cube; the Moses Mabhida stadium in Durban, South Africa; and the 2km length textile-covered entrance to the EXPO in Shanghai 2010

Concerning the form-finding of inflatable structures, they are widely used in the military and aerospace industry (temporary hangars for airplanes' repairing, removable modules for the ISS, etc, are some examples), pavilions for all kind of events, emergency sealing of liquid's pipes, and even in newer recent applications, as Tensairity[®] structures, with architectural functions (see figure 1.3).

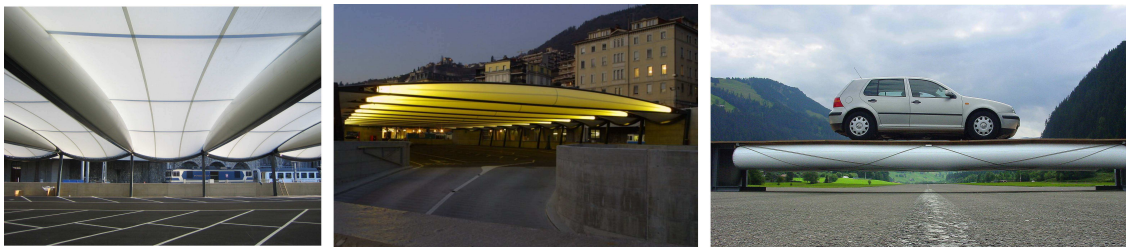


Figure 1.3: Sample Tensairity[®] applications. Left and center: parking cover (sources: canobbio.com and tensinet.com); Right: deployable bridge (Source: Buildair)

All these applications are becoming more and more complex, and the need for fast and efficient calculations is becoming more important. Troufflard, in his thesis work, found it interesting to use a particular method called *dynamic relaxation*, that he showed to be efficient and useful in the simulation on inflatable structures. However, his tool was limited to a single dynamic relaxation method, only one type of finite element, only an elastic behavior, and with the only final objective of finding the final form of the inflated lifejacket. Therefore, this method still offered some paths to be explored and fully exploited in order to improve it. This thesis work provides some new interesting

improvements for a particular type of dynamic relaxation (where it is extended to any type of element and any kind of behavior), and a comparison of several existing dynamic relaxation methods. Actually, two scientific papers are issued from this work, detailing this improvements.

1.3 Thesis overview

This thesis work covers the following work:

In chapter 2, the software Herezh++ used in our simulations will be presented. Then, since it is an academic software (under development), a validation of an inflation calculation is showed: the calculation of the radius' variation in the inflation of a sphere is made. The sphere is meshed with different sizes of triangular membrane elements. To compare it with theoretical results, an analytical study is made.

In chapter 3, the main contribution of this thesis work is presented: the improvements on the dynamic relaxation method. First of all, the dynamic relaxation method is presented, and then, the two issued papers are included. In the first one, two new proposals for a type of dynamic relaxation are presented and validated, and in the second one, our proposed methods are compared to other existing types of dynamic relaxation in several case studies for the particular case of membrane structures.

In chapter 4, in order to check the validity of the model used for the fabric in simulations, a 3D optic measuring is carried out during the inflation of a simple shape, by means of two high speed cameras and an image correlation software. The result is compared with the simulations made in our finite elements software.

In chapter 5, some experimental tests are made on the technic textile provided by Plastimo, in order to characterize it and to roughly determine a law of behavior. There, the microstructure of the material is observed, and different types of tensile tests are carried out by means of a tensile test machine along the different orientations of the technic textile.

In chapter 6, a detailed review of the creation of a parameterized mannequin in C++ is presented. The software's choice is reasoned and all the creation procedure is commented, including the difficulties found and the limitations of the model. Then, some improvement proposals are presented.

In chapter 7, we present the application of dynamic relaxation to the lifejacket manufactured by Plastimo. Then, after a brief presentation of the contact mechanics in Herezh++, the inflation of the lifejacket is made by dynamic relaxation and this inflation is combined with contact against different surfaces.

In chapter 8, a first approach on water impact and hydrodynamic/hydrostatic forces are shown. Hydrostatic pressure and hydrodynamic forces' implementation in Herezh++ are presented and justified. A review of the literature concerning the water impact is also presented.

Finally, in chapter 9, the general conclusions and perspectives are presented.

Chapter 2

FE Software and validation

2.1 FE software

2.1.1 Introduction

In order to carry out all the simulations in this work, the academic C++ finite elements software Herezh++ [18] will be used. For the pre- and post-processing, Gmsh [81] will be also used, since Herezh++ allows to import/export the data particularly easily, in order to work with it in Gmsh.

Herezh++ allows to work in large displacements and large deformations, with 1D, 2D or 3D elements, and with virtually any law of behavior (a set of laws is already implemented, but more laws of behavior can be added: external procedures like Abaqus' UMAT can be used, and they can be coded in any language [2]).

Concerning the calculation algorithms, several different algorithms are available in Herezh++, and all along this work, two temporal advancement schemes will be used: the Tchamwa-Wielgosz' scheme [5], that will be used only in the validation of the inflation in Herezh++ and when real dynamics are required (such as the calculations concerning water, where obtaining real times is important), and the Centered Finite Differences scheme (used within Dynamic Relaxation Algorithm). Both of them are explicit schemes, because this works covers the study of membrane structures, that are unstable, and implicit algorithms would lead to divergence (this is further explained later on, in the papers).

2.1.2 Algorithms

2.1.2.1 Dynamic Relaxation: Centered Finite Differences (CFD)

The dynamic relaxation algorithm is based on the Centered Finite Differences (CFD) method for the temporal advancement. This is a classic explicit method used in dynamic calculations. We can write the general discretized vectorial equation of dynamics as:

$$[M]\ddot{X}_n + [C]\dot{X}_n + R(X_n, \dot{X}_n) = 0 \quad (2.1)$$

where $[M]$ is the mass matrix, $[C]$ is the explicit (like artificial) damping matrix, \ddot{X}_n , \dot{X}_n , and X_n are the acceleration, velocity and position of the nodes at the n th increment, and $R(X_n, \dot{X}_n)$ represents the residual of internal and external forces, depending only in the nodes' positions. Also, the internal forces could include a viscous part (this would be the case of a viscoelastic law of behavior, for example).

Given this equation, and supposing no C matrix acts (to simplify the presentation), the CFD scheme would give the following approaches, in function of the time step Δt :

$$\begin{aligned}\ddot{X}_n &= -[M]^{-1}R(X_n, \dot{X}_n) \\ \dot{X}_{n+\frac{1}{2}} &= \dot{X}_{n-\frac{1}{2}} + \Delta t \ddot{X}_n \\ X_{n+1} &= X_n + \Delta t \dot{X}_{n+\frac{1}{2}}\end{aligned}\tag{2.2}$$

2.1.2.2 Tchamwa-Wielgosz

The Tchamwa-Wielgosz scheme is usually used when a filtering of the high frequencies of vibration is convenient (in rapid dynamics, for example). We are not exactly in the case of rapid dynamics, but the algorithm showed a good efficiency in our calculations. A comprehensive review can be read in the references [3, 4, 5, 6] The algorithm can be written as:

$$\begin{aligned}[M]\ddot{X}_{n+1} + R_{int}(X_{n+1}, \dot{X}_{n+1}) &= R_{ext}(X_{n+1}, \dot{X}_{n+1}) \\ \dot{X}_{n+1} &= \dot{X}_n + \Delta t \ddot{X}_n \\ X_{n+1} &= X_n + \Delta t \dot{X}_n + \Phi \Delta t^2 \ddot{X}_n\end{aligned}\tag{2.3}$$

where Φ is a parameter that controls the numerical damping of the high frequencies, and it can go from 1 to ∞ . A value of $\Phi = 1$ makes this algorithm equivalent to the CFD method. A value of $\Phi = 1.03$ is typically used since the closer we are to 1, the closer we are to a second order precision (typical of DFC). Thus, a value away from 1 makes the precision decrease. a very big value can lead to a loss in the precision.

2.2 Validation

Since Herezh++ is an academic software under development, and since this thesis work is focused in the form-finding of inflatable structures, it would be convenient in a first step to present a validation of some example results obtained when calculating the inflation of a simple known geometry. With this aim, we decided to calculate the inflation of a sphere, since the final shape can also be easily calculated analytically.

For the validation, only the Tchamwa-Wielgosz scheme will be used. Our intention is to validate the inflation calculations with an algorithm close to the real dynamics, that is the case of Tchamwa-Wielgosz' one. Concerning the validation when using a Dynamic Relaxation algorithmn (based on CFD scheme), it will be presented in Chapter 3, in the second paper.

2.2.1 Geometry and calculation parameters

The mesh to be tested is a sphere (chosen because it is a geometry simple enough to be able to obtain an analytical final result), which is going to be generated by means of Gmsh using its graphical interface. For simplicity, the three possible symmetries in a sphere are considered, modeling this way just an eighth of the sphere, as shown in the figure 2.1. This allows to save calculation time while giving the same final results.

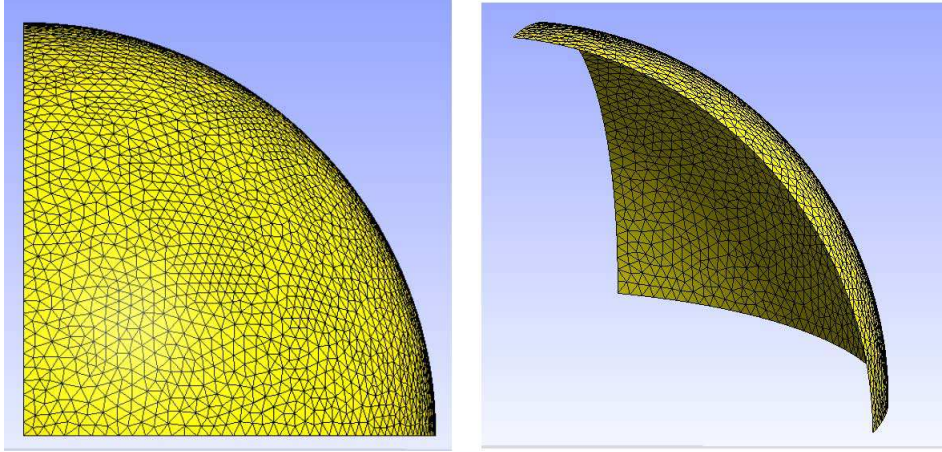


Figure 2.1: Eighth of sphere modeled in Gmsh

The chosen geometric and physical parameters of the sphere were the following (the choices were made in order to be near to a lifejacket's characteristics):

- **Radius:** $r=300$ mm
- **Thickness:** $e=0.27$ mm
- **Density:** $\rho = 10^{-9} \text{ ton/mm}^3 = 1\text{kg/dm}^3$
- **Young's modulus:** $E=150, 600$ and 3000 MPa (E, 4E and 20E)
- **Poisson's ratio:** $\nu =0.41$

For the validation to be achieved, different tests were made, by varying the elements' size (to observe the impact of the discretization), the Young's modulus (to observe the influence of the material) and also the internal pressure (in order to test with different deformations). Concerning the mesh elements' size, four different sizes were tested. Also, for each one of the meshes, three different Young's moduli were used. And finally, for each combination of mesh size and Young's modulus, three different pressures were applied to carry out the inflation. These applied pressures also comply with the order of magnitude of pressure in inflatable lifejackets. The different combinations are shown in the table 2.1.

Meshes (n° elements)	Young's modules (MPa)	Pressures (MPa)
41 , 333, 3305, 13210	150	0.01
		0.015
		0.02
	600	0.01
		0.015
		0.02
	3000	0.01
		0.015
		0.02

Table 2.1: Different tests made

The calculation was made in explicit dynamics by means of the dissipative scheme of Tchamwa-Wielgoz, with a $\phi = 1.3$ (damping factor value that leads to a big damping). Also, to try to reach faster a final equilibrium solution, a kinetic relaxation method was employed, with an stopping criterion based on the static residual (the balance of internal and external static forces) and a precision of 10^{-4} . The four different meshes can be observed in the figure 2.2

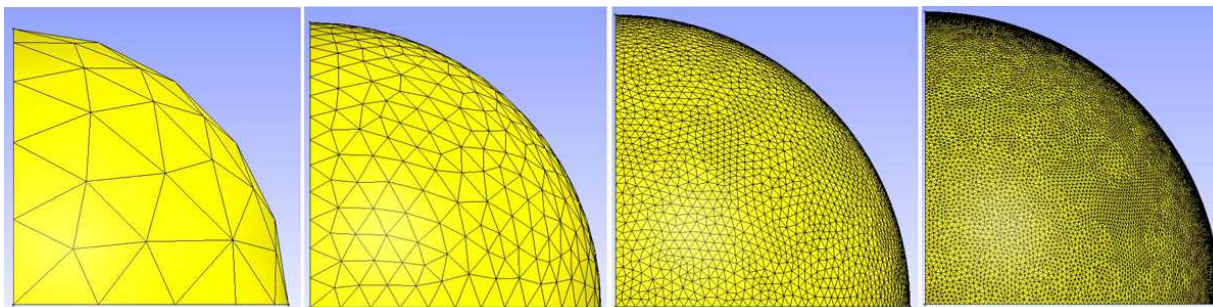


Figure 2.2: View of the four different meshes employed in the simulations

2.2.2 Analytical calculation

For the theoretical calculation, we can be based on the simple expressions for the calculation of spherical pressure vessels presented by the Colorado State University [7]. From that simple presented equations, we will carry out our own analytical development to get to more complex expressions, considering large deformations and a decrease of walls' thickness.

Slicing a sphere in a half and retaining one of the halves (e.g. the superior one), we consider the forces applied on it :

- **Internal pressure:** The internal pressure P acts in the plane surface $A = \pi r^2$

corresponding to the circular cut of the sphere projected in the cutting plane; r represents the sphere radius.

- **Stress which counteract:** The stress σ^{rr} counteracting the internal pressure acts in the surface $A = 2\pi r e$ ¹ being e the thickness of the sphere.

Knowing this, we can say:

$$P(\pi r^2) = \sigma^{rr}(2\pi r e) \quad (2.4)$$

obtaining the value of the stress:

$$\sigma^{rr} = \frac{Pr}{2e} \quad (2.5)$$

It is possible to cut the sphere in half using many different planes, but after each cut the analysis would be the same; a spherical pressure vessel is under "uniform stress".

If we consider now the strain ϵ^{rr} in 3D for a Hooke's behavior:

$$\epsilon^{rr} = \frac{1}{E}(\sigma^{rr} - \nu\sigma^{tt} - \nu\sigma^{hh}) \quad (2.6)$$

Since the values σ^{rr} and σ^{tt} are equivalent in the case of a sphere, and being σ^{hh} negligible ($\approx P, \ll \sigma^{rr}$), we finally obtain for the strain :

$$\epsilon^{rr} = \frac{1 - \nu}{E} \frac{Pr}{2e} \quad (2.7)$$

At this point, we could calculate the volume of the sphere under pressure by considering the deformation produced in it. The precision with which we would like to calculate the new volume/radius depends on if we calculate considering small deformations or not, and if thickness decreases or not. So we can distinguish four cases :

- Small deformation and constant thickness
- Large deformation and constant thickness
- Small deformation and variable thickness
- Large deformation and variable thickness

It is obvious that the most precise solution would be obtained with the last case, but it may be interesting to make an analytical development of all the possible situations.

¹We consider thin walls; otherwise the formule should be $A = \pi((r + e/2)^2 - (r - e/2)^2)$

2.2.2.1 Small deformations. Constant wall thickness e

After the application of the internal pressure, the radius of the sphere changes from a value r to a new bigger value \hat{r} . So we can write, for small deformations (and constant e):

$$\frac{\hat{r} - r}{r} \approx \frac{(1 - \nu)Pr}{2eE} \implies \hat{r} = r \left(1 + \frac{(1 - \nu)Pr}{2eE} \right) \quad (2.8)$$

And with that expression, given that we know all the parameters involved, it would be possible to calculate the new radius, and consequently, the new volume.

2.2.2.2 Large deformations. Constant wall thickness \hat{e}

Here we use the Almansi strain to calculate the new radius. We use Almansi strain because it's the one implemented in Herezh++ along with Cauchy stress. Again, the new one is denoted by \hat{r} , and \hat{e} denotes the thickness after the deformation (after inflation, the final thickness). We can write, being based in the equation 2.7 :

$$\frac{1}{2} \left(\frac{\hat{r}^2 - r^2}{\hat{r}^2} \right) = \frac{(1 - \nu)P\hat{r}}{2\hat{e}E} \quad (2.9)$$

One can note that in the case of finite deformations, a specific choice of a measure of deformation influences the result. Simplifying the expression 2.9, we obtain:

$$1 - \left(\frac{r}{\hat{r}} \right)^2 = \frac{(1 - \nu)P\hat{r}}{\hat{e}E} \implies \frac{r}{\hat{r}} = \left(1 - \frac{(1 - \nu)P\hat{r}}{\hat{e}E} \right)^{\frac{1}{2}}$$

$$\frac{\hat{r}}{r} = \left(1 - \frac{(1 - \nu)P\hat{r}}{\hat{e}E} \right)^{-\frac{1}{2}}$$

so the radius \hat{r} :

$$\hat{r} = r \left(1 - \frac{(1 - \nu)P\hat{r}}{\hat{e}E} \right)^{-\frac{1}{2}} \quad (2.10)$$

2.2.2.3 Small deformations. Variable wall thickness \hat{e}

When the sphere is under internal pressure, it inflates and its material stretches. This deformation of the material leads to a narrowing of the walls, which could be important in the final result (the resisting section decreases).

The new "real" thickness \hat{e} (instead of the initial one e) can be calculated as following for the case of small thickness.

Working in polar coordinates, we can say that the stress has the value

$$\sigma^{rr} = \frac{Pr}{2e} = \sigma^{\theta\theta} \quad (2.11)$$

And considering this, we can obtain for the strain value

$$\epsilon^{zz} = \frac{1}{E} (P - \nu\sigma^{rr} - \nu\sigma^{\theta\theta}) = \frac{1}{E} (P - 2\nu\sigma^{rr}) \approx \frac{\hat{e} - e}{e} \quad (2.12)$$

being e the initial wall thickness and \hat{e} the final one. Simplifying this expression, and replacing σ^{rr} for its value defined in equation 2.11, and knowing that $e \approx \hat{e}$ (since we are in small deformations) :

$$\epsilon^{zz} = \frac{P}{E} \left(1 - \frac{2\nu r}{2e}\right) = \frac{\hat{e} - e}{e} \approx \frac{P}{E} \left(1 - \frac{\nu r}{e}\right) \quad (2.13)$$

This leads to :

$$\Delta e \approx \frac{P}{E} (e - \nu r) \quad (2.14)$$

so we can estimate the new thickness by :

$$\hat{e} = e + \Delta e = e + \frac{P}{E} (e - \nu r) \quad (2.15)$$

2.2.2.4 Large deformations. Variable wall thickness \hat{e}

In this case, the analysis is similar to the previous one, but considering now Almansi strain instead of the one for small deformations.

$$\frac{1}{E} \left(P - 2\nu \frac{P\hat{r}}{2\hat{e}} \right) = \frac{1}{2} \left(1 - \frac{e^2}{\hat{e}^2} \right) \quad (2.16)$$

Simplifying to obtain a solution:

$$\begin{aligned} \frac{P}{E} \left(1 - \frac{2\nu\hat{r}}{2\hat{e}} \right) &= \frac{1}{2} - \frac{1}{2} \left(\frac{e}{\hat{e}} \right)^2 \\ \frac{1}{2} \left(\frac{e}{\hat{e}} \right)^2 - \frac{P\nu\hat{r}}{Ee} \left(\frac{e}{\hat{e}} \right) + \left(\frac{P}{E} - \frac{1}{2} \right) &= 0 \end{aligned} \quad (2.17)$$

If we would like to solve this, we can make the change

$$x = \frac{e}{\hat{e}}$$

we could solve the equation 2.17 simply as a second-order polynomial equation in a single variable x :

$$x^2 - \left(\frac{2P\nu\hat{r}}{Ee} \right) x + \left(\frac{2P}{E} - 1 \right) = 0$$

where x has the value :

$$x = \frac{\frac{2P\nu\hat{r}}{Ee} \pm \sqrt{\left(\frac{2P\nu\hat{r}}{Ee}\right)^2 - 4\left(\frac{2P}{E} - 1\right)}}{2}$$

So we obtain the new thickness e to use in the calculations as :

$$\hat{e} = \frac{2e}{\frac{2P\nu\hat{r}}{Ee} \pm \sqrt{\left(\frac{2P\nu\hat{r}}{Ee}\right)^2 - 4\left(\frac{2P}{E} - 1\right)}} \quad (2.18)$$

2.2.2.5 Calculation

After a first calculation in Herezh++ in the most unfavorable (in terms of precision) conditions, i.e., the most simple mesh(41 elements), with the highest loading pressure (0.02 MPa) and the lowest Young's modulus (150 MPa), it has been observed that deformation is quite important. Due to this, for the theoretical calculation, we are going to use the large deformations' formulae.

Since deformations are large, the thickness of the wall will decrease (a priori) importantly, so we will calculate using the variable \hat{e} 's theory. Due to the fact that the thickness of the walls decreases as the radius increases, we cannot solve the problem just by solving two equations separately, one for radius and another one for thickness. Instead of this, it is necessary to solve a non-linear system of two equations, which are 2.9 and 2.17.

From these equations, the unknowns are \hat{e} and \hat{r} . For solving the system, we use a classical Newton's method. We are interested only in \hat{r} , but it is necessary to obtain the \hat{e} in order to have it at each iteration to re-calculate the radius.

To solve the system, we used the software Scilab, by coding a short program that calculates the solution by iterating the Newton's method (see appendix A):

$$(X_{i+1}) = (X_i) + [K]^{-1}(R)$$

where the stiffness matrix is :

$$[K] = - \begin{bmatrix} \frac{r^2}{\hat{r}^3} - \frac{(1-\nu)P}{2\hat{e}E} & \frac{(1-\nu)P\hat{r}}{2E\hat{e}^2} \\ -\frac{P\nu}{E\hat{e}} & -\frac{e^2}{\hat{e}^3} + \frac{P\nu\hat{r}}{E\hat{e}^2} \end{bmatrix}$$

and the residual vector is:

$$(R) = \begin{pmatrix} \frac{1}{2} - \frac{r^2}{2\hat{r}^2} - \frac{(1-\nu)P\hat{r}}{2\hat{e}E} \\ \frac{e^2}{2\hat{e}^2} - \frac{P\nu\hat{r}}{E\hat{e}} + \left(\frac{P}{E} - \frac{1}{2}\right) \end{pmatrix}$$

The solutions obtained in the vector (X) , corresponding to the final radius \hat{r} and the final thickness \hat{e} are taken after reaching a certain indicated precision (10^{-12} for the residual). We could observe that 4 iterations with the Newton-Raphson's method were enough to reach the desired precision.

After calculating by Scilab for each one of the cases, the results are shown in the table 2.2:

<i>E = 150 MPa</i>		
Pressure (MPa)	Final radius \hat{r} (mm)	Final thickness \hat{e} (mm)
0,01	307,1734	0,2617
0,015	311,3056	0,2576
0,02	315,8958	0,2533
<i>E = 600 MPa</i>		
Pressure (MPa)	Final radius \hat{r} (mm)	Final thickness \hat{e} (mm)
0,01	301,6746	0,2679
0,015	302,5396	0,26692
0,02	303,4242	0,2659
<i>E = 3000 MPa</i>		
Pressure (MPa)	Final radius \hat{r} (mm)	Final thickness \hat{e} (mm)
0,01	300,3292	0,2696
0,015	300,4948	0,2694
0,02	300,6612	0,2692

Table 2.2: Theoretical results of final radius and wall's thickness after inflation

2.2.3 Herezh++ calculation and comparison with analytical results

After making all the calculations in Herezh++, the results are given by two ways: the first one, is the Gmsh format, with which we can observe visually the coherence of the result (example shown in the figure 2.3). The second one, a .maple file from where it is possible to obtain the numerical results.

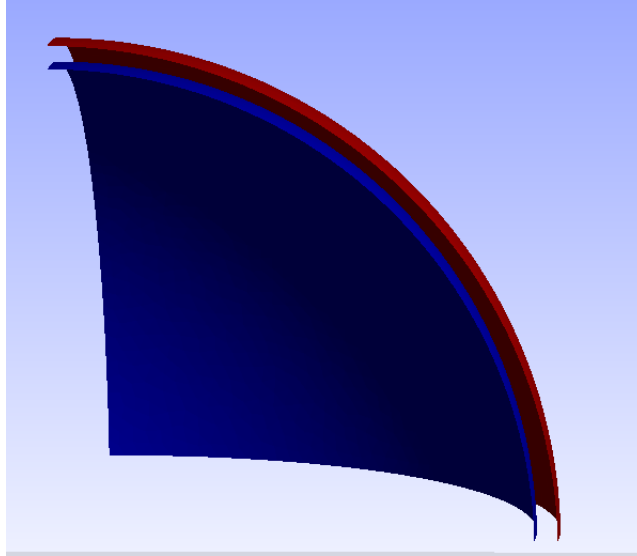


Figure 2.3: Initial (blue) and final (red) shape of the sphere used in the finite elements calculation, for the mesh of 3305 elements, with $E=150\text{MPa}$ and $P=0.02\text{MPa}$

The idea for the validation is to compare the results obtained with Herezh++ to the analytical results. We are just going to compare the final radius, because this is the main parameter which will determinate the final volume of the sphere.

But first of all, it is necessary to make a remark concerning the meshes. We calculated three different meshes to check the precision of each one, the influence of the number of elements in the result of volume. To compare them, it is just necessary to calculate theoretically the initial volume of the sphere with the radius of 300mm and extract from a .maple file the initial volume calculated by Herezh++ before applying the loads (and already multiplied by 8 to "undo" the symmetries). Results are given in the table 2.3.

It is obvious and it can be observed in the results that the bigger the number of elements, the better the precision. Also we can observe that the precision does not change a lot after a certain number of elements. The fourth mesh has a huge number of elements, and maybe with much less we could obtain a similar precision.

Since calculations were made for all four different meshes, to compare the final results with the theory, we are going to present the results obtained with the finest mesh. Anyway, it is logic to think that the best error possible in the calculations made by Herezh++ is going to be bigger than the value of error in the initial volume.

N° elements	Theoretical vol (mm^3)	Calculated vol (mm^3)	Difference
41	1,13097e08	1,0913e08	-3,5050%
333	1,1310e08	1,1260e08	-0,4414%
3305	1,1310e08	1,1305e08	-0,0450%
13210	1,1310e08	1,1308e08	-0,0113%

Table 2.3: Precision of initial volume of the spheres depending on the mesh

For the case of the mesh with 13210 elements, the results compared to those analytically calculated are shown in the table 2.4. There, we compare the radius increase from the initial value (300mm) obtained analytically (theoretical) and by means of Herezh++, and we show the difference in percentage between them.

<i>E = 150 MPa</i>			
Pressure (MPa)	Theoretical Δr (mm)	Calculated Δr (mm)	Difference
0,01	7,1734	7,1884	0,2095%
0,015	11,3056	11,3678	0,5501%
0,02	15,896	16,0738	1,1199%
<i>E = 600 MPa</i>			
Pressure (MPa)	Theoretical Δr (mm)	Calculated Δr (mm)	Difference
0,01	1,6746	1,6748	0,0112%
0,015	2,5396	2,5399	0,0146%
0,02	3,4242	3,4257	0,0436%
<i>E = 3000 MPa</i>			
Pressure (MPa)	Theoretical Δr (mm)	Calculated Δr (mm)	Difference
0,01	0,3292	0,3292	0,0187%
0,015	0,4948	0,4950	0,0373%
0,02	0,6612	0,6613	0,0199%

Table 2.4: Precision of initial volume of the spheres depending on the mesh

Seen these results, now we could ask ourselves if the choice of the most complex theoretical model (large deformations and variable thickness) was worth it. To answer this question, we could compare these results to those of (for example) the simplest linear case: small deformations and constant thickness.

If we compare the difference between theory and Herezh++ in the case of small deformations and constant thickness (simple model) and the case of large deformations and variable thickness (complex model), we obtain the results shown in table 2.5.

If we want to remark the importance of the mesh size in the final result, we can observe the results in the table 2.6, which compares the "best" and the "worst" meshes (13210 and 41 elements, respectively).

$E = 150 \text{ MPa}$		
Pressure (MPa)	Difference complex model	Difference simple model
0,01	0,2095%	9,6536%
0,015	0,5501%	15,6044%
0,02	1,1199%	22,5969%
$E = 600 \text{ MPa}$		
Pressure (MPa)	Difference complex model	Difference simple model
0,01	0,0112%	2,1886%
0,015	0,0146%	3,3212%
0,02	0,0436%	4,5123%
$E = 3000 \text{ MPa}$		
Pressure (MPa)	Difference complex model	Difference simple model
0,01	0,0187%	0,4457%
0,015	0,0373%	0,6795%
0,02	0,0199%	0,8781%

Table 2.5: Radius difference between Herezh++ and our analytical development for two different models: a complex model and a simple model

2.2.4 Conclusions

It can be observed that results are quite good, the error is not very big in any case. In the worst case (the most unfavorable conditions, i.e. the largest deformation, occurring with $E=150 \text{ MPa}$ and $P=0.02 \text{ MPa}$), the difference in the radius increase between theory and Herezh++ is 1.12%. The radius increase corresponds to a deformation of $\Delta r/r = 16.074/300 = 0.0536 = 5.36\%$. Then, the biggest difference *in deformation* between theory and simulation is 1.12% of a deformation of 5.36%, which makes a global difference of $0.012 \times 0.0536 = 0.0006$ (a quite good precision).

Also, it is remarkable that the choice of a complex model for the theory was important. With a small Young's modulus and a high internal pressure, the deformation is important (around 16mm of radius increase). This originates a decrease of the walls' thickness that is not negligible (it goes from 0.27 to 0.253, a decrease of 6.3%). In the table 2.5 it can be observed that, for the case of $E=150 \text{ MPa}$ and $P=0.02 \text{ MPa}$, the difference in the radius increase between theory and simulation is 1.12% with a complex theoretical model, and 22.6% with a simple model (small deformations and constant thickness).

Concerning the mesh, as we increase the number of elements we obtain, logically, a more precise result (see table 2.6). In fact, since we cannot have a perfectly smooth sphere, there will always be an error between the theoretical volume and the meshed sphere's volume. This can be one of the reasons of the difference between theory and simulation: we start with an initial error due to the better or worse precision of the mesh. As it can be seen in the table 2.2, even for the finest mesh (with 13210 elements), the difference with theory in volume is 0.011%, error that means in radius a deviation of 0.003754%.

<i>E = 150 MPa</i>		
Pressure (MPa)	Finest mesh errors	Coarser mesh errors
0,01	0,2095%	-2,2037%
0,015	0,5501%	-2,1391%
0,02	1,1199%	-1,7738%
<i>E = 600 MPa</i>		
Pressure (MPa)	Finest mesh errors	Coarser mesh errors
0,01	0,0112%	-1,4639%
0,015	0,0146%	-1,7391%
0,02	0,0436%	-1,9047%
<i>E = 3000 MPa</i>		
Pressure (MPa)	Finest mesh errors	Coarser mesh errors
0,01	0,0187%	-0,6193%
0,015	0,0373%	-0,7821%
0,02	0,0199%	-0,9001%

Table 2.6: Comparison of errors when using the finest mesh with those when using the coarser mesh

Due to this, it is logical to think that we will find at the end of simulation at least this difference with theory, and that is what happens and what we can see in the results.

Another possible thing which may cause de difference or error between the theory and the simulation is the fact that the calculation made in Herezh++ is not exactly the same that we made in the theory. In Herezh++ a thin-shell model is used, for which the thickness' variation is calculated from the compressibility modulus, the trace of the stress and the relative variation of volume, which is different to the trace of the strain (used in our theoretical calculations).

Chapter 3

Dynamic Relaxation Method

3.1 Introduction

The dynamic relaxation (DR) is a numerical method usually used in the form-finding of all kind of structures (tensegrity structures, membrane structures, shell structures...) that consists in considering that the mass of the system is discretized and lumped in the nodes; these nodes oscillate about the equilibrium position, and by introducing artificial inertia and damping, the nodes come to rest in the static equilibrium position.

The fact of using artificial inertia and damping, makes the use of DR methods be restrained to the cases where *the only objective of the calculation is to obtain the final equilibrium position of a structure*, because the transient part will not be physical. However, the displacement path is close to a physical one, as it will be shown in this work.

In the literature, we can find DR methods using kinetic damping and DR methods using viscous damping. The methodology of this two methods is different. In the case of **DR with kinetic damping**, the kinetic energy of a structure is traced, and velocities are reset to zero at each of the kinetic energy peaks (that are gradually smaller) until the balance of internal and external forces is reached and the structure comes to rest; therefore, the principle in this case is to try to optimize the mass matrix in order to reach as fast as possible the kinetic energy peaks. On the other hand, when using **DR with viscous damping**, the velocities are not so important; the main idea is to try to damp as effectively as possible the oscillations, by searching an optimum viscous damping coefficient.

The most commonly used damping method is the viscous damping. This method is closer to the real behavior of the structures, since they behave as if they were somehow viscous. The kinetic damping makes the structure evolve in a very different way.

Within the following sections, two scientific papers are presented. In the first paper [15], we focus in the DR method with kinetic damping. There, we propose two different formulations for the mass matrix that extent the range of applicability of the method to any kind of element and any type of reversible behavior (instead of the previous limitation of only triangular elements and elastic behavior); some case studies are shown to prove the efficiency and reliability of both proposals. Also, we show in this paper that even if the

transient part of the calculations is not "physically real", the DR can be implemented with an incremental formulation, being this way able to carry out the calculations in several loading steps where a static equilibrium is reached. Therefore, with an adequate definition of the loading steps, DR can also provide the intermediate part of the calculations.

In the second paper, that has been recently submitted to the journal "Mechanics Research Communications", we make a review of the existing DR methods up to the present date, including DR methods with kinetic damping and DR methods with viscous damping. After implementing several types of DR methods with viscous damping in our calculation software Herezh++, we show a comparison of some of what we considered the most relevant DR methods existing in the literature. We compare them in the particular case of form-finding of membrane structures.

***NOTE:** Both full papers are included in the following sections. Also, in order to ease their understanding and to clarify certain points, extra information not included in the papers' submission is added. This extra information is written in italics.*

3.2 Numerical study of dynamic relaxation with kinetic damping applied to inflatable fabric structures with extensions for 3D solid element and non-linear behavior

J. Rodriguez, G. Rio, J.M. Cadou, J. Troufflard

Abstract: This work mainly deals with the numerical study of inflatable fabric structures. As implicit integration schemes can lead to numerical difficulties such as singular stiffness matrices, explicit schemes are preferred. Since the final objective of this study is to obtain the final shape of a structure, a dynamic relaxation (DR) method is used. These methods allow us to obtain the final and stable shape of the inflatable fabric structures without doing so many time increments, which is the case when using a classical explicit integration method. Han and Lee (Computers and structures, 2003, 81, pp. 1677-1688) proposed an extension of the DR method stated by Barnes (Computers and Structures, 1988, pp. 685-695) suitable for triangular elements and elastic behavior. There are two main contributions in this paper. Firstly, we propose a modification of Han and Lee's method, allowing it to be used with any kind of membrane or solid finite elements and any reversible behavior. Secondly, we propose to rewrite the expression initially introduced by Barnes. Furthermore, these proposals are adapted for incremental loadings, allowing this way to obtain the pseudo-equilibriums of the intermediate phases. Numerical examples from academic problems (rectangular and circular membranes) show the efficiency and the reliability of proposed methods, with linear elasticity behavior, and also with a non-linear incremental behavior and finite deformation states.

Keywords: Dynamic relaxation; kinetic damping; inflatable structures; form-finding

Published: Thin-Walled Structures, 2011. doi:10.1016/j.physletb.2003.10.071

3.2.1 Introduction

The simulation by the FE method of inflatable fabric structures, when a pressure load is applied and an implicit scheme is used, can lead to severe instabilities due to the lack of stiffness in the fabric. For instance, in certain cases the basic Newton-Raphson algorithm cannot achieve a final convergence due to the swapping between several stable states. Explicit time schemes overcome this difficulty, but they need a huge number of time steps to obtain a realistic stable final shape. This occurs when using natural damping.

This is an usual issue in civil engineering (some examples are: geotechnical problems [60], prestressed coated fabric membranes [41], architectural structures [16], and space inflatable structures [17]), and there have been several solutions proposed [21, 22, 23, 24, 25] by using *dynamic relaxation* methods.

The classic form of the dynamic relaxation (see for example [28] or [29]) mainly is to use an artificial viscosity to damp the movement, and to search for the critical damping value (see [27] for a comprehensive review). However, among the existing dynamic relaxation methods, we are interested in a different method; the one proposed by Barnes [30]. It has been initially applied to the calculation of prestressed cable structures and further extended by Han and Lee [21] to be used with triangular elements and a linear elastic behavior. This method combines a kinetic damping (resetting the speed to zero at each kinetic energy peak), often used in form-finding, and an optimization of the mass matrix (proposed by Han and Lee).

One application of the method is thin fabric structures loaded by pressure, which are notably unstable during loading due to the lack of flexion stiffness. The static final form does depend on the inertial forces that act during the transient evolution. Considering this, the right value of the mass is supposed to have no influence on its static final form. In order to quickly reach the stable deformed state, we must first adapt the mass matrix and then use kinetic damping. Kinetic damping has been successfully employed by several authors (one example is [39]). A correct choice of the mass matrix leads to an optimal convergence of the dynamic relaxation method.

In this paper, we will present two main formulations. Firstly, we propose an extension of that Barnes-Han-Lee method. Secondly, we propose a general expression based on the works of Barnes for the mass matrix calculus. The basis of this second expression has already been proposed in previous papers (see Underwood [44] or Barnes [30]), but to our knowledge, no systematic studies have been done concerning its applications for simulation of the inflation of unstable structures. Both formulations can be used with any reversible behavior, any type of membrane element and also solid elements. We show, with numerical examples, their correct operation even when dealing with complex mesh shapes or 3D elements. Our methods aim to find one solution when one or more solutions exist (there can be several stable final shapes).

The reminder of this paper is broken into three main parts. In section 3.2.2, we first explain the dynamic relaxation method that our work is based on. We then present two methods for the formulation of the mass matrix. We propose an initial method based on the formulation of Han and Lee and also propose an alternate method based on a different formulation of the mass matrix. In section 3.2.3, we show several numerical case studies and results of application of our proposals after implementing them in the software Herezh++ [18]. Finally, in section 3.2.4, we briefly discuss our conclusions.

3.2.2 Dynamic Relaxation Method

3.2.2.1 Kinetic damping

Before presenting the dynamic relaxation method itself, we present the kinetic damping.

Kinetic damping method was firstly introduced by Cundall [32]. It consists in resetting velocity to zero at each kinetic energy peak. This simple procedure has generally been found to be stable and allowing a fast convergence [30]. When there is no external energy

acting, there is just internal elastic energy to evolve towards the steady state position.

Velocities are reset to zero at each kinetic energy peak because the structure oscillates, and the kinetic energy peaks are supposed to occur close to the static equilibrium position. Then, the computation is restarted from the current configuration, but with zero initial velocity. This procedure is continued until the structure comes progressively to a static equilibrium position.

An example of application that will be presented and developed later on can be seen in the Figure 3.1, where it can be observed in red the evolution of the kinetic energy and in green the residual. There, we can see that the residual decreases significantly each time the velocities are reset to zero, what means that the method is effective. However, it can also be observed that the effectiveness is inferior at the end of the calculation, where kinetic energy peaks are very small.

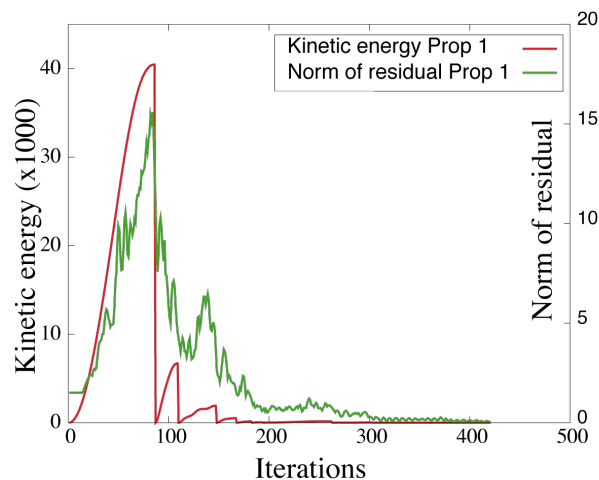


Figure 3.1: Kinetic energy and residual for a random DR calculation where kinetic damping has been applied

A detailed review of the implementation of kinetic damping can be read in the works of Barnes [30, 36] or even in the thesis of Troufflard [1].

This damping method was implemented in the calculation software used in this thesis (Herezh++) by including several parameters, that are detailed in the following:

Kinetic damping parameters implemented and used in Herezh++ Although the kinetic damping principle is very simple, the numerical behavior of the calculations makes it interesting to have the control of some parameters concerning the kinetic damping. In this section, the input parameters used in Herezh++ are described. (NOTE: Unless if a detailed description of the used parameters is wanted, this part can be skipped).

Kinetic damping does not have to be applied from the very beginning of the calculation. To avoid it to start right at the beginning and thus avoiding taking into account eventual

initial oscillations, a parameter can be defined to indicate since which iteration we need it to start working:

`nb_deb_test_amor_cinetique_ [iteration_number]`

During a calculation, a high number of oscillations can appear. In order to avoid the kinetic damping to act in all the "fake" kinetic energy peaks, there is the possibility of defining a parameter that indicates how many times the kinetic energy has to decrease in order to allow to reset velocities to 0:

`max_nb_decroit_pourRelaxDyn_ [number]`

For the same reason of the eventual many oscillations, it might result advantageous not to look at the kinetic energy at every single iteration, but calculating the average over a bunch of iterations, and resetting to zero the velocities whenever a peak is reached in this averaged value of kinetic energy. A parameter allows to indicate the number of iterations considered to calculate the average (by default, if the parameter is omitted, its value is 1):

`taille_moyenne_glissante_ [number_of_iterations]`

It is difficult to determine with precision the peaks of kinetic energy, and a criterion can be used to ensure a peak has been reached. For example, we can assume that the kinetic energy has passed a peak whenever it diminishes after a peak a certain value. This value can be a fraction of the last peak. In spite of that, a parameter is defined to indicate the value of the fraction, that can be adjusted according to our interest:

`test_fraction_energie_ [fraction_value]`

When a calculation is near convergence, there can be a lot of small oscillations that may not need the kinetic damping to accelerate the convergence. Due to this, and in order to reduce the cost of calculation, there is a parameter which allows to deactivate the kinetic damping. This parameter is a coefficient that multiplied by the last kinetic energy peak gives the minimum acceptable kinetic energy to continue using the kinetic damping. Kinetic damping is paused/stopped if $E_k < coef \times E_k^{peak}$:

`coef_arret_pourRelaxDyn_ [coefficient_value]`

The same way the use of kinetic damping can be disabled at a certain moment, it can be re-enabled if the calculation needs it. A coefficient can be defined so if it is multiplied by the maximum kinetic energy peak, it gives the minimum kinetic energy that would reactivate the kinetic damping. Kinetic damping is reactivated if $E_k > coef \times \max(E_k^{peak})$:

`coef_redemarrage_pourRelaxDyn_ [coefficient_value]`

To stop the calculation, we can consider a convergence criterion based on the displacement of the structure, by checking the displacement between two iterations. Thus, we can establish an inferior limit to $\Delta x_{\tau \rightarrow \tau + \Delta \tau}$ with:

```
max_deltaX_pourRelaxDyn_ [minimum_displacement]
```

A parameter can be used to indicate the number of times the previous criterion has to be verified to allow to stop the calculation:

```
nb_max_dX_OK_pourRelaxDyn_ [number]
```

Finally, another parameter can be used to indicate the number of passages into damping from which the end is checked:

```
nb_deb_testfin_pourRelaxDyn_ [number]
```

Presented the parameters, if nothing is specified, the used parameters in all the calculations in this thesis are ¹:

```
max_nb_decroit_pourRelaxDyn_ 1
# taille_moyenne_glissante_ 30
# test_fraction_energie_ 0.05
coef_arret_pourRelaxDyn_ 0
coef_redemarrage_pourRelaxDyn_ 0.0
max_deltaX_pourRelaxDyn_ 0.005
nb_max_dX_OK_pourRelaxDyn_ 10
nb_deb_testfin_pourRelaxDyn_ 250
```

3.2.2.2 Dynamic relaxation method

The problem that we need to solve, after discretization by FE, is:

$$[M]\ddot{X} + R(X, \dot{X}) = 0 \quad (3.1)$$

where $[M]$ is the diagonal mass matrix; X, \dot{X}, \ddot{X} are respectively the position, velocity and acceleration of the nodes and $R(X, \dot{X})$ is the residual of internal and external forces in function of the position and velocity of nodes. The term $[M]\ddot{X}$ represents the generalized expression of the acceleration forces. The method used to solve the problem in time is based on the explicit centered finite differences method (CFD).

The calculation of equilibrium is always made in the final configuration, using the Cauchy's stress tensor.

In the case of a Hooke's elastic law of behavior, Cauchy's tensor is associated with Almansi's deformation measure. The deformation is calculated from the variation of the

¹The # symbol means "commented line". Therefore, the two commented lines mean that we did not use those two parameters in our calculations

coordinates of the metric tensor associated to the material coordinates of the point in the reference element (a comprehensive example of this calculus has been presented in [20]). Then, the stress tensor is obtained by means of the formulae:

$$\textit{Spheric part} : \quad \frac{\textit{trace}(\sigma)}{3} = K \textit{trace}(\epsilon) \quad (3.2)$$

$$\textit{Deviatoric part} : \quad \textit{dev}(\sigma) = 2 G \textit{dev}(\epsilon) \quad (3.3)$$

In the case of the more complex material behavior: Hart-Smith, that we use in one of our numerical examples, the tensor of left Cauchy-Green B is determined, using again the coordinates of the metric tensor. Its invariants are then used to define the potential and its different variations, needed for the calculation of Cauchy's stress tensor [20].

For both of these behaviors, only the initial and final states are taken into account.

Since acceleration forces depend on the mass, the dynamic relaxation method proposed by Barnes [36] uses an arbitrary mass term in order to improve the kinetic damping while keeping the numerical stability. This mass matrix is obtained from the Courant-Friedrichs-Lewy (CFL) condition [8] which gives the maximum Δt . This limitation is given by:

$$\Delta t \leq \frac{2}{\omega_{max}} \quad (3.4)$$

where ω_{max} is the maximum frequency of equation (3.1). This frequency can be expressed by:

$$\omega_{max} = \sqrt{\mu_1} \quad (3.5)$$

and μ_1 represents the largest eigenvalue of the matrix $[M]^{-1}[K]$. In order to minimize the computation time, Δt must be chosen close to the limit indicated in (3.4). If $[M]$ is chosen as a diagonal matrix, and if $[K] = a[M]$, then $2/a$ is a near upper bound on μ_1 [16]. With $\mu_1 \approx 2/a$, the maximum time step to remain in stability is:

$$\Delta t_{max} \approx \sqrt{2a} = \sqrt{2 \frac{[M_d]}{[K_d]}} \quad (3.6)$$

Underwood [44] has found that a Δt close to 1 is sufficient to ensure stability, and Lewis [16] gives a brief reasoning of this choice. From the previous equations we obtain:

$$m \geq \frac{\Delta t^2}{2} k_{max} \quad (3.7)$$

where k_{max} is the largest value of $[K_d]$. The eventual large displacements generated by the external loads lead to a large variation of the stiffness, and thus of the eigenvalues of $[K_d]$. Therefore, an exact calculation of the stiffness at each increment would be expensive for the calculation, so an estimation of k_{max} is preferred.

The dynamic relaxation method proposed by Barnes [30] uses an arbitrary mass term in order to improve the kinetic damping while keeping the numerical stability. In the previous studies, Barnes proposes a lumped mass matrix where the elements m_i in the diagonal are:

$$[m_i] = \lambda \frac{\Delta t^2}{2} [k_i] \quad (3.8)$$

where m_i is the mass matrix at node i ; k_i represents the diagonal component of the stiffness matrix in the principal direction; Δt is arbitrarily chosen as 1; and λ is a convergence parameter which is constant for the whole structure. The optimum mass matrix is calculated by adjusting the parameter λ , that can be considered as a modifier of the size of the time step.

The term $k_{i_{max}}$ can be decomposed in two parts: one part related to the material and another one related to the geometry:

$$k_{i_{max}} = \sum (k_{mat} + k_{geo}) \quad (3.9)$$

For membrane elements, Han and Lee also proposed to choose the largest stiffness term for the calculation of the mass term, and they stated, for CST (constant stress triangle) elements, that the stress k_i at a node i can be approximated as

$$k_{i_{max}} = \sum_e \frac{h}{4S_0^e} \left(\frac{E}{1-\nu^2} + \sigma_x + \sigma_y + \sigma_{xy} \right) \quad (3.10)$$

where h is the thickness of the element e , S_0^e is the initial surface of the element e , and $\sigma_x, \sigma_y, \sigma_{xy}$ are the components of the stress tensor in an orthonormal basis associated to the surface element. E and ν are the coefficients of the isotropic elastic Hooke's behavior law.

The time step is arbitrary, and for simplicity, its value in the formule 3.17 has been chosen as 1. The consequence is that this time step does not appear directly in the time-advance algorithm, but it does in the loading, boundary conditions and material's behavior.

In reference [42], the authors propose to suppress the surface term S_0^e in order to obtain mass dimensions in equation 3.17. They show, particularly, that in this case the optimal value of the coefficient λ is more stable, what is advantageous when it has to be defined. The expression becomes then:

$$k_{i_{max}} = \sum_e \frac{h}{4} \left(\frac{E}{1-\nu^2} + \sigma_x + \sigma_y + \sigma_{xy} \right) \quad (3.11)$$

In this work, we propose two ways to generalize the previous approaches, which we define in the two following subsections.

The first proposal is a generalization of the method proposed by Barnes-Han-Lee, where the intention is to extend the applicability to all types of elements (not only triangular) and to any kind of behavior (not just elastic). However, only reversible laws of behavior are studied; more complex laws will be the subject of future research.

The second proposal is based in the works of Underwood [44]. These works are based in the circle theorem of Gershgorin which permits to obtain an upper bound to the eigenvalue "i" of the stiffness matrix $[K]$ of the system [9]: "Every eigenvalue of a matrix A lies in at least one of the circles C_1, \dots, C_n , where C_i has its center at the diagonal entry a_{ii} and its radius $r_i = \sum_{j \neq i} |a_{ij}|$ equal to the absolute sum along the rest of the row". This second method presents as a disadvantage that it needs at least the calculation of one stiffness matrix, what implies the need to being able to calculate the tangent behavior. Generally, at the beginning of the loading process, the evolution is mainly elastic, so a priori the stiffness belonging to the tangent behavior should be enough if we consider that the material tends to soften.

3.2.2.3 Proposal 1: extension of the formulation of Barnes-Han-Lee

Here we propose an extension of the previous formulation, on one side to other type of elements and on other side to other material's behavior. The aim is therefore to study the feasibility of this extension. Let us consider the following expression, which would replace Han-Lee's [21] :

$$k_{imax} = \sum_e \frac{l_e}{4} \left(\alpha K + \beta \mu + \gamma \frac{I_\sigma}{3} + \frac{\theta}{2} \sigma_{mises} \right) \quad (3.12)$$

Looking at the expression 3.10, the term $\frac{E}{1-\nu^2}$ can be considered as controlling the shape changing or the element volume changing. It could be replaced by a linear combination of the average compressibility modulus K and shear modulus μ , available for all elastic and hyperelastic laws: $\alpha K + \beta \mu$.

Initially, parameters α and β can be chosen as $\alpha = \beta = 1$, what leads to a magnitude almost equal to the initial formulé's one (with the condition of a not very high compressibility). For example, if $\nu = 0.3$, we get: $\alpha K + \beta \nu \approx 1.21E$, while with Han-Lee's formulé 3.10 we obtain: $\frac{E}{1-\nu^2} \approx 1.1E$.

Concerning the second part of the equation 3.10 proposed by Han-Lee, the term $\sigma_x + \sigma_y + \sigma_{xy}$ can be considered as representing the stress state in the material (cumulating the spheric and deviatoric parts). For our proposal, and in order to extent the use of the formulé to other geometries than triangular elements, we replace this term by an invariants' combination: $\gamma \frac{I_\sigma}{3} + \frac{\theta}{2} \sigma_{mises}$, where $I_\sigma = \sigma_k^k$ is the trace of the Cauchy stress tensor and σ_{mises} is the Mises stress. They represent respectively the intensity of the spherical and the deviatoric parts of the stress tensor. These two quantities are tensor invariants so they could be calculated for any type of element.

Therefore, the coefficient $\frac{1}{3}$ is added so $-\frac{I_\sigma}{3}$ represents the spherical pressure, and the coefficient 0.5 is added so $0.5\sigma_{mises}$ represents the amount of shear.

The parameters α, β, γ and θ in the expression 3.18 permit to control the influence of each entity. And finally, l_e represents a geometrical characteristic length, suitable for 2D elements (thickness) and for 3D elements (cubic root of the volume).

Notice the presence of the stress terms, what implies that the mass matrix has to be updated all along the calculation.

3.2.2.4 Proposal 2: Second formulation for the mass matrix

The second proposal refers to the theoretical elements proposed by the early work of Underwood [44] by using the theorem of Gerschgorin which permits to obtain an upper bound to the eigenvalue "i" of the stiffness matrix "K" of the system:

$$\rho_i \leq \sum_j |K_{ij}| \quad (3.13)$$

The mass matrix is then built to satisfy the stability condition with a unitary time step.

$$m_i = \frac{\lambda}{2} \text{MAX}_{k=1}^3 (\rho_{3(i-1)+k}) \quad (3.14)$$

Unlike the physical masses, we can expect a variation of the mass matrix built this way during the calculation. Given that on one side we choose the maximum value over the 3 axes (loop over k in 3.14) and on the other side the stiffness of the initial material behavior is generally more important than during deformation, it has been proved in our simulations that the mass matrix calculated at the beginning was enough to "guide" the whole simulation, i.e. the update of the mass matrix along the calculation of our simulations did not provoke any time gainings.

The method presents as a disadvantage that it needs at least the calculation of one stiffness matrix, what implies the need of being able to calculate the tangent behavior. Generally, at the beginning of the loading process, the evolution is mainly elastic, so a priori the stiffness belonging to the tangent behavior should be enough if we consider that the material tends to soften.

In order to make the calculations converge as fast as possible, the idea is to be as close as possible to the critical time step. However, being too close to the critical time step can eventually provoke instabilities and divergence. In the dynamic relaxation method formulae, the time step Δt is usually arbitrarily fixed to 1. However, the presence of the parameter λ can be considered as a factor of this fixed time step. Its optimum value cannot be determined a priori (we observed that it depends on the mesh geometry, elements size, etc.). However, the relation (3.13) and the formule (2.4) of reference [44] lead to a minimum theoretical value of λ for the second proposal: $\lambda \geq 0.5$.

The range of values to find the optimum value of λ is different for each one of our proposals, being this range much smaller in the case of the second proposal (around 0.5-0.7 for the proposal 2 vs. 5-15 for the proposal 1).

3.2.2.5 Incremental scheme and convergence criterion

In the case of an incremental law of behavior, a priori not totally reversible, when the loading leads to big deformation-stress final states, the final-form finding procedure in one step is not correct anymore. The final state depends indeed on the loading path which in the case of DR can be very different to the real path. A solution is to use an incremental loading procedure. Assuming that increments are small enough, the procedure then guarantees a succession of points of static physical equilibrium that allows to be close to the real response of the structure during the loading.

The convergence criterion in the steady state must comply with two points. In one part, the structure must be in mechanical equilibrium, what we represent as a norm of the residual of the static generalized forces -internal and external-, inferior to an instruction's value. In other part, in the case where the kinematic boundary conditions block the global solid movements, we impose the final kinetic energy to be also inferior to an instruction value, what also guarantees the equilibrium in the case where the generated stresses are very low. In the practical, these conditions are applied under a relative form according to:

$$Max \left(\frac{\|Residual\|_{\infty}}{\|Reactions\|_{\infty}}, \frac{Kinetic\ Energy}{Internal\ Energy} \right) \leq \varepsilon \quad (3.15)$$

where ε is the convergence criterion (the mentioned instruction value).

3.2.3 Numerical case studies

In this section, we will perform numerical case studies on the formulae 3.12 and 3.14. We use the C++ academic finite elements software Herezh++ [18], and for the meshing and postprocessing, we use the software Gmsh [66].

The numerical case studies in the section are described below:

- Firstly, we show how we can adapt the parameters of the first of our proposed formulae to obtain an equivalent calculation to Han and Lee's formulation. We also compare it to our second formule using the classical test of inflation of a rectangular cushion.
- Based on the same numerical test, we show that both of our proposed formulae work with complex meshes, with different geometries, with different element types and different interpolations.
- We demonstrate our proposed formulae working with meshes composed of 3D elements, using an inflate test of a rectangular cushion and a traction test of a partially perforated plate.
- Finally, we explore how the formulae works when using a complex law of behavior.

3.2.3.1 Equivalence between the formulation of Han and Lee and our proposals

The objective in this section is to verify the equivalent calculation between the method proposed by Hann and Lee, 3.10, modified by Troufflard [42] and our formulae 3.12 and 3.14. Notice that considering the term σ_{xy} in the formule 3.10 is problematic, because it depends on the coordinates on which it is calculated. In our work, in order to suppress this dependance, we propose to be situated in a stress eigenvector frame, which leads, considering the plain stress hypothesis, to $\sigma_{xy} = 0$, $\sigma_x + \sigma_y = trace(\sigma)$ and $\gamma = 3$ in (3.10).

The solution permitting to determine the terms α and β is not unique. We keep:

$$\alpha = \frac{3(1 - 2\nu)}{2(1 - \nu^2)}, \beta = \frac{1}{1 - \nu} \text{ being : } K = \frac{E}{3(1 - 2\nu)}, \mu = \frac{E}{2(1 + \nu)} \quad (3.16)$$

In this case, relations 3.10 and 3.12 are identical, what shows that our first proposal includes the former Han-Lee's proposal.

The calculation is carried out in linear elasticity, $E = 125MPa$ and $\nu = 0.41$, which are coherent with the parameters of behavior of a usual thin fabric. Concerning the expression 3.14, we use for this exemple a value of $\lambda = 0.6$ (we will discuss about this parameter afterwards).

The first numerical test is a classical one, which has already been studied, for example, in reference [22]: the inflation of a rectangular shaped cushion. It consists in two membranes joined at their periphery, with dimensions $500mm \times 500mm \times 0.27mm$. Due to the symmetries, just 1/8 of the cushion is studied. The cushion is loaded with an instantaneous internal pressure of 0.015 MPa. The mesh is constituted of a ruled triangular division, $25 \times 25 \rightarrow 625$ elements.

Finally, the convergence criterion 3.50 is set to: $\epsilon = 1.e - 3$.

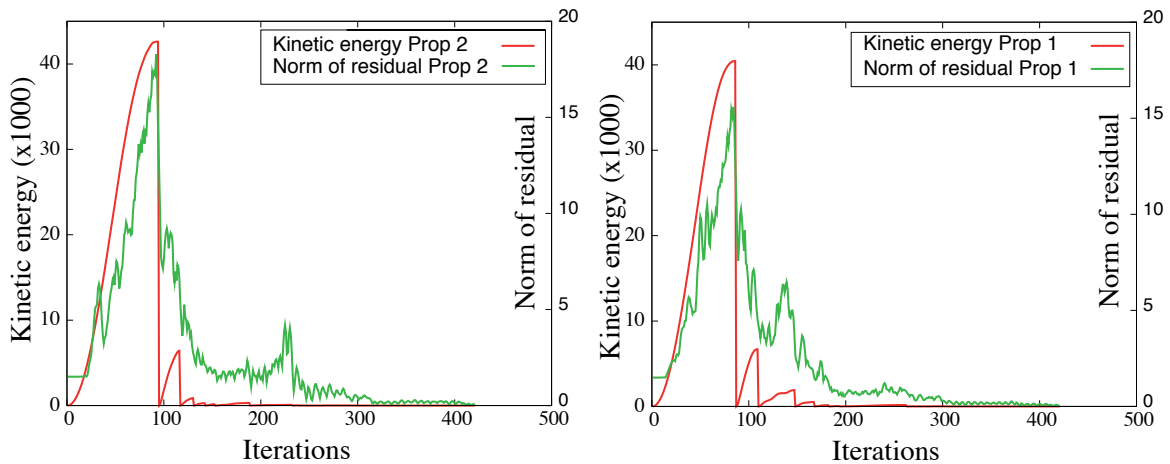


Figure 3.2: Inflation of squared cushion. Evolution of kinetic energy and residual of static equilibrium in fonction of the number of iterations, for each one of the proposals

The evolution of kinetic energy in fonction of the iteration number, Figure 3.2, shows clearly the kinetic damping points (i.e. speeds reset to 0). Globally, the evolution for both proposals is very close. Entering into detail, notice that the first maximum of kinetic energy occurs a bit later in the case of the second proposal, but on the other hand, the decrease’s gradient seems to be bigger for this second proposal. We can also notice the regular diminution of the norm of static residual, quite similar for both methods, with an important diminution at each kinetic damp.

3.2.3.2 Membranes: complex meshes

The aim of the second application is to validate our two proposals in the case of more complex meshes. So we study 2D meshes, with triangular and quadrangular elements, and with linear and quadratic interpolations. Also, two different qualities of mesh are considered: a grid of 25×25 elements and another one of 50×50 . The geometry and the material behavior are identical to the first application, in the previous section. For the first proposal, we use the parameters $\alpha = 0.9022557, \beta = 0.9022557, \gamma = 1, \theta = 1$.

For the different tested samples, we use the notation indicated in table 3.1. Thus, as an example, the notation RL1 means: test made with a mesh with 25×25 Rectangular elements, and using Linear interpolation.

T: Triangular elements	R: Rectangular elements
L: Linear interpolation	Q: Quadratic interpolation
1: Mesh of 25x25	2: Mesh of 50x50

Table 3.1: Notation

The figure 3.12 shows an example of inflated membrane. There, we can observe that the method permits also to capture eventual wrinkles, local instabilities which can appear during the inflation. We would like to remark that it is not the aim of this work to obtain the best precision for the wrinkles. It is evident that, the smaller the mesh is, the more we gain in wrinkles’ precision. But as told, the aim of this work is to obtain one among all the possible solutions for the steady inflated state; we cannot assure that the obtained wrinkles would have the same shape and would be placed in exactly the same position than in reality. To assure that, further studies must be made.

For each geometry, the table 3.2 shows the obtained results with an optimum λ . Calculations are made in an Apple computer (Processor: 2x2.93 GHz Quad-Core Intel Xeon, Memory: 16 Go 1066 MHz DDR3) with just one processor .

Firstly, it can be observed that convergence is reached in all the cases. Particularly, the quadratic interpolation does not induce a particular difficulty.

The number of needed iterations is slightly higher with the second proposal, but the associated calculation times stay however smaller or equivalent, due to the fact that the stiffness matrix is not recalculated at each iteration, unlike the proposal 1.

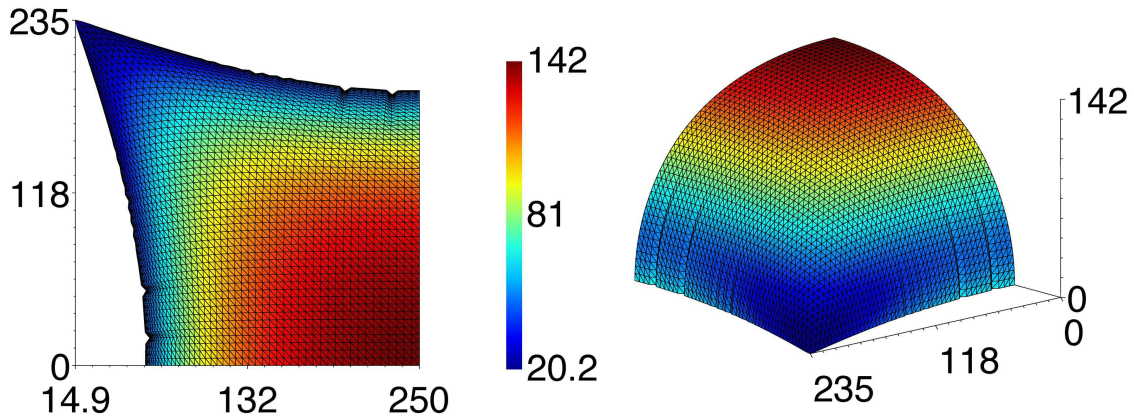


Figure 3.3: Inflated squared cushion: representation of 1/8 of the cushion, displacement isovalues

Mesh	<i>Proposal 1</i>			<i>Proposal 2</i>		
	λ_{opt}	Iterations	Time [s]	λ_{opt}	Iterations	Time [s]
TL1 (2028 dof)	10	546	14,1	0,6	565	13,8
TL2 (7803 dof)	10	923	101,5	0,7	1081	111,8
TQ1 (7803 dof)	13	1128	118,4	0,6	1185	119,8
TQ2 (30603 dof)	14	2158	943,3	0,7	2358	970,1
RL1 (2028 dof)	6	422	23,7	0,5	423	22,6
RL2 (7803 dof)	6	671	150,4	0,6	841	183,9
RQ1 (7803 dof)	10	1015	159,8	0,5	970	148,8
RQ2 (30603 dof)	9	1688	1085,6	0,5	1889	1552,1

Table 3.2: Inflation of 1/8 of cushion in just one loading step, for different meshes

The range of variation of the parameter λ , even if it is smaller than in the original method of Barnes-Han-Lee, 3.10, it is still quite large for the proposal 1. This point is important, because it imposes preliminary tests in the case of a full new mesh in order to determine the optimum value for λ . In the case of the proposal 2, a value of 0.6 or 0.7 ensures a convergence near the optimal one in all the studied cases.

The increasing number of iterations seems to be proportional to the square root of the number of dof, i.e., the mesh density.

3.2.3.3 Circular mesh

The third application concerns the inflation of a circular cushion, with a diameter of 400mm, where the mesh, Figure 3.4, includes both triangular and quadrilateral linear elements. The other material, geometric, etc, characteristics are identical to the squared

cushion’s ones, and also the methods.

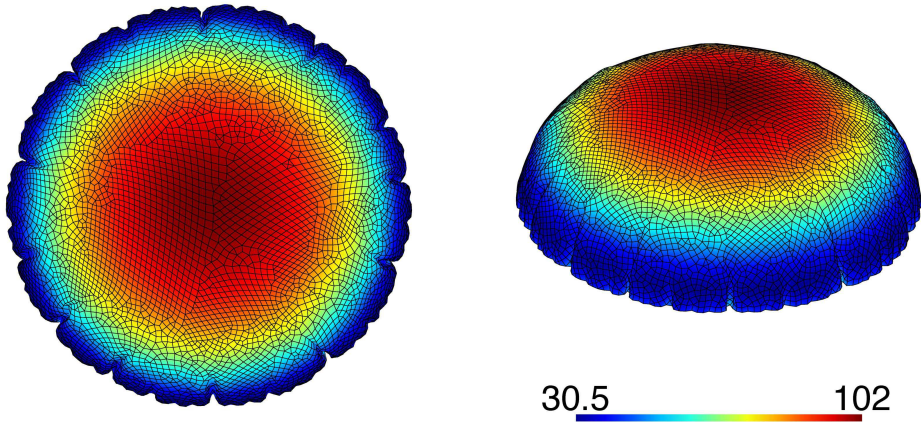


Figure 3.4: Inflated circular cushion: displacement isovalues

The Table 3.3 shows that the number of necessary iterations for convergence is consistent with those obtained for squared geometries. The mix of elements does not seem to alter the convergence. The proposal 2 is here more interesting, because even with the same previously used value of $\lambda = 0.6$, which is not the optimum, we obtain a very good convergence.

	<i>Proposal 1</i>			<i>Proposal 2</i>		
Mesh	λ_{opt}	Iterations	Time [s]		Iterations	Time [s]
Circular	10	2096	1068,3	$\lambda_{opt}=0,4$	1322	616,745
17856 dof				$\lambda=0,6$	1703	792,6

Table 3.3: Inflation of a half of a circular cushion, with a mix of linear triangular and quadrangular elements

We can also observe the presence of wrinkles in the solution. Analogously to a classic explicit dynamic scheme, considering these instabilities does not seem to create a problem. However, the process does not allow to control the choice of the bifurcated solution.

3.2.3.4 Meshes with 3D elements

We consider now the case of 3D elements. Two different types of simulations are studied: a squared plate under a transversal load (pressure), and a partially perforated plate (just called perforated plate in the rest of the paper for simplicity) under a load in the plane. The thickness of both plates is 5mm.

The first case represents the version in 3D elements of the inflation previously studied, with also, in this case, a certain rigidity to flexion of the plate. In fact, to obtain

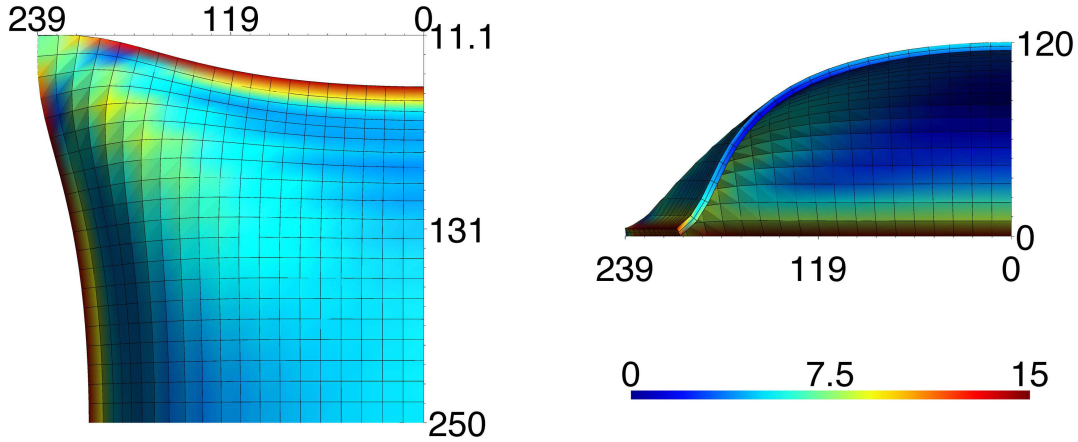


Figure 3.5: 1/4 of 3D plate under pressure, result in one step: isovalues of Mises stress (in MPa)

similar deformations, we use now a pressure of 0.08 MPa. While in the first case the deformation-stress fields are quite homogeneous in the plane (not in the thickness), and the displacements are important, in the second case, the presence of the partial hole originates an important field gradient in the plane, and displacements are comparatively smaller. Both classic interpolations, linear and quadratic are used, and also two types of element: hexahedral and pentahedral. Both proposals give similar results, but just the proposal 2 is shown here, with $\lambda = 0.7$.

Case	Element type	Elem.	Dof	It.	Time [s]
Inflation	Linear hexahedra	100	726	914	21.8
Inflation	Quadr. hexahedra (27 pt)	100	3969	2687	520.2
Traction	Linear pentahedra	2239	7200	1550	177.2
Traction	Quadr. pentahedra (6 pt)	2239	31428	4140	2410

Table 3.4: Tests with 3D elements: meshes and results

The table 3.4 shows that in all cases the calculation converges, even if it is for large deformations in the plane (Figure 3.6) or if it is for large transversal displacements including flexion (Figure 3.5). In the case of quadratic hexahedra, the studied case consists in a complete interpolation with 27 nodes and 27 integration points. A priori, this choice permits to avoid the locking in flexion, and despite the fact of having just one element in the thickness, the behavior in flexion is a priori correctly approximated. Obviously, this is not the case for the mesh of linear hexahedra, where it would be necessary to correctly approach the behavior in flexion, to include a higher number of elements in thickness (just one used here), and at least a selective integration to avoid the locking. However, we present both types of interpolation to show, on one side, that the algorithm converges

in both cases, and on other part, that the calculation times are coherent between them and with the previously obtained results.

For the case of the 3D inflation, considering the ratio of dof between the two meshes (linear and quadratic): 5.46, and the ratio of integration points: 3.38 ($=27/8$), we obtain a global ratio of around $5.46 \times 3.38 = 18.45$. If we compare this ratio with the ratio of calculation times, 24.7, we can observe that, even if they are not equal, we are in the same order of magnitude.

Concerning the traction tests on the perforated plate, the elements are pentahedra and the global ratio between dof and between quadratic and linear pentahedra's integration points is around 13 (4.37 for the dof and 3 for the integration points), while the ratio of calculation times is around 13.5. Thus, here also we observe coherent ratios.

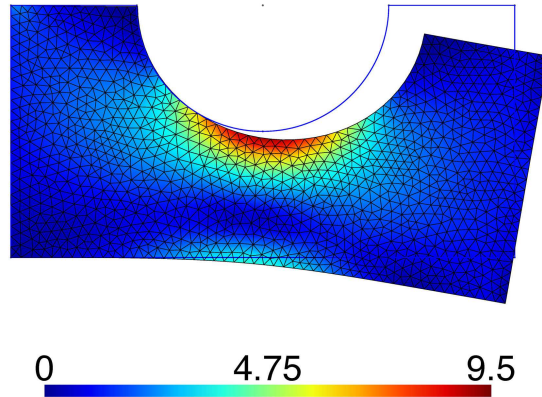


Figure 3.6: Perforated plate, result in one step: Mises stress isovalues

3.2.3.5 Incremental calculations

In order to be able to use the method in the case of an incremental law of behavior, we introduced an incremental version of the proposals 1 and 2. Actually, the dynamic relaxation method is used here to find the steady state at the end of each loading step. The method is thus analogous to a classic iterative one, with the difference that it does not need the determination of a tangent evolution; but in return it needs a larger number of iterations.

The different types of simulation 2D and 3D previously presented are studied considering 10 loading steps (increments). As an example, we present results for the proposal 2. We observe that the method works out for all kind of elements. The Figure 3.7 presents the evolution of the number of iterations versus the number of increment (loading step). We observe coherent numbers with the one-step calculation. Notice that the number of iterations -quite constant-, is less stable with the quadratic than with the linear elements.

The Figures 3.14 and 3.14 present the different steps of loading constituting the result of the intermediate pseudo-steady states resulting of the multi-step loading (to improve

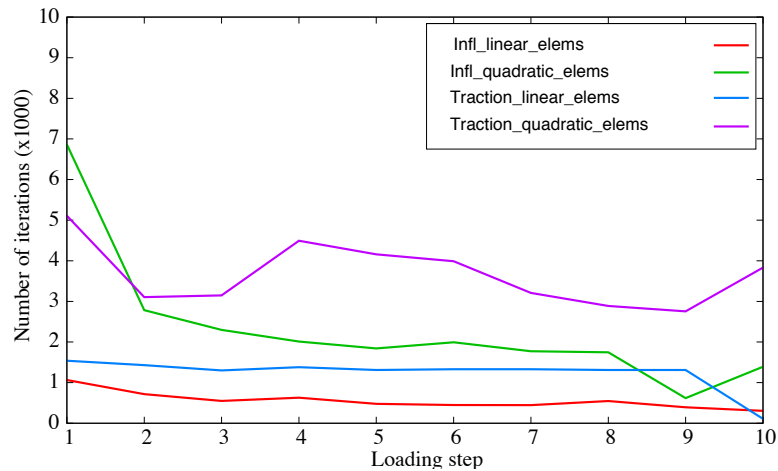


Figure 3.7: Number of iterations vs Loading step, for the second proposal, and $\lambda = 0.7$

the clarity of the figures, not all the increments are shown).

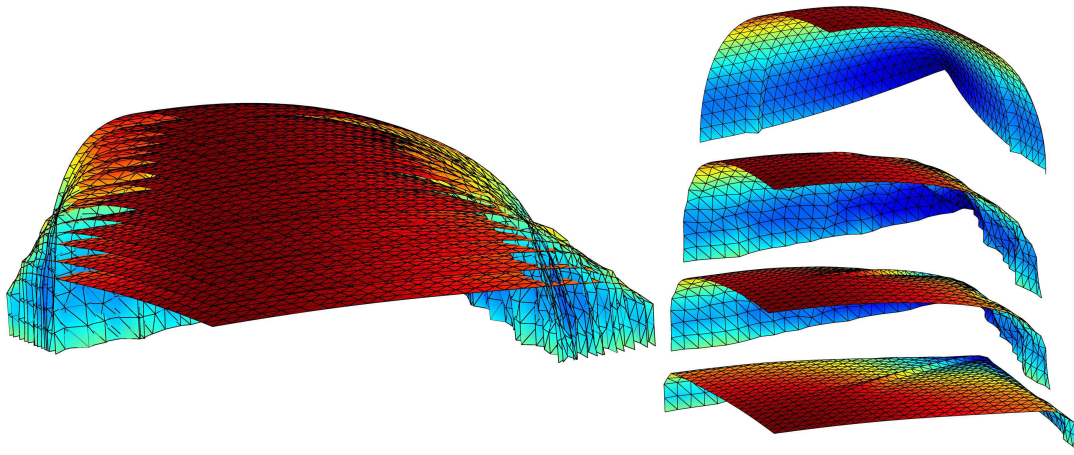


Figure 3.8: Incremental inflation of a cushion, representation of 1/8 of the cushion, 2D mesh

3.2.3.6 Complex law of behavior

The last part of the study is exploratory. It consists in observing the influence of a complex law of behavior, preferably, incremental. For that, we consider the inflation of a squared membrane, meshed with 3D quadratic hexahedral elements. The geometric dimensions are $250mm \times 250mm \times 6mm$, the mesh is constituted of a grid of $10 \times 10 \times 1$ and the used λ is 3 (bigger than before, to be sure to overcome nonlinearities). The loading is quasi-static, so the speed effects are negligible. The material is considered an elastomer Vitton where the law is modeled by assembling an additive hyperelastic stress and a stress hysteresis.

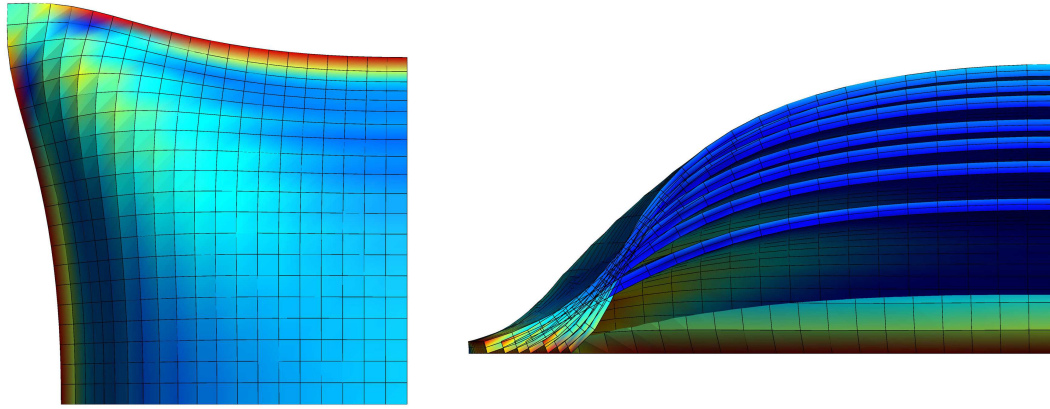


Figure 3.9: Incremental inflation of a cushion, representation of 1/8 of the cushion, 3D mesh

For more details of the law, see [19]. Just notice that the hyperelastic part is based in the model of Hart-Smith: $K = 2700$ MPa and the deviatoric part coefficients: $C1=0.067$, $C2=0.402$, $C3=3.05$. The hysteretical behavior is purely deviatoric and incremental and can be seen as an infinite and continuous assembly of couples : a spring and a frictional element in parallel. During a shear test, the slope at the origin is $\tau/\gamma = 4.59$ MPa and the saturation stress is $\tau_{max} = 0.27$ MPa.

Mesh	λ	Inc 1	Inc 2	Inc 3	Inc 4	Inc 5
3969 dof	3	32020	8470	6540	4730	2830
		Inc 6	Inc 7	Inc 8	Inc 9	Inc 10
		2910	970	2590	910	690

Table 3.5: Inflation of an elastomeric plate: Needed iterations per loading step

The calculation converges despite the complex behavior. We observe in the table 3.5 a number of iterations much higher for the first increment, and then a big regular decreasing of the number of iterations, in opposition to the case of linear elasticity. The reason is that the weak initial stiffness of the material leads to a very big displacement at the first increment. Then, the material rigidifies and the displacements per increment decrease importantly. The observed evolution of the number of necessary iterations in function of the loading step is therefore logical.

3.2.4 Conclusions and discussion

We presented two proposed formulae to extend Barnes-Han-Lee's dynamic relaxation method with kinetic damping. Barnes-Han-Lee's method was limited to the particular

case of linear triangular elements and elastic behavior. Our proposed formulae allow for applications beyond the original limitations. This is our main contribution.

Furthermore, we have numerically demonstrated several other advantages of our formulae. We showed our proposals are effective for 2D and 3D elements, with linear and quadratic interpolation. We showed the formulae are compatible with an incremental formulation, which minimizes the influence of the loading path. Our exploratory work showed that the second proposal works with a complex incremental law of behavior.

We present dynamic relaxation with kinetic damping, using the incremental formulation, as a useful alternative to the classic Newton's method in the cases where instabilities are found.

This work covered structural instabilities. In future work, the study will continue with material instabilities.

3.2.5 Acknowledgements

This work is financed by *Région Bretagne*, and in collaboration with the Navimo Society. We thank both of them their support and collaboration, that made it possible.

3.3 Comparison of several dynamic relaxation methods in the case of large displacements of membrane structures

J. Rodriguez, G. Rio, J.M. Cadou

Abstract: In the field of form-finding, the dynamic relaxation (DR) method is widely used. The classic form of DR uses an artificial viscosity to damp the movement. However, some authors use a kinetic damping instead. Several authors have presented different improvements on both DR methods in the last years, but no comparisons between them can be found in the case of membrane structures. The aim of this paper is to compare DR with viscous damping and DR with kinetic damping, using several existing formulations, and in the particular case of large displacements of membrane structures. Also, we propose two new formulations for the DR with kinetic damping.

Keywords: Dynamic relaxation; inflatable structures ; membrane structures; form-finding

Published: Submitted to Mechanics Research Communications

3.3.1 Introduction

When doing simulations by the FE method, in certain cases the basic Newton-Raphson algorithm cannot achieve a final solution due to instabilities like structural ones, which lead to a singular stiffness or the swapping between several stable states. Usually, explicit time schemes overcome this difficulty, but they need a huge number of time steps to obtain a realistic stable final shape. This occurs when using natural damping. This issue has been solved in several papers by using the method of Dynamic Relaxation (DR); some examples are the works carried out by Han and Lee [21], Wu [22], Ramesh [23], Russell [24] or Wood [25].

The DR method consists in considering that the mass of a structure is concentrated at the nodes. Then, a static problem is converted into a dynamic problem by the application of pseudo masses and viscous damping at the nodes. The static final form of the structure does not have to depend on the inertial forces that act during the transient evolution. Considering this, the mass is calculated so that the solution is achieved as fast as possible. A correct choice of the DR method parameters leads this way to an optimal convergence of the method.

The classic form of the dynamic relaxation uses an artificial viscosity to damp the movement (a comprehensive review can be read in Rezaee-Pajand [26, 27], the LS-DYNA theory manual by Hallquist [28], or the recent works of Joldes [29], for example). However, this is not the only existing DR method. Another interesting proposal is the DR method

introduced by Barnes [30], who combined the calculation of fictitious masses with a kinetic damping instead of the viscous damping.

Therefore, there are two main ways of working with the DR method:

- Dynamic Relaxation combined with Kinetic Damping (KDR)
- Dynamic Relaxation combined with Viscous Damping (ordinary DR)

Some authors use KDR and some other authors use the oDR, but it is difficult to find comparisons between both methods in the literature and it cannot be told a priori whether a method is better than the other or not for a particular application. Therefore, the aim of this paper is to compare both types of DR, and we focus the comparison in the particular case of inflatable membrane structures. A first brief comparison between KDR and some proposals of DR with viscous damping can be found in one of the latest works of Rezaee-Pajand [31] in the case of tensegrity structures. Our intention is to extend this comparison to large displacements in the domain of inflatable membrane structures. These large displacements are, for instance, due to smooth boundary conditions, and they can lead to an unstable final shape containing wrinkles.

In a first section, we will present the DR methods we will use. Then, we will present a set of numerical results, starting by a validation of the implementation of the DR methods in our calculation software and following by the comparison of all the methods in the case of inflatable structures. This comparison includes the case of an incremental formulation. We will end up commenting the extracted conclusions.

3.3.2 DR methods

3.3.2.1 DR with kinetic damping (KDR)

The kinetic damping method was firstly introduced by Cundall [32]. In this method, the global kinetic energy of a structure is traced. When a structure is steady and immobile, its kinetic energy is equal to zero and acceleration forces are null. The kinetic damping method consists in resetting velocity to zero at each kinetic energy peak. This is done because the structure oscillates, and the kinetic energy peaks are supposed to occur close to the static equilibrium position. Then, the computation is restarted from the current configuration, but with zero initial velocity. This procedure is continued until the structure comes progressively to a static equilibrium position.

In our work, the calculation of equilibrium is always made in the final configuration, using the Cauchy's stress tensor and the Almansi's deformation.

A comprehensive analysis of the DR with a kinetic damping has been presented by Barnes [30]. He applied the KDR in the calculation of form-finding of prestressed cables and membranes. Later on, several other examples can be found, such as the works of Topping [33], who proposed an algorithm for parallel DR computation; Gosling [34] or Wakefield [35], who applied the KDR to the calculation of structural membranes; Barnes [36], in the calculation of tension structures; Adriaenssens [37], Domer [38] or more recently Ali [39, 40], who studied tensegrity structures; Douthe [41], who applied it to

the study of composite grid shells; Troufflard [42], who applied it to the form-finding of inflatable structures; and also Han and Lee [21, 43], in a first paper to study the stabilizing processes of unstable structures and then in another one to trace the post-buckling equilibrium path of structures.

For the calculation of the mass matrix, we propose two methods, presented in the following subsections.

Proposal 1: KDR1 The first proposed method is based on the works of Barnes [30] and Han and Lee [21]. Barnes worked with cable structures, and Han and Lee proposed an expression to calculate the lumped pseudo-mass at each node i , improved later on in reference [42]. The mass matrix was then calculated as:

$$m_i = \lambda \frac{\Delta t^2}{2} k_{i_{max}} \quad \text{with} \quad k_{i_{max}} = \sum_e \frac{h}{4} \left(\frac{E}{1-\nu^2} + \sigma_x + \sigma_y + \sigma_{xy} \right) \quad (3.17)$$

being "h" the thickness of the material, and E and ν the Young modulus and Poisson ratio; Δt is fixed to 1 and λ is an adjustable parameter used to avoid instability.

Based on this equation, we propose to use a different expression for $k_{i_{max}}$ in order to extend its applicability to any type of membrane element and virtually any kind of behavior:

$$k_{i_{max}} = \sum_e \frac{l_e}{4} \left(\alpha K + \beta G + \gamma \frac{I_\sigma}{3} + \frac{\theta}{2} \sigma_{mises} \right) \quad (3.18)$$

Looking at the expression (3.17), the part $\frac{E}{1-\nu^2}$ can be considered as controlling the shape changing or the element's volume changing. It can be replaced by a linear combination of the average compressibility modulus K and shear modulus G , usually available for elastic and hyperelastic laws: $\alpha K + \beta G$. Concerning the second part of the term $k_{i_{max}}$, $(\sigma_x + \sigma_y + \sigma_{xy})$ can be considered as representing the stress state in the material (cumulating the spheric and deviatoric aspects). For our proposal, and in order to extend the use of the formula for other geometry than triangular elements, we replace this term by a combination of invariants: $\gamma \frac{I_\sigma}{3} + \frac{\theta}{2} \sigma_{mises}$, where $I_\sigma = \sigma_k^k$ is the trace of the Cauchy stress tensor and σ_{mises} is the Mises stress that represent the intensity of the spherical and the deviatoric parts of the stress tensor, respectively. These two quantities are tensor invariants and can be calculated independently of the type of element.

This first proposal includes Barnes and Han-Lee proposals.

Proposal 2: KDR The second proposal refers to the theoretical elements proposed by the early work of Underwood [44] by using the circle theorem of Gershgorin which permits to obtain an upper bound to the eigenvalue "i" of the stiffness matrix "K" of the system. The mass matrix is then built to satisfy the stability condition with an unitary time step. The stiffness in the normal direction of a flat membrane is null. In order to avoid a zero

value for the virtual-mass in this direction we choose the maximum value over the 3 axes:

$$m_i = \frac{\lambda}{2} MAX_{k=1}^3 (\rho_{3(i-1)+k}) \quad \text{with} \quad \rho_i \leq \sum_j |K_{ij}| \quad (3.19)$$

Unlike the physical masses, we can expect a variation of the mass matrix built this way during the calculation. Given that on one side we choose the maximum value over the 3 axes and on the other side the stiffness of the initial material behavior is generally more important than during deformation, it has been proved in our simulations that the mass matrix calculated at the beginning was enough to "guide" the whole simulation, i.e. the update of the mass matrix along the calculation of our simulations did not lead to any improvement.

3.3.2.2 DR with viscous damping

This is the classic form of DR method; it has been used by multiple authors and it is also used in some commercial FE softwares such as LS-DYNA [28]. Most of the references using DR with viscous damping are based on the works of Underwood [44].

We can find examples of DR with viscous damping in several fields: Bardet [45] applied it to the simulation of granular materials; Ramesh [23] studied plates and shallow shells; Wood [25] or Hegyi [46] used it to calculate membranes; Joldes [29] applied DR with viscous damping to biomechanical models; Kadkhodayan [47] combined a variant of this method (DXDR) with a modified fictitious time (MFT) step; and many others, like Turvey [48, 49], Salehi [50], Alshawi [51], Ghelli [52] or Kilic [53], who have found DR with viscous damping suitable for their simulations.

Some authors have also worked with materials with complex laws of behavior: Oakley [54], Zhang [55], Teng [56], Frieze [57], Kadkhodayan [58], Pasqualino [59] and Dang [60] are some examples.

Finally, Rezaiee-Pajand [61, 27, 31, 62] has recently made a interesting review of most of the references concerning the dynamic relaxation method, and he has also made contributions that we will use in our numerical case studies.

In the case of DR with viscous damping, and considering a fixed time step (usually arbitrary fixed to 1), two elements must be calculated: the mass matrix and the critical damping coefficient (the damping factor that causes the structure to approach the static position most rapidly). Several proposals for the calculation of both elements can be found in the literature, and we will focus on those that have been presented as the most interesting.

Most of the authors calculate the mass following the proposition of Underwood. However, some authors use alternative formulations: for example, Kommineny [63] uses the diagonal terms of the linear stiffness matrix as diagonal coefficients of the diagonal fictitious mass matrix; and Topping [33] uses the fictitious mass matrix proposed by Barnes [30]. Other authors, like Dang [60], fix the mass matrix to its real value and adjust the time step based on the changes in the element consistent tangent stiffness.

Reminder of the Dynamic Relaxation Method presented by Underwood

Dynamic relaxation is based on the second-order Richardson method [10]. Then, we can write the second order time dependent equation [44] the same way it has been previously presented, but including in this case a viscous term:

$$\mathbf{M}\ddot{X} + \mathbf{C}\dot{X} + \mathbf{P}(X) = \mathbf{f}(t) \quad (3.20)$$

where X, \dot{X}, \ddot{X} are the vectors displacement, velocity and acceleration, respectively. Notice that $\mathbf{C}\dot{X} + \mathbf{P}(X) - \mathbf{f}(t) = R(X, \dot{X})$. To solve the problem in time, the explicit centered finite differences method (CFD) is used. To preserve the explicit form of the CFD integrator, the mass matrix \mathbf{M} and the damping matrix \mathbf{C} must be diagonal. For dynamic relaxation, \mathbf{C} is chosen with the form is: $\mathbf{C} = c \cdot \mathbf{M}$. So we can write:

$$\mathbf{M}\ddot{X} + c\mathbf{M}\dot{X} + \mathbf{P}(X) = \mathbf{f}(t) \quad (3.21)$$

The expressions used for the temporal derivatives are:

$$\dot{X}^{n+\frac{1}{2}} = \frac{X^n - X^{n-1}}{\Delta t} \quad (3.22)$$

$$\ddot{X}^n = \frac{\dot{X}^{n+\frac{1}{2}} - \dot{X}^{n-\frac{1}{2}}}{\Delta t} \quad (3.23)$$

$$\dot{X}^n = \frac{\dot{X}^{n+\frac{1}{2}} - \dot{X}^{n-\frac{1}{2}}}{2} \quad (3.24)$$

If we substitute the expressions (3.22), (3.23) and (3.24) in (3.21), we obtain²:

$$\dot{X}^{n+\frac{1}{2}} = \frac{\mathbf{M}/\Delta t - c\mathbf{M}/2}{\mathbf{M}/\Delta t + c\mathbf{M}/2} \dot{X}^{n-\frac{1}{2}} + \frac{\mathbf{f}(t^n) - \mathbf{P}(X^n)}{\mathbf{M}/\Delta t + c\mathbf{M}/2} \quad (3.25)$$

$$X^{n+1} = X^n + \Delta t \dot{X}^{n+\frac{1}{2}} \quad (3.26)$$

Simplifying the mass terms in the equation:

$$\dot{X}^{n+\frac{1}{2}} = \frac{2 - c\Delta t}{2 + c\Delta t} \dot{X}^{n-\frac{1}{2}} + \frac{2\Delta t \mathbf{M}^{-1}(\mathbf{f}(t^n) - \mathbf{P}(X^n))}{2 + c\Delta t} \quad (3.27)$$

$$X^{n+1} = X^n + \Delta t \dot{X}^{n+\frac{1}{2}} \quad (3.28)$$

Since matrix \mathbf{M} is diagonal, we can write for each vector component:

$$\dot{x}_i^{n+\frac{1}{2}} = \frac{2 - c\Delta t}{2 + c\Delta t} \dot{x}_i^{n-\frac{1}{2}} + \frac{2\Delta t [f(t_i^n) - P(x_i^n)]}{m_{ii}(2 + c\Delta t)} \quad (3.29)$$

²These formulae reproduce exactly the presented in Underwood's work. The fact of including in the formulation the inverse of the mass matrix as it is made in that paper could be discussed, but we are only interested in the final resultant formulation, that we consider correct.

$$x_i^{n+1} = x_i^n + \Delta t \dot{x}_i^{n+\frac{1}{2}} \quad (3.30)$$

There are now in these formulae three parameters that must be defined: the fictitious mass matrix \mathbf{M} , the damping coefficient c and the time step Δt .

Concerning the time step; although there are also some authors like Kadkhodayan [47] that use a modified Δt applied to the calculation of truss structures and plate bending (obtaining good improvements in the number of iterations), we will follow the suggestion of Underwood [44]. The time step is "coupled" with the mass. It is arbitrarily chosen as 1 and then the stability is managed by a good choice of the mass matrix.

Therefore, the parameters to calculate are the mass matrix and the damping coefficient.

Fictitious mass matrix

Fixed the time step, the mass matrix and the damping coefficient must be chosen in order to guarantee the stability and good convergence of the iterations. We will present now the different formulations implemented in Herezh++. Virtually any of the implemented mass matrix formulations could be used with DR with kinetic or viscous damping.

Underwood's proposal We will also use the fictitious mass proposed by Underwood [44] based on Gerschgorin's theorem, that having a mathematical basis, it is supposed to have efficient results. Also it has been widely used by many authors, being effective for many types of non-linear problems.

$$m_{ii} \geq \frac{(\Delta t)^2}{4} \sum_j |K_{ij}| \quad (3.31)$$

where K_{ij} are the elements of the global tangent stiffness matrix $[K]$.

Rezaiee-Pajand's proposal Another interesting formulation for the fictitious mass matrix can be found in the work of Rezaiee-Pajand [27, 31], who, based on an error analysis proposed the following formulation that he proved to be valid in several linear and geometrically non-linear examples. He denotes it as mDR :

$$m_{ii} = \max \left[\frac{(\Delta t)^2}{2} K_{ii}, \frac{(\Delta t)^2}{4} \sum_j |K_{ij}| \right] \quad (3.32)$$

where K represents again the global tangent stiffness matrix.

Mass matrix updates

Structural and eventual material non-linearities can produce changes in the stiffness of the structure. In order to keep the stability, it could be necessary to update the fictitious mass

matrix. Underwood proposes to use a criterion based on the perturbed apparent-frequency error measure. The error is calculated with:

$$\epsilon = \max_i^{n_{\text{dof}}}(\epsilon_i) \quad , \quad \epsilon_i = \frac{(\Delta t)^2}{4} \frac{|\Delta \ddot{X}_i|}{|\Delta X_i|} \quad (3.33)$$

where $\Delta \ddot{X}_i$ is the variation of acceleration for the degree of freedom i , and ΔX_i is the variation of the position. Then, ϵ_i is evaluated and, based on its value, the mass matrix is eventually recalculated or the time step decreased. If ϵ_i is greater than one, it would mean that the estimated upper-bound for the maximum apparent-frequency has been exceeded and the mass matrix must be recalculated to keep the stability. The same way, if the value of ϵ_i is much smaller than one, it would mean that we are being too conservative, and the convergence could be improved. All this has also been implemented in Herezh++.

Damping coefficient

The critical damping coefficient is the damping factor that causes the structure to approach the static position most rapidly. One possible solution (Dang [60]) to obtain this coefficient would be to estimate it by doing an undamped run of the calculation to estimate the highest frequency and then using the expression given by Biggs [11] for a 1-D system: $C_i = 2\sqrt{S_i M_i}$. However, this is not the common method used in the literature since it would require the calculation to be launched twice. Other authors, as Papadrakakis [12] propose an automatic identification of the parameters of DR. We will be based in the works of Underwood. All the following estimators for the damping coefficient are implemented in Herezh++ and have been used.

Underwood's proposal Usually, the value of critical damping coefficient is estimated by using the lowest frequency of the system. The following expression is used:

$$c = 2\omega_0 \quad (3.34)$$

where ω_0 is the lowest frequency of the system.

In order to find the vibration properties of a structure, the following matrix eigenvalue problem must be solved:

$$\mathbf{K}\Phi = \lambda\mathbf{M}\Phi \quad (3.35)$$

The eigenvalues $\lambda_n (\equiv \omega_n^2)$ are the roots of the equation (it can be read, for example, in Chopra [13]):

$$p(\lambda) = \det(\mathbf{K} - \lambda\mathbf{M}) = 0 \quad (3.36)$$

where $p(\lambda)$ is a polynomial of order n_{dof} (number of degrees of freedom or the system). Since this would be very expensive to calculate especially for large systems, other methods

are preferred. Most of the authors use the Rayleigh method and so we do (some authors, as Rezaiee-Pajand [31] propose to use the Stodola method, though).

If the equation (3.35) is multiplied by Φ^T :

$$\Phi^T \mathbf{K}\Phi = \omega^2 \Phi^T \mathbf{M}\Phi \quad (3.37)$$

then, solving for ω^2 :

$$\omega^2 = \frac{\Phi^T \mathbf{K}\Phi}{\Phi^T \mathbf{M}\Phi} \quad (3.38)$$

what is called Raileigh's quotient. Therefore, if we apply this to our system to find an approximation to its lowest frequency, we can write:

$$\omega_0^2 \approx \frac{\Delta X^T \mathbf{K}\Delta X}{\Delta X^T \mathbf{M}\Delta X} \quad (3.39)$$

In non-linear systems, since \mathbf{K} it cannot be accessed to use it directly in the calculation, it can be calculated as following (and this is the method implemented in our calculation software):

$$\bar{\mathbf{K}}_{ii}^n = \frac{\Delta R_i^n}{\Delta t \dot{X}_i^{n-\frac{1}{2}}} \quad (3.40)$$

where ΔR_i^n is the static residual and $\bar{\mathbf{K}}_{ii}^n$ represents the diagonal estimators of the directional stiffness.

Rezaiee-Pajand's proposal Rezaiee-Pajand [27], from his error analysis of the DR, proposes the following expression for the critical damping coefficient estimation:

$$c = \sqrt{4\omega_0^2 - \omega_0^4} \quad (3.41)$$

For the estimation of ω_0 , the lowest frequency of the structure, he proposes two different methods: one based in Rayleigh's quotient, exactly as shown in section 3.46, described in Rezaiee-Pajand [27]; and another method, described in Rezaiee-Pajand [31], based on the Stodola iterative process (previously explained, for example, by Clough [14]). The Stodola method is more precise than Rayleigh method because it is an iterative method instead of an estimation, but the cost of calculation can be much higher, since the inverse of the stiffness matrix has to be calculated frequently. Due to this, the Stodola method has not been implemented in Herezh++.

Qiang's proposal Qiang [64] is based on a minimization of the displacement error and the use of Gerschgorin's theorem to propose the equations to be satisfied :

$$m_{ii} = \sum_j |k_{ij}(x^n)|$$

$$\omega_0 = \frac{(x^n)^T \mathbf{K}(x^n)x^n}{(x^n)^T \mathbf{M}x^n} \tag{3.42}$$

$$ch = \frac{4\sqrt{\omega_0}}{1 + \omega_0}$$

$$h = \frac{2}{\sqrt{1 + \omega_0}}$$

From these equation we can deduce his expression for the estimated critical damping:

$$c = 2\sqrt{\frac{\omega_0}{1 + \omega_0}} \tag{3.43}$$

Then, for the estimation of the lowest frequency ω_0 , he also proposes to use Rayleigh's quotient, as described in 3.46.

For our numerical examples and subsequent comparison, we implemented in our calculation software the classical formulation of Underwood and also the latest formulations of Rezaiee-Pajand. We also implemented the formulation of Qiang for the critical damping coefficient.

Implemented mass matrix formulations Denoting with K_{ij} the elements of the global tangent stiffness matrix $[K]$, the proposals we implemented to calculate the mass matrix with $m_i = \lambda \frac{\Delta t^2}{2} k_{i_{max}}$ are:

$$\text{Underwood [44]} : k_{i_{max}} = \sum_j |K_{ij}| \tag{3.44}$$

$$\text{Rezaiee-Pajand [27, 31]} : k_{i_{max}} = \max \left[2 K_{ii}, \sum_j |K_{ij}| \right] \tag{3.45}$$

Implemented critical damping coefficient formulations Denoting with ω_0 the lowest frequency of a system, the proposals we implemented to calculate the critical damping coefficient are:

$$\text{Underwood [44]} : c = 2\omega_0 \tag{3.46}$$

$$\text{Rezaiee-Pajand [27, 31]} : \quad c = \sqrt{4\omega_0^2 - \omega_0^4} \quad (3.47)$$

$$\text{Qiang [64]} : \quad c = 2\sqrt{\frac{\omega_0}{1 + \omega_0}} \quad (3.48)$$

The lowest frequency is calculated in all the cases with the Rayleigh's quotient, that Zhang [65] presented as the most advantageous method (being X the vector position):

$$\omega_0^2 \approx \frac{\Delta X^T \mathbf{K} \Delta X}{\Delta X^T \mathbf{M} \Delta X} \quad (3.49)$$

3.3.2.3 Notation

In order to establish an unambiguous notation for all the implemented methods, we will keep consistent with the literature for the existing methods:

- *Methods of DR with kinetic damping*: KDR1 if our proposal 1 is used for the mass term; KDR if our proposal 2 is used.
- *Methods of DR with viscous damping*: oDR when using formulae (3.44) and (3.46); mDR when using (3.45) and (3.46); mdDR when using (3.45) and (3.47); uqDR when using (3.44) and (3.48); and pqDR when using (3.45) and (3.48).

3.3.2.4 Incremental scheme and convergence criterion

The final state of a structure can depend on the loading path (this is the case when using an incremental law of behavior, for example). But the loading path of DR can be very different to the real path. A solution is to use an incremental loading procedure. Assuming that increments are small enough, the procedure then guarantees a succession of points of static physical equilibrium that allow to be close to the real response of the structure during a quasi-static loading.

The convergence criterion we use in the calculations is the following, being ε the instruction value:

$$\text{Max} \left(\frac{\| \text{Static Residual} \|_\infty}{\| \text{Static Reactions} \|_\infty}, \frac{\text{Kinetic Energy}}{\text{Internal Energy}} \right) \leq \varepsilon \quad (3.50)$$

with "static" referring to residual force without inertia and viscosity forces.

3.3.3 Numerical case studies

We will present in the following subsections a set of numerical case studies comparing the different DR methods. We use the C++ academic finite elements software Herezh++ [18], and for the meshing and postprocessing, we use the software Gmsh [66]. Calculations are made on an Apple computer (Processor: 2x2.93 GHz Quad-Core Intel Xeon, Memory: 16 Gb 1066 MHz DDR3) with just one processor.

Since the time step is arbitrarily fixed to 1, the control of the stability depends on the parameter λ . This parameter has already been introduced in the field of DR by Barnes and Han-Lee. If we consider for instance the formule (3.44) and we compare it with the one presented by Underwood [44], we can deduce the relation between λ and the time step: $\lambda/2 = (\Delta t)^2/4$. This expression leads to a minimum theoretical value of $\lambda = 0.5$. However, due to different approximations, a smaller value of λ could eventually be used. The smaller λ is, the closer to the critical Δt we are (and in consequence, the instability is nearer).

Since the mass calculated for KDR1 is not based on Gerschgorin's theorem as all the other used DR methods, the range of values for λ is different and it has to be presented separately.

In these particular case studies, the methods oDR, mDR and mdDR appeared to be equivalent, giving exactly the same number of iterations in all the calculations, so their results are presented altogether. The same happened for the methods uqDR and pqDR.

In the numerical case studies, we will firstly validate the implementation of the DR methods and then we will compare the DR methods in three different parts: a first part focusing the comparison in the study of squared and circular meshes with different elements' characteristics. Then, we will make a comparison in the case of an incremental calculation and also when we vary the precision of the calculation. Finally, we will present the comparison in the case of calculation of a complex geometry, as a benchmark.

3.3.3.1 Validation

Before carrying out all the calculations, we considered important to validate the implementation in Herezh++ of the different DR methods, in order to be sure that calculations will be correct. For that, we made a calculation previously carried out by Wu [22] in order to compare our results with his. It consists in the inflation of an airbag made of two squared membranes joined along their perimeters.

As Wu indicates in the section 5.4 of his paper [22], the mesh size is 1x1 m. We carried out the calculation with the finest mesh proposed in the paper: the one with 1600 (40x40) rectangular elements. As well as in his paper, the material properties were: $\rho = 2,7 \times 10^2 \text{ kg/m}^3$, $E = 7 \times 10^4 \text{ Pa}$, $\nu = 0.3$ and the thickness of the membrane $h = 1 \times 10^{-5} \text{ m}$. A symmetry was considered and only the superior membrane was calculated. A followed pressure $P = 0.03 \text{ Pa}$ was applied to simulate the inflation. Since in DR the transient path is false, we did not care about the time of application of the pressure, we have just searched the final shape to compare them.

We made the calculations with both types of damping (kinetic and viscous). We present results obtained with KDR (Figure 3.10) and mdDR (Figure 3.11). As we can observe in both figures, the result is very close to Wu's result (presented on the left side of each figure).

It can be observed in the figures that displacements are very similar, and even though Wu did not specified the precise values, we can see in the scales that they are almost the same. For the maximum displacement (the top of the airbag), we obtained with both

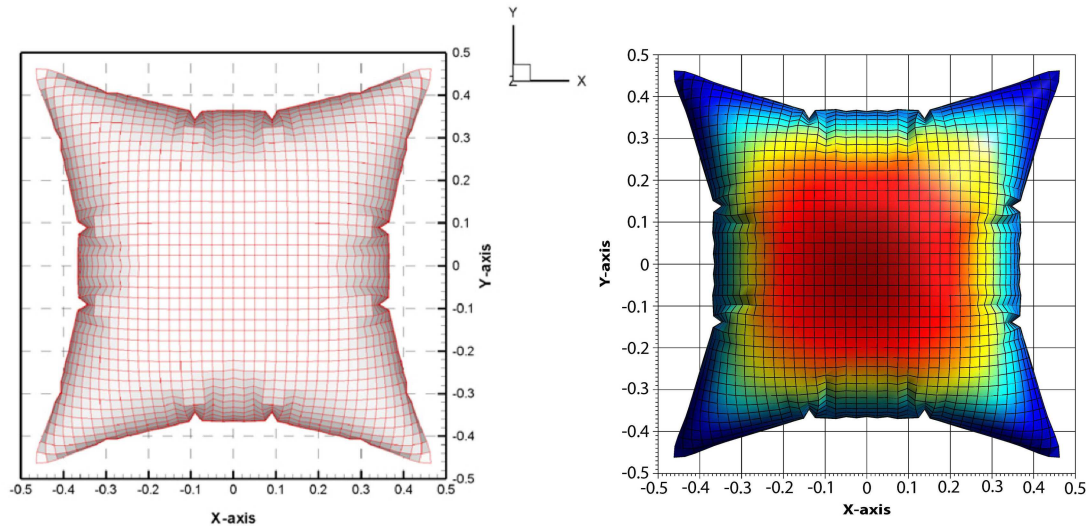


Figure 3.10: Comparison between the airbag calculated by Wu [22] (left) and the same mesh calculated by us (right) using the KDR method

KDR and mdDR methods a value of 0.259 m, what is in concordance with the value obtained by Wu and presented in his paper.

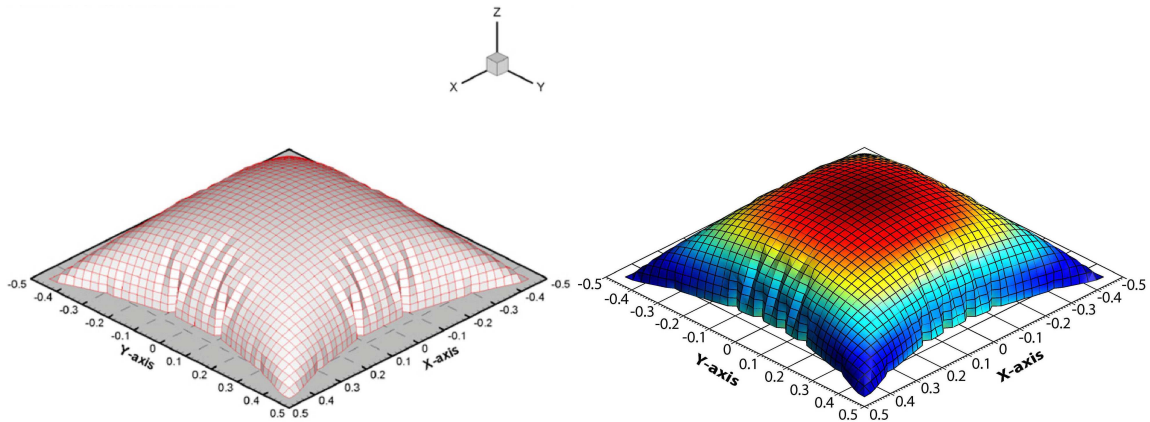


Figure 3.11: Comparison between the airbag calculated by Wu [22] (left) and the same mesh calculated by us (right) using the mdDR method

We can also observe in the figures that even the distribution of wrinkles is also quite similar. Since this is an unstable structure, wrinkles are not positioned exactly in the same places (there is even a small difference between the result using kinetic damping and the result using viscous damping), but they are in a good agreement with the literature.

Seen these results, we can confirm that our results are consistent.

3.3.3.2 Squared and circular meshes: different types of elements and interpolation

We study here 2D squared meshes with triangular (T) and rectangular (R) elements with linear (L) and quadratic (Q) interpolations, and also a circular mesh with a mix of triangular and rectangular elements. We also make tests for two different qualities of mesh: a grid of 25×25 elements (1) and another one of 50×50 (2). For the KDR1 method, we use the parameters $\alpha, \beta, \gamma, \theta = 1$. The calculation is carried out in linear elasticity, $E = 125MPa$ and $\nu = 0.41$, which are coherent with the parameters of behavior of a usual thin fabric. As an example, the notation RL1 means: test made with a mesh with 25×25 Rectangular elements, and using Linear interpolation.

The numerical tests consist in the inflation of a squared or circular air bag. The air bags consist in two membranes joined at their periphery, with dimensions $500mm \times 500mm \times 0.27mm$ in the case of the squared mesh, and diameter 400 mm for the circular one. Due to the symmetries, just $1/8$ of the squared air bag is studied (and $1/2$ in the case of the circular air bag). The air bag is loaded with an instantaneous internal pressure of 0.015 MPa. When it is not precised, the convergence criterion is set to: $\varepsilon = 1 \times 10^{-3}$

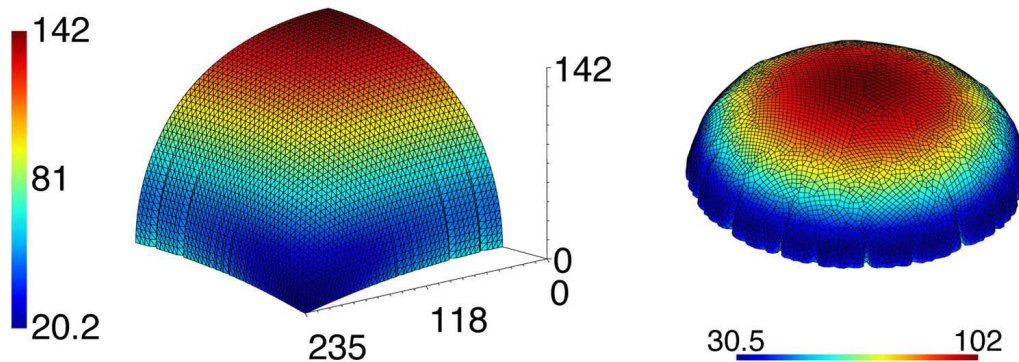


Figure 3.12: Field of displacement of an inflated squared air bag (left) and an inflated circular air bag (right)

Since it would be very long to present all the results, we present the three most representative (given their difference) calculations: for the cases TL1, RQ2 and circular mesh, in Tables 3.6 and 3.7 ³.

Added data: Tables 3.8 to 3.13 show all the results that were not presented in the paper in the original submission to the journal *Mechanics Research Communications*.

³In all the presented tables, "div" means divergence

TL1	DR method \ $\lambda =$	5	6	7	8	9	10	11	12	13	14	15	
	KDR1	div	div	div	div	div	599	555	570	621	756	685	678
TL1	DR method \ $\lambda =$	0,5	0,6	0,7	0,8	0,9	1	1,1	1,2	1,3	1,4	1,5	2
	KDR	div	518	799	906	927	719	759	1019	1065	1138	1115	1473
	oDR, mDR, mdDR	561	659	654	697	736	774	812	832	865	898	929	1074
	uqDR, pqDR	div	div	div	div	div	3685	3960	4228	4492	4750	5004	6215

RQ2	DR method \ $\lambda =$	5	6	7	8	9	10	11	12	13	14	15	
	KDR1	div	div	div	1582	1729	1915	2066	2068	2139	2189	2467	
RQ2	DR method \ $\lambda =$	0,5	0,6	0,7	0,8	0,9	1	1,1	1,2	1,3	1,4	1,5	2
	KDR	2035	2021	2189	2425	2622	2572	2829	2822	3403	3047	3436	3677
	oDR, mDR, mdDR	1749	1918	2088	2249	2478	2620	2705	2825	2940	3114	3436	3948
	uqDR, pqDR	div	div	div	>15k								

Table 3.6: Number of iterations in the calculation of meshes TL1 and RQ2 for each DR method (squared meshes)

CIR	DR method \ $\lambda =$	5	6	7	8	9	10	11	12	13	14	15	
	KDR1	div	2767	2860	2191	2262	2291	2466	4445	2353	2819	2956	
CIR	DR method \ $\lambda =$	0,5	0,6	0,7	0,8	0,9	1	1,1	1,2	1,3	1,4	1,5	2
	KDR	1542	1703	1857	1953	2068	2053	2300	2306	2220	2487	2585	2673
	oDR, mDR, mdDR	div	div	2342	2553	2700	2835	3023	3163	4144	3451	3772	3468
	uqDR, pqDR	div	div	div	11105	12105	13070	14012	14936	13720	14490	>15k	>15k

Table 3.7: Number of iterations in the calculation of the circular mesh for each DR method

TL2	DR method \ $\lambda =$	5	6	7	8	9	10	11	12	13	14	15	
	KDR1	div	div	div	div	1127	1201	1206	1089	1431	1191	1293	
TL2	DR method \ $\lambda =$	0,5	0,6	0,7	0,8	0,9	1	1,1	1,2	1,3	1,4	1,5	2
	KDR	div	1090	1081	1646	1187	1420	1300	1607	1440	1796	1685	2016
	oDR, mDR, mdDR	1026	1118	1188	1252	1317	1379	1446	1511	1588	1649	1707	1965
	uqDR, pqDR	div	div	div	div	div	8955	10516	11129	11746	12363	12975	>15k

Table 3.8: Number of iterations in the calculation of mesh TL2 for each DR method

3.3.3.3 Squared mesh in incremental calculations and calculations with different precisions

For this comparisons, we considered the mesh TL1; the pressure is applied following a linear slope from 0 to 0.015 MPa and the calculation is made in 10 increments. The figure 3.13 (left) shows the number of iterations taken by each method for each increment. It

TQ1	DR method \ $\lambda =$	5	6	7	8	9	10	11	12	13	14	15	
	KDR1	div	div	div	div	div	div	div	1200	1310	1363	1376	
	DR method \ $\lambda =$	0,5	0,6	0,7	0,8	0,9	1	1,1	1,2	1,3	1,4	1,5	2
	KDR	div	1205	1246	1301	1383	1674	1618	1733	1775	2032	1914	2319
	oDR, mDR, mdDR	div	1216	1312	1404	1490	1571	1648	1722	1793	1861	1926	2226
uqDR, pqDR	div	div	div	div	div	10169	10923	11660	12383	13091	13787	>15k	

Table 3.9: Number of iterations in the calculation of mesh TQ1 for each DR method

TQ2	DR method \ $\lambda =$	5	6	7	8	9	10	11	12	13	14	15	
	KDR1	div	div	div	div	div	div	div	div	1972	2061	2207	
	DR method \ $\lambda =$	0,5	0,6	0,7	0,8	0,9	1	1,1	1,2	1,3	1,4	1,5	2
	KDR	div	2326	2413	2709	2815	2886	3051	3333	3230	3461	3631	4212
	oDR, mDR, mdDR	div	2275	2459	2629	2789	2940	3084	3220	3352	3458	3602	4161
uqDR, pqDR	div	div	div	div	>15k								

Table 3.10: Number of iterations in the calculation of mesh TQ2 for each DR method

RL1	DR method \ $\lambda =$	5	6	7	8	9	10	11	12	13	14	15	
	KDR1	497	547	477	501	533	568	641	594	569	652	691	
	DR method \ $\lambda =$	0,5	0,6	0,7	0,8	0,9	1	1,1	1,2	1,3	1,4	1,5	2
	KDR	553	484	619	596	692	637	598	746	685	757	809	992
	oDR, mDR, mdDR	div	490	530	567	601	634	665	695	724	751	777	898
uqDR, pqDR	div	div	div	2260	2470	2675	2875	3070	3261	3449	3634	4515	

Table 3.11: Number of iterations in the calculation of mesh RL1 for each DR method

RL2	DR method \ $\lambda =$	5	6	7	8	9	10	11	12	13	14	15	
	KDR1	874	792	738	887	934	1164	1074	992	1074	1045	1155	
	DR method \ $\lambda =$	0,5	0,6	0,7	0,8	0,9	1	1,1	1,2	1,3	1,4	1,5	2
	KDR	765	788	1183	1110	1156	1161	1585	1286	1589	1376	1300	1559
	oDR, mDR, mdDR	div	1015	1091	1143	1223	1268	1326	1383	1439	1503	1557	1806
uqDR, pqDR	div	div	div	6299	6889	7464	8026	8575	9113	9641	10160	12642	

Table 3.12: Number of iterations in the calculation of mesh RL2 for each DR method

can be seen that KDR1 and KDR appear to be much more efficient than oDR, mDR and mdDR, specially at the beginning. Indeed, to be able to obtain the results for oDR, mDR and mdDR, we had to increase the value of λ to avoid divergence, while with KDR1 and KDR we could keep the minimum (optimum) value obtained in the previous case study. We discard to present the results of uqDR and pqDR since the number of iterations is much higher and it would difficult the visibility of the results' plot.

RQ1	DR method \ $\lambda =$	5	6	7	8	9	10	11	12	13	14	15	
	KDR1	div	div	div	div	988	1020	1072	1112	1146	1260	1295	1286
RQ1	DR method \ $\lambda =$	0,5	0,6	0,7	0,8	0,9	1	1,1	1,2	1,3	1,4	1,5	2
	KDR	970	1053	1097	1177	1376	1299	1491	1456	1587	1617	1602	1956
	oDR, mDR, mdDR	971	1068	1206	1292	1373	1449	1521	1590	1657	1720	1782	2062
	uqDR, pqDR	div	div	div	7231	7900	8551	9186	9807	10415	11011	11597	14395

Table 3.13: Number of iterations in the calculation of mesh RQ1 for each DR method

Also, we compared the DR methods (in just one increment of calculation) in the case of different precisions, and we observed that the DR methods using viscous damping need an augmentation of λ to avoid divergence as we increase the precision, while the number of required iterations remains similar in both methods. Figure 3.13 (right) shows the needed λ for each kind of DR method (KDR or oDR,mDR,mdDR).

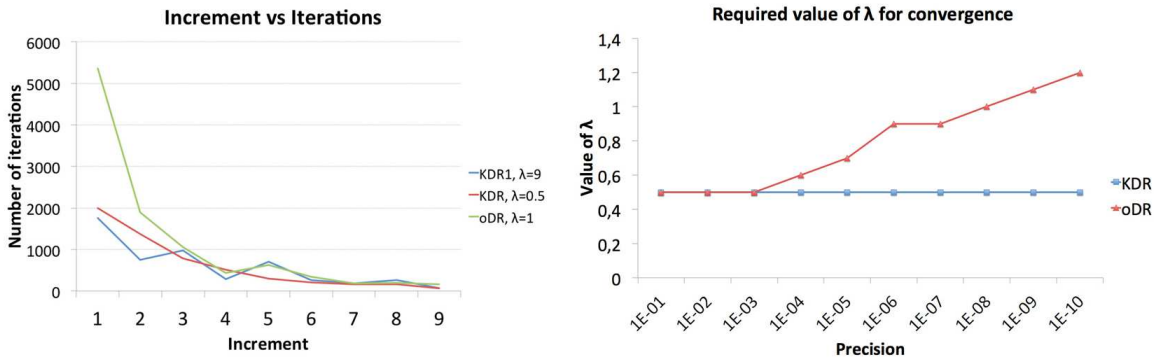


Figure 3.13: Number of iterations per increment (left) and needed λ for convergence (right).

We can conclude in this subsection that the KDR appears to be advantageous for high precision calculations and for incremental calculations.

3.3.3.4 Benchmark

As a benchmark, we have carried out a calculation with a random mesh without symmetries, in order to try to complicate the calculation to test the robustness of the DR methods and to compare them in the case of a complex calculation: we looked for a mesh that produced wrinkles, with angles, curves, no symmetries... The material properties are the same than in the previous calculations. The geometry and the obtained results are available in [67].

Once again it can be observed the clear advantage of DR methods when using kinetic damping instead of viscous damping.

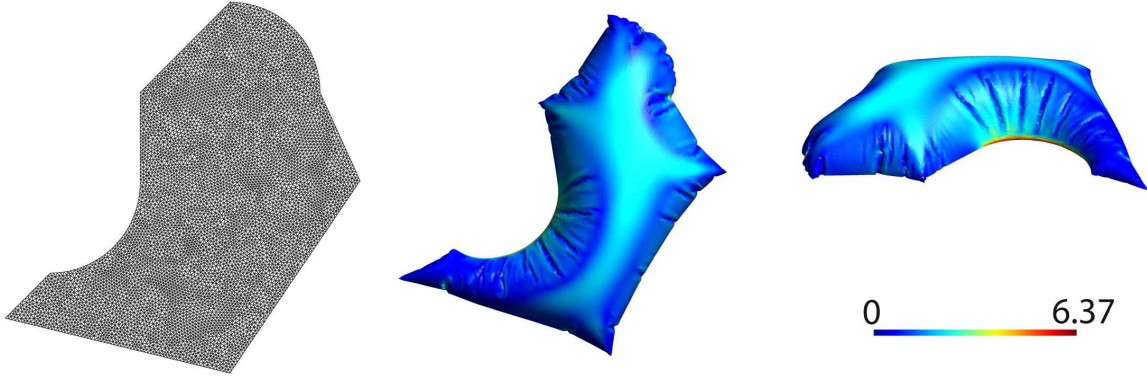


Figure 3.14: Benchmark mesh (left) and inflated result (right): Mises isovalues [MPa]

BEN	DR method \ $\lambda =$	5	6	7	8	9	10	11	12	13	14	15	
	KDR1	div	div	2481	1740	2556	3010	3164	3049	4170	3035	3514	
	DR method \ $\lambda =$	0,5	0,6	0,7	0,8	0,9	1	1,1	1,2	1,3	1,4	1,5	2
	KDR	2371	3338	3922	3212	3062	4212	5449	3482	4875	4978	5134	4675
	oDR, mDR, mdDR	div	div	4685	4427	4911	5458	5217	5962	6535	6208	6409	7483
	uqDR, pqDR	div	div	div	>15k								

Table 3.14: Number of iterations needed for each λ and DR method (benchmark mesh)

3.3.4 Conclusions and discussion

After the comparison we made between several DR methods with both kinetic and viscous damping, we can conclude *for our particular case studies*:

- Both DR with viscous damping and kinetic damping allow to obtain the final static state, with similar global numerical behavior.
- In the case of DR with viscous damping, a good choice of the critical damping coefficient is very important. We could observe that Qiang's proposal [64] is particularly inefficient compared with Rezaiee-Pajand's [27, 31] and Underwood's [44] proposals.
- We obtain the same of number of iterations between the calculations with the original proposal of Underwood [44] and the calculations with the modifications proposed by Rezaiee-Pajand [27, 31].
- In the case of DR with viscous damping, if we increase the precision of a calculation, we must increase λ to achieve the convergence, while in the case of KDR we can increase the precision and keep a fix lambda. KDR is therefore advantageous in the cases where a high precision is required.
- An advantage of DR with viscous damping against DR with kinetic damping is that the number of iterations always increases *regularly* as λ increases.

Added data: This conclusion can be observed looking at the results in the tables, but in order to illustrate it better, we present some results in the figure 3.15

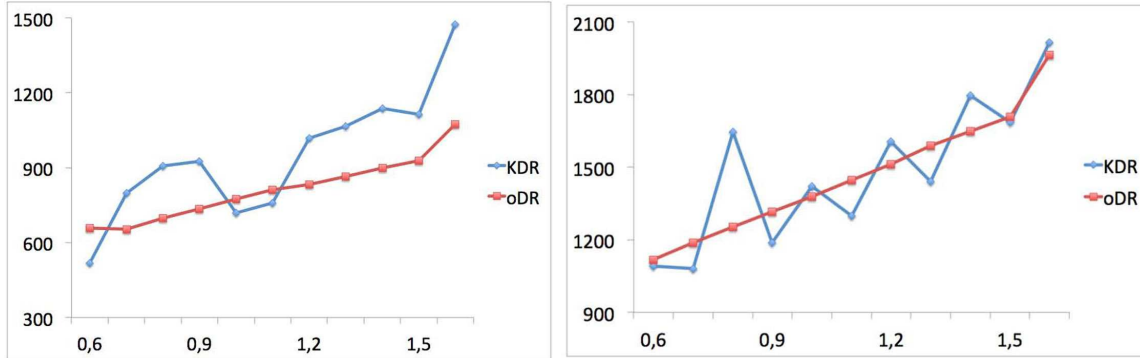


Figure 3.15: Needed number of iterations in function of lambda for KDR and oDR, for a TL1 mesh (left) and a TL2 mesh (right)

- The optimum number of iterations appears to be usually when we use the minimum possible λ , but it is not always the case (when this is not the case, the value of λ is anyway close to the minimum one).
- Once identified the optimum λ , the KDR1 method is often the most efficient among them all.
- When a mesh is complex (Benchmark) or when it is very unstable (incremental calculations), the DR with kinetic damping appears to be more efficient than DR with viscous damping.

3.3.5 Acknowledgements

The authors are grateful to *Région Bretagne*, *Conseil Général du Morbihan* and the *Navimo Society* for their financial support and collaboration, that made this work possible.

Chapter 4

3D measuring

4.1 Introduction

We showed in the previous chapter that the implementation made in Herezh++ of the different dynamic relaxation methods allowed to make calculations with an incremental loading (obtaining several points of static physical equilibrium). Therefore, and in the context of the form-finding of inflatable fabric structures, we could try to make a comparison of the transient part of a real inflatable structure and its numerical simulation.

Thus, in this chapter, we will present some experimental measurements made all along the inflation of an air bag made out of fabric. This fabric is the one used by Plastimo in the manufacturing of their lifejackets and other security items. This enterprise provided us with the air bag, consisting in two circular pieces of fabric welded together along their perimeters (resulting an effective diameter of 400mm), and also disposing of a tube in his bottom, where an air pump can be plugged to inflate it.

In his thesis works, Troufflard [1] had already made some measurements on this air bag, but his objective was different. His aim was to measure the final inflated form, while we are trying to measure the transient part. For his measurements, Troufflard used two different devices:



Figure 4.1: Coordinate-measuring machine (left) and Aramis' 3D optical system (right)
[Image sources: starequipment.net; uakroncivil.com]

- *A mechanical coordinate-measuring machine (figure 4.1, left)*: We discarded this option for this thesis work due to several reasons. Firstly, it is a system mainly conceived for rigid objects, because the probe needs to apply a certain pressure in the object, and even if a maximum force can be defined, this would originate deformations in the air bag's surface, specially during the inflation due to the low stiffness (further commented by Troufflard [1]). Then, the set-up of this machine is very complex, the measuring process is very long, and the post-treatment of the obtained data is also very complex. Finally, it is impossible to measure the transient part; even if we inflated the air bag with different pressures and measured at each one, at the lowest pressures the air bag wouldn't be rigid at all, resulting impossible to carry out the measuring.
- *3D measuring with the optical system Aramis[68] (figure 4.1, right)*: Aramis is a digital image correlation software able to measure displacements and strains without contact. This option was not suitable for this thesis work because the maximum shooting speed of the camera devices available in our laboratory was 2 images/second; and the inflation of the air bag is completed in around 1 second. Therefore, the transient part could not be measured. However, the measuring system would be appropriate if the shooting speed was faster, because it has the advantages of no needing a contact, high precision and also a relative ease of set-up and post-treatment of the data.

Since the 3D optical measuring system was the most convenient, we decided to combine the use of high-speed cameras (to take the pictures during the transient phase) and the software Aramis (to calibrate the cameras and process the taken images).

4.2 Description of the devices used in the measuring

The set up for the 3D optical measuring is as shown in the following simplified scheme: Therefore, the required devices included in the set-up are:

- A compressed air circuit that is connected to a pressure regulator (figure 4.3, left). The regulator allows to control the pressure inside the air bag, and it also has a probe to check the pressure. Any pressure value can be specified as a setpoint (up to the limit of the pressure probe, 0.035 MPa). Since we were working with a fabric used in inflatable lifejackets, and the air bag's size is in the same order of magnitude than them, we used a pressure setpoint in the same order of magnitude than inflatable lifejackets' one: 0.02 MPa. The air flow was set to a value that allowed the balloon to be inflated in around 1 second.
- Two high-speed cameras (figure 4.3, right). The camera model is Photron Fastcam SA5 [70]. Each one of these cameras is able to record at up to 1 million of images per second. Thus, they are the correct device to take pictures during the transient part. For our application, we have chosen a shooting speed that allowed to have

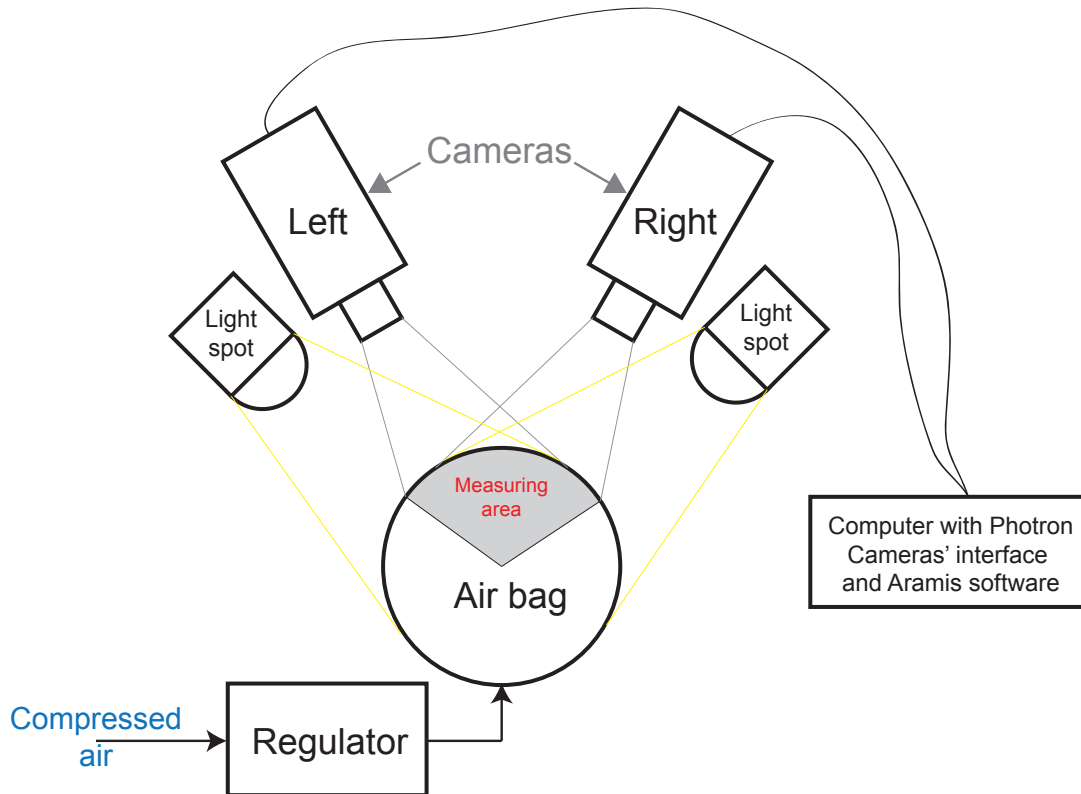


Figure 4.2: 3D optical measuring set-up

clear pictures during the inflation (otherwise, the Aramis software wouldn't be able to process them); 125 images/second appeared to be enough, a good compromise between luminosity, shooting speed and resolution. The objectives used in both cameras were SIGMA AF-MF ZOOM LENS 24-70 mm F2.8 EX DG MACRO, with a minimum focal distance of 40 mm. Since we needed to carry out a 3D measurement, we synchronized two cameras by means of a manual TTL trigger, since the timing is crucial at these recording speeds.

- Two light spots of 400 W pointing to the air bag (figure 4.3, right), since we needed optimal light conditions for the images to be processed by Aramis. At high shooting speeds, the aperture time is shorter, and then more light is needed to obtain a good contrast in the pictures.
- The cameras were linked to a laptop, where they were controlled by means of the interface software provided by Photron. Also, in that laptop, we disposed of the software Aramis 6.1 for the image treatment.
- Finally, the air bag itself. To carry out the measurement with Aramis, the sample must be prepared by painting it with a high-contrast stochastic pattern (see figure 4.3). We painted only the portion of the air bag visible by the cameras, since it

is the only part that would be processed by Aramis. First, we applied a uniform layer of white painting with a spray, and then, with another spray of black paint, we made random (in size and position) black dots.

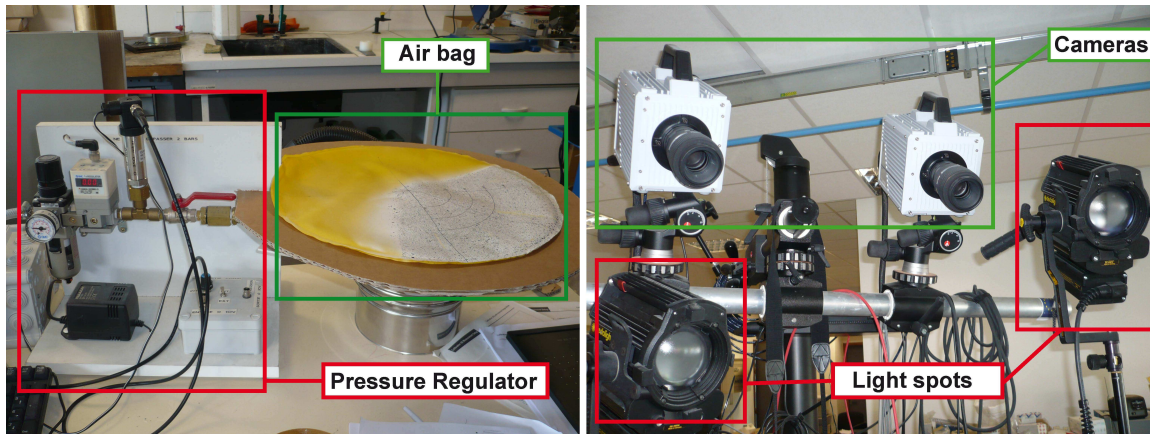


Figure 4.3: Pressure regulator, airbag, light spots and cameras for 3D measuring

4.3 System calibration and sample preparation

The first step when the Aramis software is going to be used is always to make a calibration of the system [69]. For that, Gom¹ provides different calibration objects (panels and crosses). The choice of the calibration object depends on the size of the sample to be measured. Here we found a first difficulty: the air bag is very big, and its large displacements make the volume of the workspace (the volume inside which the measures are made) very big. Thus, with our calibration objects, we were not able to calibrate the system for such a large workspace. However, since the air bag is circular, and it is supposed to be axisymmetric, we decided to measure only a portion of it.

The most appropriate would have been using a calibration cross, but the cameras were not the ones provided by Gom with the Aramis system, but by Photron, and it appeared to be impossible to calibrate the system with the cross. The reason was that the cameras' maximal resolution is 1 Megapixel, and the crosses are quite big; therefore, if we distanced the crosses enough to be entirely in the pictures, the small cameras' resolution did not let the Aramis software to "distinguish" the calibration marks. Thus, we discarded the cross. We calibrated with a calibration panel instead. More precisely, the panel of 135x108 mm, the largest panel we had at the laboratory (see figure 4.4).

The workspace volume resulting is in the same order of magnitude of the panel's indicated dimensions. In order to calibrate the whole workspace we needed for the portion of air bag, we had to displace the panel all over the area that the air bag could "touch"

¹Gom is the manufacturer of the Aramis system

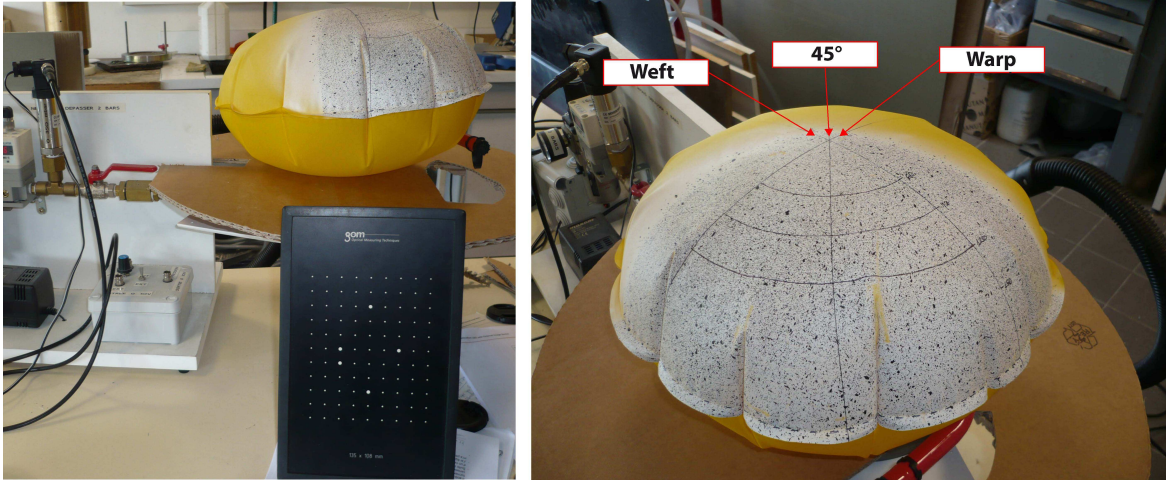


Figure 4.4: Air bag and calibration panel (left) and air bag with the stochastic pattern already made (right)

during the calibration pictures. This could apparently lead to a bad calibration; however, the calibration results were valid: a deviation of 0.027 pixels, while 0.04 pixels is the maximum acceptable deviation for a correct measuring [69].

Concerning the selection of the portion to be measured, we took into account the microstructure of the sample's material (fabric). Fabric is made of a continuous length of interlocked yarns. There are two perpendicular directions along which fibers are disposed: warp and weft (see figure 4.5). The warp is the set of lengthwise yarns that are held in tension on a frame or loom. The yarn that is inserted over-and-under the warp threads is called the weft, woof, or filler [80]. Usually, the warp yarns are more tense than the weft yarns, and as a consequence, the behavior of the fabric is not isotropic, but orthotropic.

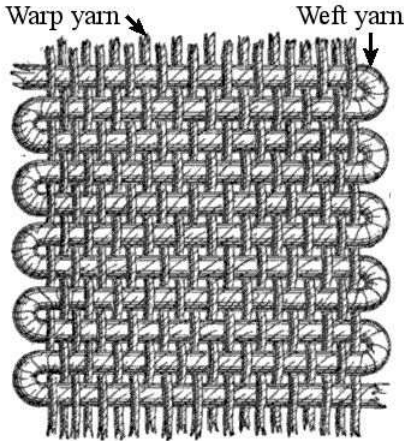


Figure 4.5: Fabric yarns' senses: warp and weft [Image source: en.wikipedia.org]

Since different behavior was expected in the warp and the weft senses, we applied the stochastic pattern to a portion superior to 90° , that included the warp yarn and the weft yarn passing by the center of the air bag (determined by the manufacturer and marked in the air bag). Thus, in the image processing we would be able to analyze the behavior in both senses, and also at 45° .

4.4 Limitations and objectives of the experimentation

This experimentation presented several difficulties that limited the possible exploitable results:

- The only anchor point of the airbag was the tube placed in the center of its bottom. This implies that during the inflation, the air bag can oscillate randomly in any direction, with larger oscillations during the beginning of the inflation, where there is no stiffness at all. These oscillations complicate the measurement of the displacements, and they cannot be calculated with precision. This was the biggest problem of the experimentation. No other anchor points could be made in order to avoid limiting the displacements (without conceiving a new support for the air bag): the diameter decreases during the inflation, and both layers of fabric move away of each other. This makes that the only exploitable result was the curvature of the air bag during the inflation.
- The large displacements of the air bag made it difficult to define the workspace volume. The air bag could eventually exit the volume during part of the inflation if a big oscillation was produced.
- Wrinkles appear during the inflation. Therefore, part of the stochastic pattern "hides" at the end, what originates blanks in the treated data (in the figure 4.6, they can be observed the surfaces "readable" by Aramis at the beginning, in the flat position, and at the end, in the inflated position and with wrinkles).
- The big size of the air bag added to the low resolution of the cameras, made it impossible to measure with precision other than the global displacements.
- Finally, the initial position of the air bag was no completely flat, due to the lack of stiffness of the fabric. The problem with this if we try to measure the global displacements, is how to define the origin of coordinates, to mark the zero position. The solution was to calculate the average plan of the surface at the initial stage with the Aramis software, and use it as the reference plane. We placed the origin in the center of the air bag. The average plan and the origin can be seen in the figure 4.7.

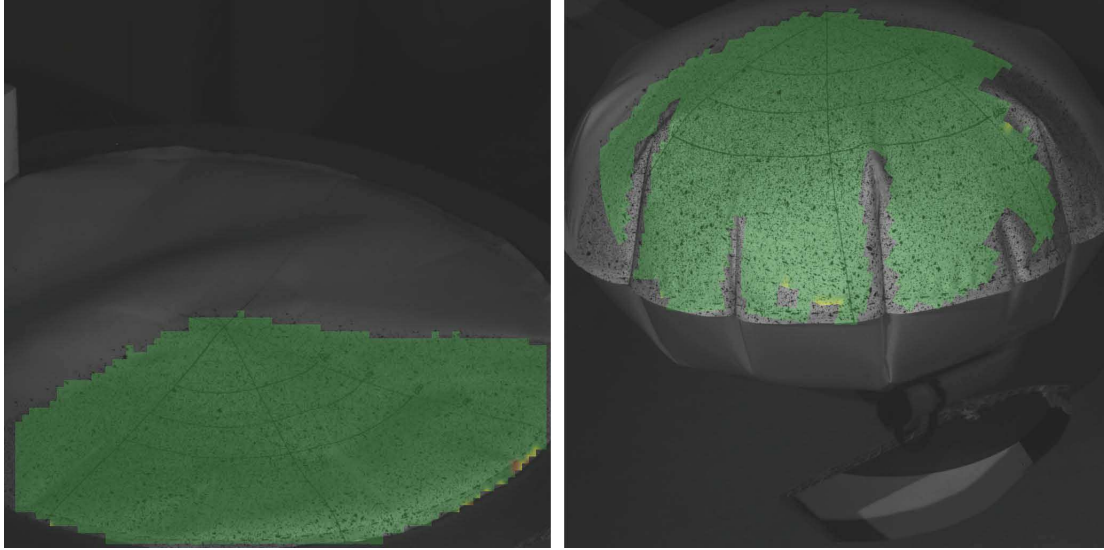


Figure 4.6: Areas that can be processed by Aramis in the flat and in the inflated position

Due to all these constraints, we were conscious that the only exploitable results were to obtain the global displacement of a portion of the superior fabric layer. This data could be compared with the results of numerical simulations.

4.5 Numerical simulation

Since the only result we can exploit are the global displacements, a simulation was made to obtain the displacement field. This numerical simulation was carried out in Herezh++ with the following parameters:

- The material properties were the provided by the fabric manufacturer: $E = 125$ MPa, $\nu=0.41$, thickness = 0.27 mm, density = 900 kg/m^3
- The calculation algorithm was dynamic relaxation with kinetic damping in the same conditions as shown in the previous chapters.
- The element type used were shell elements. Even if in the research works of this thesis we used membrane elements, here we looked for a more realistic result by taking into account the flexion of the elements, particularly effective to obtain realistic wrinkles (see work of Onate [126]). For that, we used the shell elements implemented in Herezh++: SFE (Semi Finite Element), that are introduced in the thesis of H. Laurent [71] (a review in english can be read in the paper [72]).
- Due to the existence of a symmetry, only the superior fabric layer was calculated. The mesh had 111 192 dof, in order to obtain a realistic result.
- The load applied was a pressure of 0.02 MPa, applied following a slope during 1 second (this is the global time, serving for the advancement of the loading).

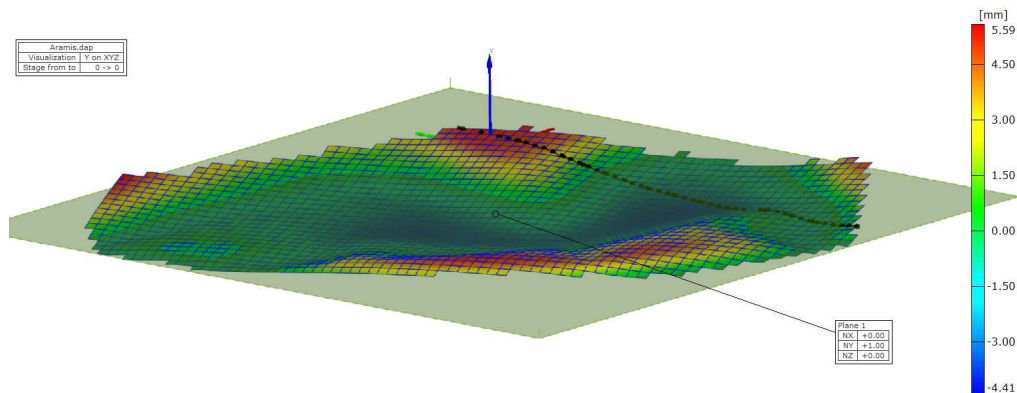


Figure 4.7: Reference plan calculated with Aramis as the average position of all the surfaces' points.

The result of simulation can be seen in the figure 4.8. There, we observe that the maximum vertical displacement is 96.4 mm.

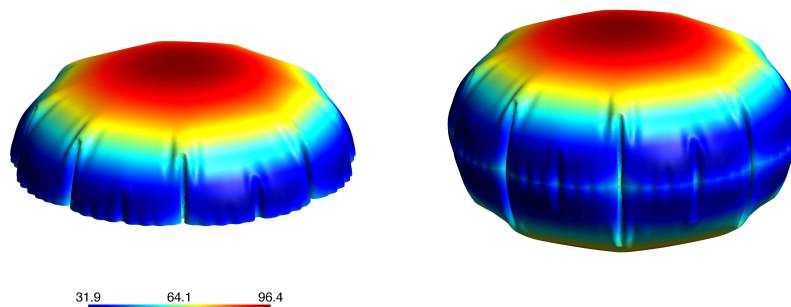


Figure 4.8: Field of displacement of the air bag; simulation result (left) and full air bag representation (right)

A priori, the results seem to be close to reality, since the general shape is similar, and even the wrinkles' distribution is also close to reality. Figure 4.9 shows both simulated and real air bags, putting in evidence the similarities. We can observe the similarities: big wrinkles (A) interspersed by medium-sized wrinkles (B) and small wrinkles (C). Also, we can even observe the same deformation in the fabric at the limits of the big wrinkles (D).

4.6 Measuring results

After treating the data recorded with the cameras in Aramis, the resulting displacements with isolines can be observed in the figure 4.10:

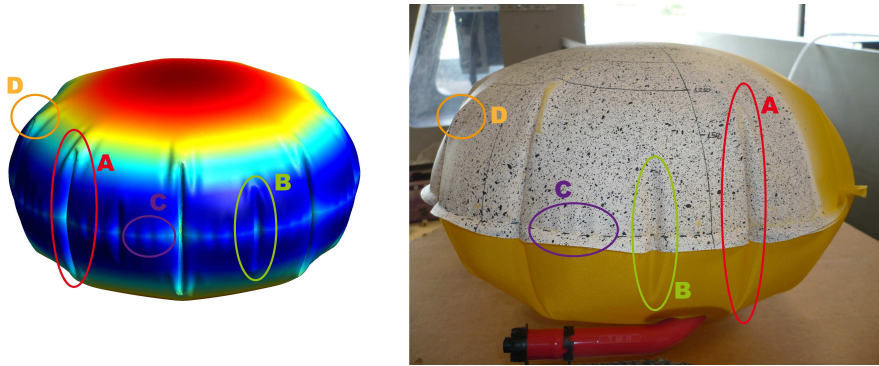


Figure 4.9: Field of displacement of the air bag; simulation result (left) and full air bag representation (right)

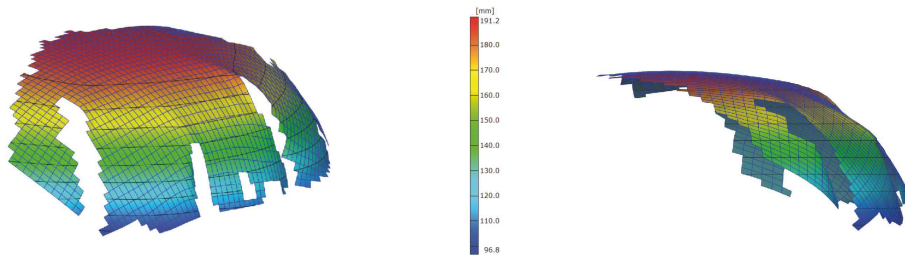


Figure 4.10: Field of displacement of the air bag; two views of the experimental result

In the figure, we can observe that blanks appear where the wrinkles are located. This is impossible to avoid, and it hinders the measurements (for example, we could think of measuring the internal volume of the air bag, but it is not possible with so many blanks). However, we can see that the displacement isolines are coherent and have the same allure than in the numerical simulations (figure 4.8).

Also, we can see that the maximum vertical displacement of the air bag is 191.2 mm. The value we had obtained in the numerical simulations was 96.4 mm for a half of the air bag. Thus, if we consider the full numerical simulation of the air bag, the total maximum displacement is $96.4 \times 2 = 192.8$, a value very close to the experimental value of 191.2.

As we explained at the beginning, we considered three directions to be studied: warp, weft and 45° . These senses were manually marked in the air bag to be able to identify them during the post-processing of the images. Thus, we cut with a vertical plane along each one of the senses, and they can be seen in the image 4.11.

Firstly, the blanks avoid to have the full cuts of all the senses. Then, concerning the transient part, we could not be able to compare it analytically with the simulation, due to the random oscillations of the air bag appearing during the inflation. This problem is visible when we look at the evolution in time of a cut of the measured surface. Some

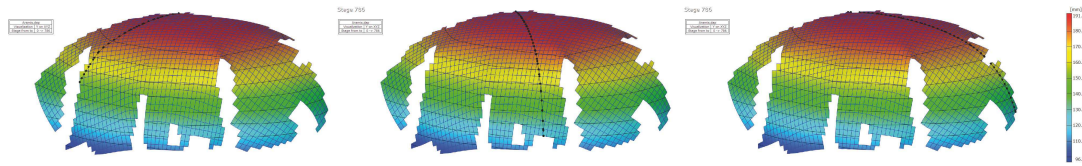


Figure 4.11: Yarns' senses as read in the images from Aramis: Warp (left), weft (right) and 45° (center)

screen captures are showed in the figure 4.12, that shows the evolution of the cut made at 45° (we show this one because it is the one with the least number of blanks). In that sequence, we can see that the air bag does not inflate regularly, but inclined to one side, making it impossible to do a direct comparison with the simulations.

However, we could observe another very interesting phenomenon. During the inflation, the air bag did not inflate regularly: a big wrinkle appears in one side of the air bag and propagates along the radius until a stage where it disappears and the inflation is continued (see figure 4.13).

When we made the numerical simulation of the air bag using membrane elements, the inflation was regular, a regular increase of the vertical displacement occurred in an axisymmetric way. We thought this was somehow logic, because the wrinkle origin could be due to its positioning, heterogeneities in the fabric, etc, and we found it logic that simulations did not predict that. However, when we carried out the numerical simulation using shell elements instead of membrane elements, this phenomenon appeared in the results. It can be observed in the figure 4.14. However, this apparition of the wrinkle in the simulation is still unstable and can be probably due to the irregularities in the mesh.

4.7 Conclusions

The multiple encountered difficulties (lack of an appropriate support that avoided oscillations, the blanks due to the wrinkles, etc) limited the exploitable results of the 3D measuring experiments. However, some good results were found (mainly, the almost equivalent vertical displacement, the similarities of both numerically simulated and measured air bag, the similarities during the inflation). With these results we could not validate the numerical simulations (including the transient part) but we could say the results are coherent with what happens in reality.

For a better validation, a support should be conceived to properly anchor the air bag. If this was done, probably the results would be exploitable.

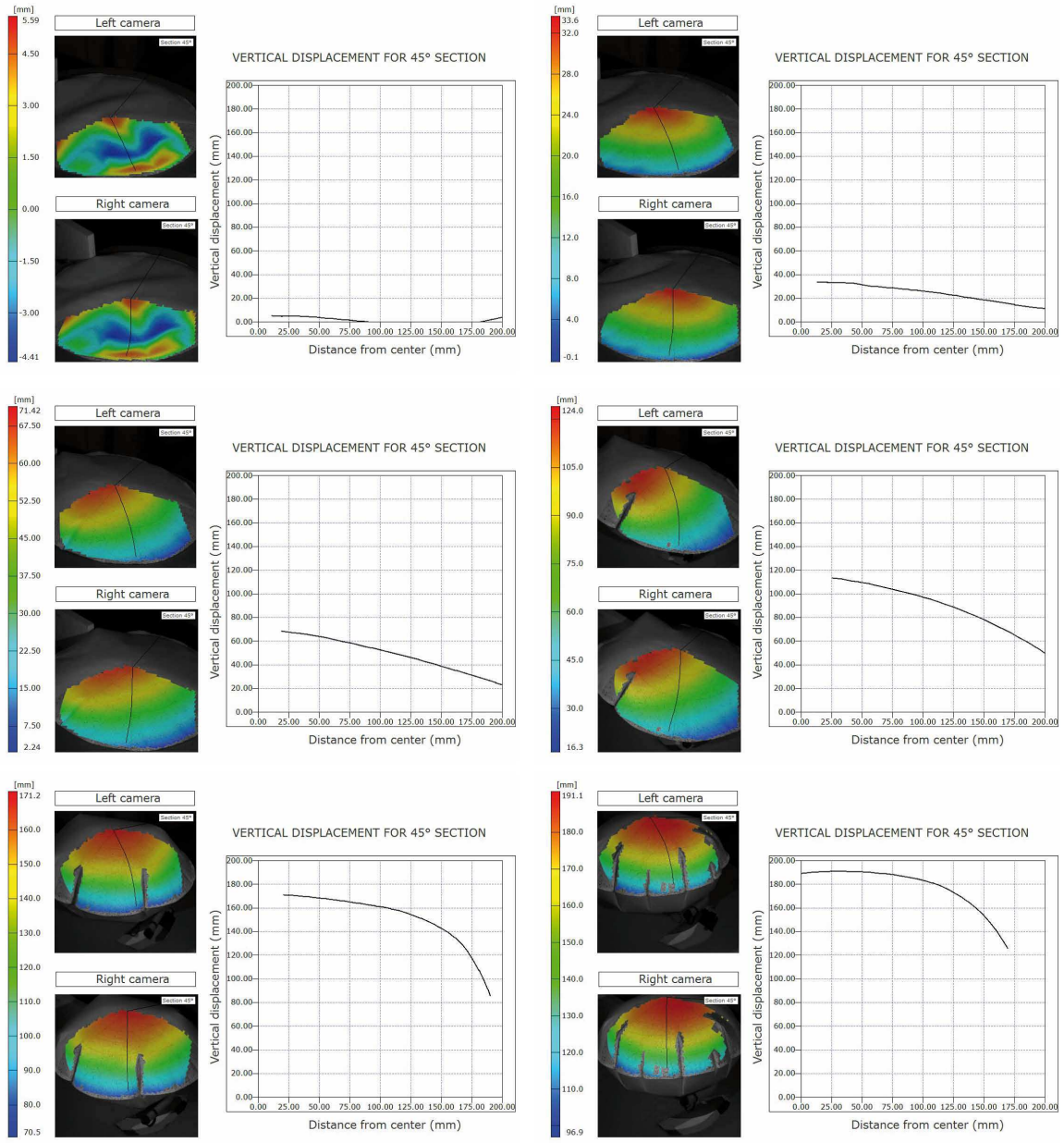


Figure 4.12: Captures of the air bag inflation sequence, showing the evolution of a cut at 45° (from the warp or weft sense)



Figure 4.13: Captures of the air bag inflation sequence, where the apparition of a big wrinkle can be observed

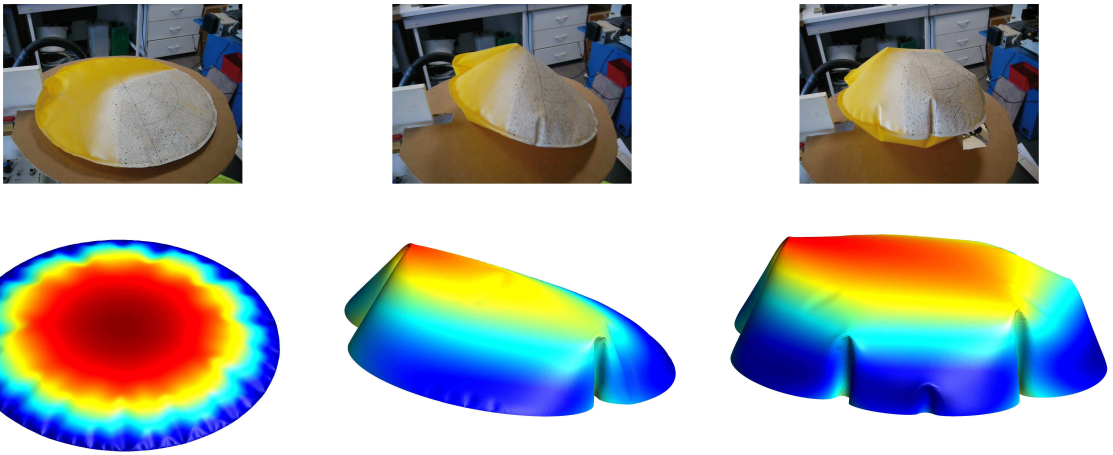


Figure 4.14: Captures of the air bag inflation sequence, where the apparition of a large wrinkle can be observed

Chapter 5

Tensile tests on fabric

5.1 Introduction

The secondary objective of this thesis work is to make a contribution to the modeling of inflatable lifejackets. This modeling would suppose being able to make a simulation that could eventually reduce the amount of real functioning tests (carried out with a physical mannequin and a lifejacket's prototype in a pool).

Concerning the inflation simulation of the lifejacket, in order to obtain realistic and reliable results, the material properties need to be properly defined. The studied lifejackets are made of a technic textile called TEXTANE A/B 210 (240g) XF. The lifejacket's manufacturer provided the following information about the technic textile:

- Young's modulus: 125 MPa
- Poisson's ratio: 0.41
- Fabric thickness: 0.27 mm

It might be obvious that these data are not enough to have a good description of the material. With this information, the fabric is supposed to have an isotropic and perfectly elastic behavior. However, this is a woven textile, and that fact suggests that there exists, at least, an orthotropic behavior. Also, since the fabric has a polymer matrix to make it watertight, it probably has a more complex behavior than perfect elasticity. We will assume nevertheless that the thickness is constant all over the fabric, and with the value indicated by the manufacturer.

The objective of this chapter is to observe the real behavior of the material by carrying out different tensile tests.

5.2 Technic textile

The textile manufacturer has provided a data sheet (see Appendix B). Looking at this data sheet, we can observe that this textile is composed of a PU matrix, an adhesive and the woven fabric itself. Thus, the fact of having a polymeric matrix can give it different properties than if it only had fabric.

Also, observing the description of the fabric, we can see that there is a different average "density" of yarns in the warp and weft senses. While in the warp sense there are 27 yarns/cm, in the weft sense there are only 21 yarns/cm. Usually, yarns in warp sense are more tense by default (due to the way of manufacturing of fabric), what gives a higher stiffness in the warp sense than in the weft sense; and if added to this there are more yarns, the difference of stiffness should be even higher, what confirms that the material must be orthotropic.

In order to have a better knowing of the used material, we used a microscope to obtain a micrography (see figure 5.1). There, we could observe the different tension of the yarns depending on the sense (warp yarns seem to be more "straight" than weft ones). The polymeric matrix can also be intuited in the gaps between the yarns. In the most zoomed image, we can see that the yarns are composed of several fibers; there, it seems that there are more fibers composing the weft yarns than the warp yarns, but it can be due to the fact that, being more tense, the warp yarns have some of their fibers superposed. Thus, the cross section of warp yarns would be more round than the cross section of weft yarns.

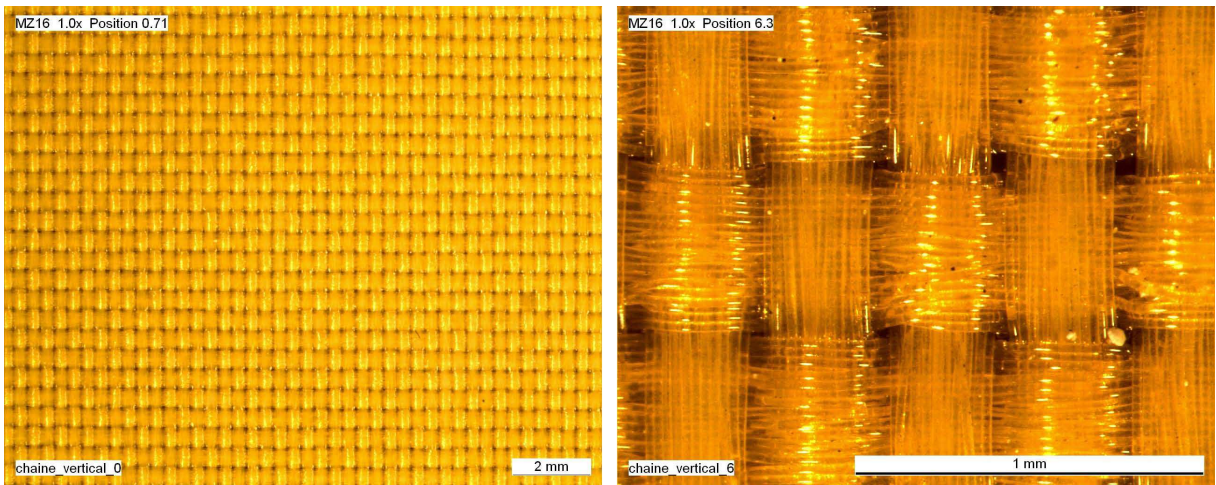


Figure 5.1: Micrography of the studied textile with different zooms (warp sense is in vertical in both images).

Another phenomenon that we will neglect in our numerical simulations but that it is worth to mention, concerns the variation of thickness occurring when stretching the material (due to the crimp). Actually, our calculation software does consider the thickness reduction (as we showed in the Validation chapter), but in this kind of fabric, the opposite phenomenon could eventually occur: an increase of the thickness when it is stretched (see figure 5.2). In our calculations, we will consider the provided thickness as good (0.27mm) and we will consider that it can *only* be reduced when stretching it (implemented in Herezh++). To take the crimp into account, we should model the material at a different scale, what escapes our purposes.

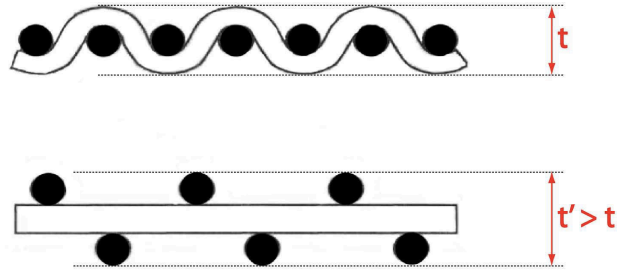


Figure 5.2: Figure showing the phenomenon of thickness increase when stretching

5.3 Tensile test preparation

Tensile strength is the most important property of a fabric. In almost every fabric development and manufacturing, tensile properties are reported. Modulus, breaking strength and elongation at break are widely used for quality control [73]. Among the different types of fabric tensile tests, in this work we carried out the strip tensile tests, where a narrow strip of fabric sample is used.

As suggested in the work of Quaglini [75], we carried out tests not only in the warp and weft senses; also in an "off-axis" direction, in which the specimen was aligned at 45° with respect to the warp direction (see figure 5.3).

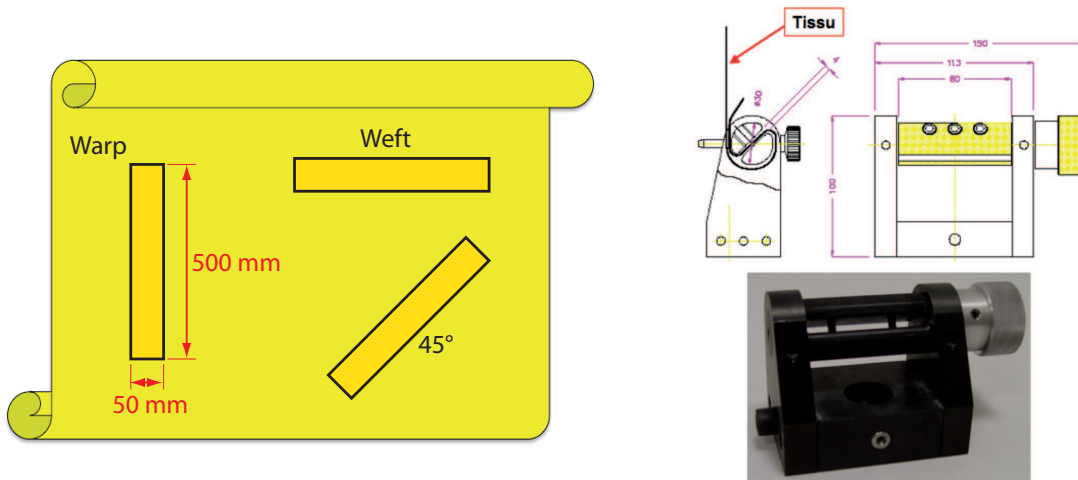


Figure 5.3: Figure showing the different types of samples used in the tensile tests (left) and the jaws used in the tensile test machine (right) (Source [1])

For the determination of the warp sense, we followed the proposition of the "Handbook of Weaving" [73] regarding to our micrography and the data sheet provided by the manufacturer: "If one set of yarns have ply in the fabric, it is usually the warp yarns. Warp yarn needs to be stronger than the filling yarn due to heavy forces acting upon them. In general, the warp density (ends/unit length) is more than the filling density (fillings/unit

length). In the fabric, warp yarns are usually straighter than filling yarns since filling yarns may have more tendency for bow and skewness.”

The samples were cut from a roll of textile provided by Plastimo, following the indications of the norm ISO 1421:1998(F) [76]. This norm indicates that each sample must be 50 mm \pm 0.5 mm width, and a effective length (once the sample is placed in the jaws) of 200 mm \pm 1 mm. Similar indications are provided in the work of Dauda [77].

Therefore, samples were cut with size 500mm \times 50mm so that once they were placed in the rolling jaws (see figure 5.3) the sample dimensions respected the indications.

For the testing, a tensile machine was used along with a 3-spot measuring system (see figure 5.4; an explanation can be read in the works of Thuillier [78] or the thesis of Troufflard [1]).



Figure 5.4: 3-spot local measuring system setup

We carried out different tests: break tests (sharp break [74]), tests with different speeds,

cycles, cycles with relaxation time, etc. Tests were made at deformation speed $\epsilon = 10^{-1}$ and at ambient temperature (20 °C).

5.4 Results

Figures 5.5, 5.7 and 5.8 show the results of the different tests.

We can observe in figure 5.5 (left) the different behavior of the technic textile when being solicited in the different considered directions. At 45° the stiffness is very low and at least at the beginning this stiffness is probably due only to the polymeric matrix. A very large elongation appears when the tensile test is done along this direction (see figure 5.6). Also, we could observe in the plots that the textile behaves as expected in the warp and weft directions (being stiffer in the warp direction). In figure 5.5 (right) we can see the good repeatability of the tests (only one example is shown): there, they are represented 3 tests in the warp direction, and the most significant difference is a small difference on the break elongation.

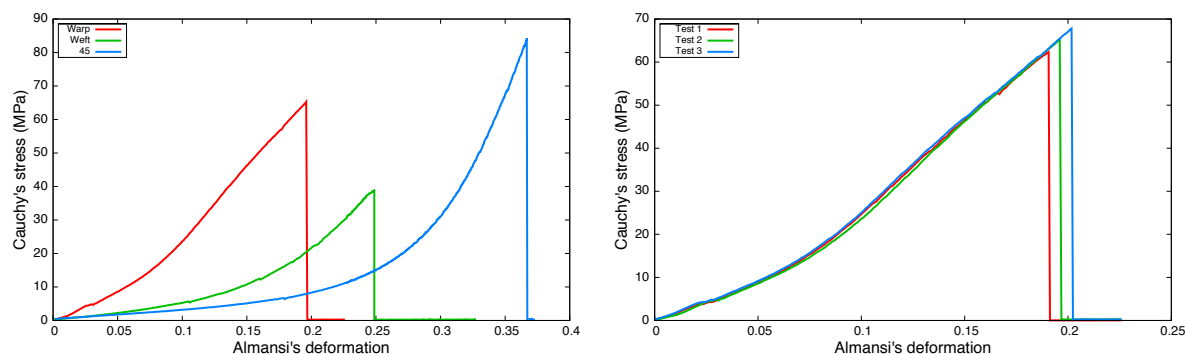


Figure 5.5: Break test with different directions and deformation speed 10^{-1} (left) and repeatability test in warp direction at the same speed (right)

In figure 5.7, two different loop tests are represented (single and multiple loops), where we can appreciate the existence of a certain viscosity.

Finally, in figure 5.8, tests with relaxation times are presented. These tests were carried out in order to have the possibility of an eventual identification of parameters for introducing a complex law of behavior in the calculation software.

5.5 Conclusions and discussion

After the experimental observations, we can conclude several points:

- The technic textile has an anisotropic behavior, as expected. Thus, an implementation of a orthotropic law of behavior could be convenient to be closer to the real behavior.

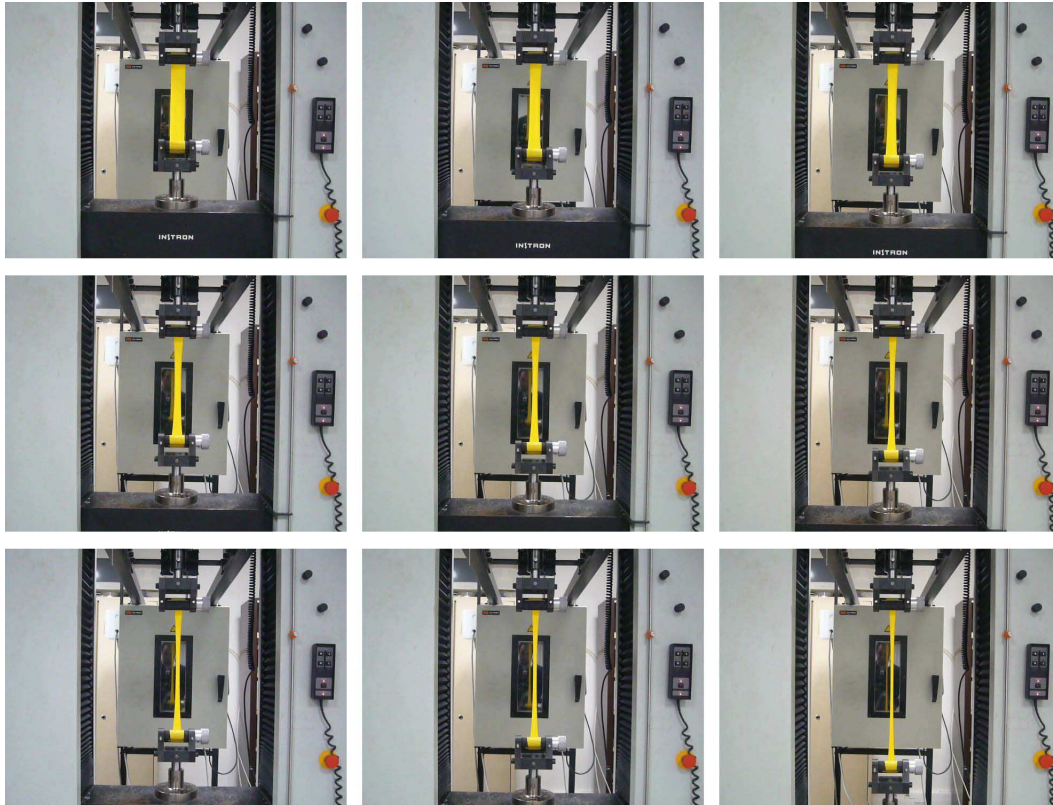


Figure 5.6: Test in the off-axis sense (45°)

- We could observe hyperelasticity and viscosity. However, in the common usage of this textile in lifejackets, stresses and then deformations are not very high (peaks of stress are in the order of 15 MPa), so the fact of considering hyperelasticity is probably not very important. We could say the same about viscosity taking also into account that the inflation of the lifejacket is relatively slow (in around 1 second). But although the inflation phase is slow, the objective is to have final form after a time quite long (typically several minutes), so a priori, after the relaxation of viscosity.
- The observed hysteretic behavior could be important or not: if we consider that the lifejackets are not supposed to inflate and deflate often (only when an emergency occurs), we could neglect it. However, if the manufacturer makes periodic tests on them (each year, for example), after a certain number of inflations/deflations, the hysteresis could end being important.

All these points are only hypothesis, since there could be many other parameters influencing the real behavior of the technic textile in a common usage, for example, the temperature: water's temperature in the ocean is in a range from 0 to 38 °C, and the sun can also act. High temperatures can lead to higher deformations and probably hypere-

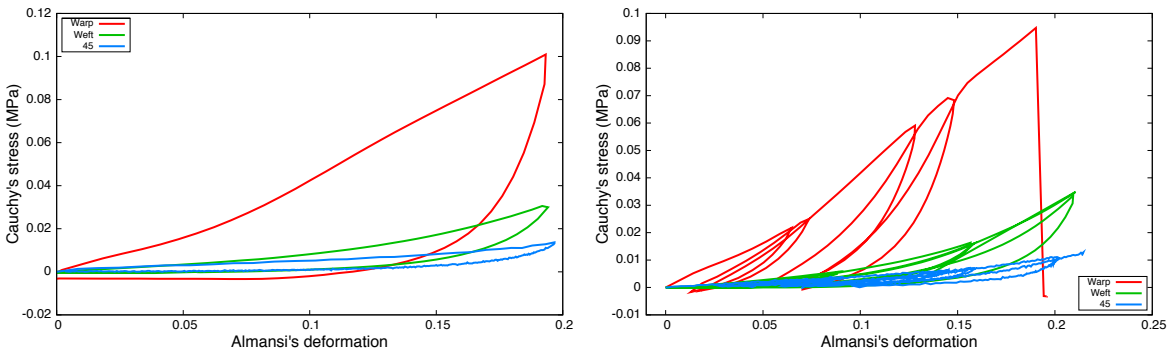


Figure 5.7: Loop tests for the different directions (left) and several loops tests (right)

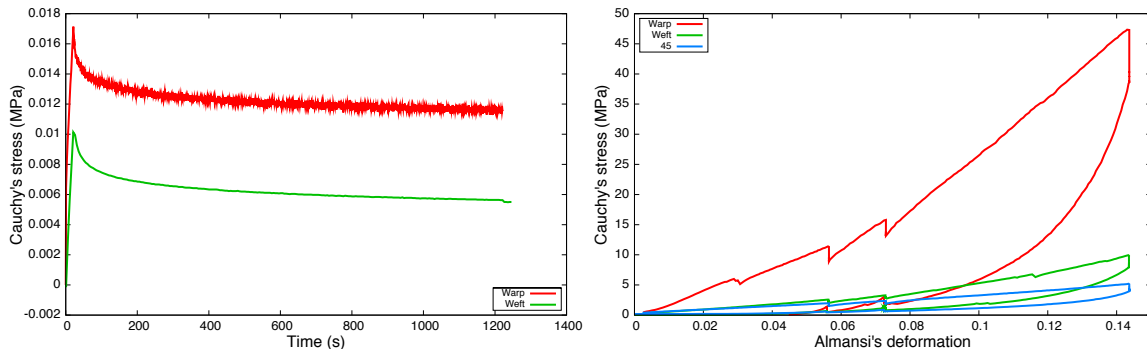


Figure 5.8: Tests to determine τ (left) and loops with relaxations for the different directions (right)

lasticity becomes important. Also, stresses can be different if the lifejacket is worn by a man or a woman, for example.

Therefore, we can finally conclude that considering only an elastic behavior can be not enough to describe the technic textile's behavior under real usage conditions. It could be interesting to introduce a more complex law of behavior including orthotropy, hyperelasticity and hysteresis. However, if the aim is to have a base for comparing the different lifejackets' conceptions, this could be enough.

Chapter 6

Human body model

6.1 Introduction

The objective in this section is to create a generic dummy, i.e., a human-shaped FE model which would permit to carry out the different desired simulations porting the lifejacket. Also, the model must allow to be able to easily modify its morphology in order to be able to obtain an approximation to any kind of human body shape (man or woman, any height and weight, etc). Another important requirement is simplicity: it must be a FE model with a small number of elements, because calculations must be relatively fast.

Previous works were made at the LIMATB (*Laboratoire d'Ingénierie des MATériaux de Bretagne*) with this subject. The first one was carried out by the student of IUP of Lorient, Quentin Govignon, who created a very simple model with squared shapes. Later on, Julien Troufflard [79] made a training work improving the dummy model, and obtaining a model closer to reality. On this last work of Troufflard is inspired the present work for the creation of the new and improved model.

In the literature, several human body models can be found, but no one match exactly the present requirements of simplicity. Most of the works using a human body model use it either for studying its kinematics and animation (mainly for virtual reality) or the behavior of a precise body part (taking into account all the bones and muscles, and even the internal organs). Some examples of human body modeling can be cited:

- **Works focused in the kinematics or animation:** For example, Multon [84] focused on the motion of human body, studying the musculoskeletal system (locomotor system), as well as Nedel [85] did. Porcher Nedel [86] and Park [92] also modeled the human body in order to make animations for virtual reality simulations. Another example of human body modeling to study kinematics is the work of Oliver [87]. Savenko [94] worked on an articulated figure for use in animation, and Maciel [96] presented a model to represent joints in articulated bodies. Kayis [105] presented a model with joints to integrate in simulations of environment design with CATIA.
- **Works focused in human body parts:** Erdmann [88], for example, studied the

trunk; Veeger [89] studied the upper extremities, taking also into consideration the muscles; Zordan [90] studied the environmental interaction of the upper-body; Willinger [91] focused on the human head, including the brain; and Perez del Palomar [99] studied, for example, the women’s breast deformation for pre-surgical planning. Other kind of application is the work of Gourret [106], who studied the contact deformations of human skin (studying particularly a finger’s model).

- Precise models of human body:** In the group of works where the aim is to obtain a human body model as precise as possible, several examples could be cited: Dekker [93], for example, presents some techniques to digitalize the surface of a human body in order to obtain a precise result; Allen [97] also presents the way to obtain a precise human body model (see figure 6.1, right); Choi [98] works in clothing simulation, where the body shape must be precise, but the study is focused in the textile. Another field where precision is important is crash tests simulations: Oshita [100], for example, presents studies involving the response of the human body under impact loading conditions, and in his human body model he includes the skeleton and even internal organs (see figure 6.1, left). Also, other precise models can be found in the works of Delotte [104], who studied the crash test of a pregnant woman, and Haug [107], who also studied cash and impact simulations. Also in the field of crash simulations, Watanabe [103] proposed a human model, including the skeleton.

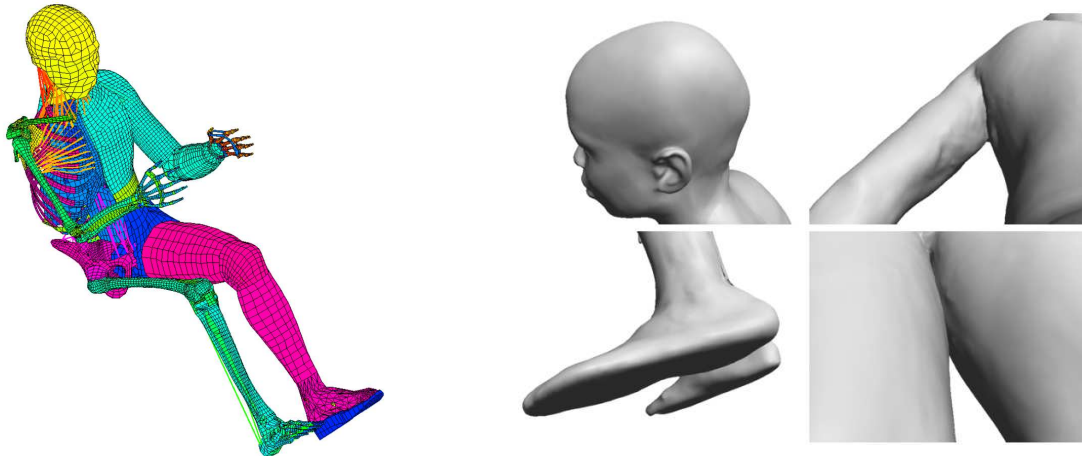


Figure 6.1: Precise human body models presented by Oshita [100] (left) and Allen [97] (right)

Therefore, the fact of not having an exact reference in the literature made it necessary to create a new model under the required conditions.

6.2 Software's choice

To be able to make the calculations with Herezh++, it is necessary to dispose of a Herezh++'s readable mesh file (in format .her). However, another format of mesh could be generated and then converted to a .her file. In the LIMATB there are several available 3D modeling and meshing softwares that could be "combined" with Herezh++, such as Catia, Gmsh, Castem or Gid.

Using Catia might seem the most sensible choice for the modeling, because it is widely used in the industry for the modeling of very complex mechanical parts and structures, and it is probably the one that offers the greatest potential to obtain a realistic result. However, the aim of Plastimo is to dispose of a simple and economic tool to make the simulations. If Catia was used, Plastimo should dispose of some license, being those rather expensive. The same could be told about Gid. However, Gmsh is a GPL (General Public License) software that offered the needed requirements.

The software used by Troufflard [79] was Castem. But since both Castem and Gmsh offered the same parameterization capabilities, Gmsh was chosen due to some advantages: its use is very simple and easy, visualization and post-processing modules seemed to offer more customization possibilities and were more "user-friendly", which is an advantage for the enterprise. Also, the mesh's conversion to a Herezh++ format is easy and precise by using the Perl program "msh2her.pl" developed by Gérard Rio.

6.3 Geometric considerations

For the dummy to have an industrial applicability, it must allow to vary parameters in order to create any desired morphology, and the calculation time should be short enough offering a reasonably realistic result (this implies a compromise between precision and a not too large number of finite elements).

A human body presents rounded forms, which are complex to model. Taking the idea from Troufflard's work [79], the human body can be modeled progressively from feet to head (or vice-versa) by means of an ellipse. If any cut is made in a human body (parallel to the *transverse plane*, see Figure 6.2), the section can be approximated by an ellipse. By placing different ellipses (with different dimensions) at different heights (as if transverse plane was progressively displaced along its normal direction) the body model can be created.

Controlling the sizes of the ellipses would allow to virtually give any shape to the human body model. To parameterize the dimensions of the ellipses, four different parameters were considered. To place the ellipses in a reference system, one of its axis was placed along the x-axis, and the other one along the y-axis. Then, the different ellipses were placed at different heights along the z-axis. Ellipses' centers were placed in the intersection of sagittal plane and coronal plane (see Figure 6.2).

Four parameters were required for a full parameterization: a semi-axis length from the coronal plane (b1), a semi-axis length from the coronal plane in the negative sense (b2),

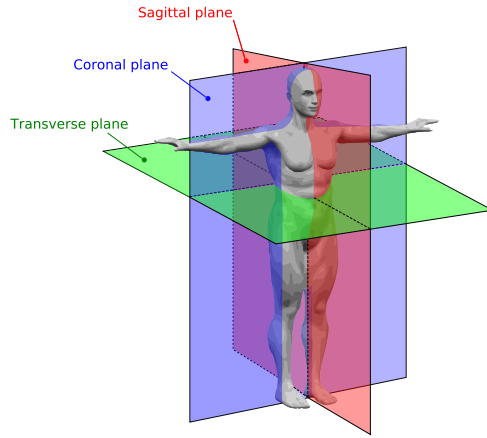


Figure 6.2: Human anatomy planes [80]

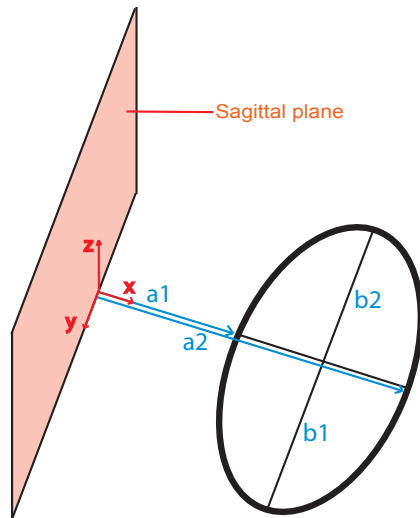


Figure 6.3: Ellipse parameters

the shortest distance from the sagittal plane to the ellipse (a_1), and the longest distance from the sagittal plane to the ellipse (a_2). Figure 6.3 represents these parameters. If we consider the ellipse in figure 6.3 as if it was a footprint (the first created ellipse of the body, the lowest one), we can observe that (b_1) and (b_2) would allow to model the bulges of the body (forward and backward, respectively); (a_2) would allow to control the width of the body sections (being the most external part), and (a_1) would allow to generate legs and arms, that are not "in contact" with the sagittal plane, but at a certain distance (a_1) from it.

Once the parameters were decided, the next step was to start the creation of ellipses by means of an ensemble of perimetric points. Since the objective was to obtain an industrially usable model, i.e., a model which would not take too much time to calculate, perfectly smooth and rounded shapes are not possible. The greater the precision, the

longer the calculation time. Thus, it has been decided to create the ellipses with a contour of not more than 12 or 15 points -nodes-, which would give a facetized result, but with an acceptable precision.

Since the body was going to be parameterized, virtually any dimensions could be used in its creation. The final size could be adjusted at the last stage of the creation procedure.

6.4 Development in Gmsh

The final model was not developed in Gmsh, but by means of a C++ program that generated a mesh in a Gmsh-readable format (.msh). However, it was considered worthy to comment in this section the experience and remarks observed when we tried to generate the mesh directly in Gmsh.

Gmsh [81] is a software which permitted the model (the mesh) creation by three different ways (at its 2.3.0 release). The first, and probably the easiest one was by using its graphical interface. The problem is that this way does not allow to parameterize, and the result would be a dummy with a given morphology (the chosen one when created) and without any chance to easily change it, so a full reconstruction would be necessary to obtain different body shapes.

Another possibility was to create the geometry by coding a .geo file, and after this, by means of the graphical interface, using the automatic Gmsh's meshing module to obtain the desired dummy's mesh (a .msh file) to use in calculations with Herezh++ (after converting it to .her format). This way seemed to be a priori a good idea. Even though it was more complex than using the graphical interface directly, this way did let to parameterize. The existing Gmsh .geo tutorials, showed that a scripting language could be used to create the dummy geometry, and thanks to this it was possible to employ small functions to automatize the geometry creation and also to introduce geometric parameters. So this was at first the chosen way to carry out the dummy creation.

As mentioned before, the human body could be created just by placing several layers of ellipses. So the idea was, firstly, to be able to create a parameterized ellipse. Then, just by repeating it and changing the axes' length and coordinates progressively, it was possible to create the whole body. The aim was to create just the "envelope" of the body (necessary to calculate later its interactions with the lifejacket and with water). Ellipses were created with twelve points along their perimeters, which gave an acceptable precision, and this way calculations should not take too long.

The creation of this .geo file was not as intuitive as expected, because it was necessary to define points, with these, lines, then surfaces and finally volumes. The problem was that it was strictly necessary to respect the order of definition of all instances (the nodes in a line or element, the lines in a surface, etc), being this order sometimes not evident, and a small mistake would give as a result a non-sense mesh (with superposed elements, for example), and there were no indicators pointing to the exact problematic point of the code, so it was necessary to review the whole file and check if all was right. Several tries were needed and it took a lot of time to create something valid.

Beginning from a foot, part of a leg was created, and at this point it was a good idea to check if the created mesh was satisfactory. But again results were not good (see figure 6.4). A "random" mesh was obtained when Gmsh was asked to mesh it. We thought at first that once given the envelope, Gmsh would be able to mesh the interior of the leg with 3D elements. But we found that these elements were superposed ones to others. Probably by spending time on it and with a lot of effort the correct parameters can be used to define a good mesh, but this is not simple a priori.

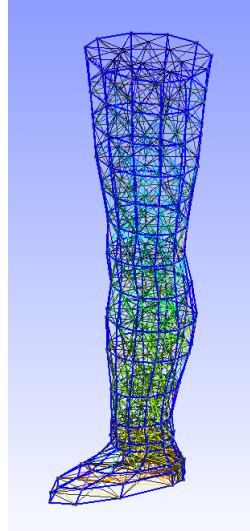


Figure 6.4: Automatic mesh created by Gmsh

So, after these unexpected results, it has been concluded that this was not the correct way to follow, and it has been decided to change the dummy creation procedure and start to work with the a priori most complicated modeling way of Gmsh, but also the only one which offers the total control of the created mesh: an .msh ASCII file.

This way of modeling consists in manually positioning each node (formulae are not used anymore to automatically calculate nodes' positions), and then manually defining each element of the mesh. The result of this is directly the mesh file, and the use of a geometry file (.geo) is not necessary. But the difficulty here was that the whole file consisted in just numbers, and the parameterization in the file was not possible. So, finally, to get this .msh file, it has been decided to create a C++ program which created it. This language had also the advantage that the functions used in the .geo file could be easily adapted to C++, because the code type was quite similar (but of course, C++ offers much more capabilities). The software used for programming was Xcode 2.5 for MAC.

6.5 C++ programming and testing

Being our aim to manually create the mesh (defining all nodes and elements), it could be asked why we didn't create directly a .her file to use in the calculations. The answer is

that, this way, by making a previous .msh file, it could be visualized in Gmsh, and if there was some geometric mistake, it could be easily detected, just by looking at the model in Gmsh's graphical interface. However, if a .her file was directly created, there wouldn't be a way to check that the geometry has been correctly created, and the only indicator of a problem would be an error in the calculation in Herezh++, and since this could be due to several other factors, it was not appropriate to follow this way.

To generate the .msh file, the instructions in Gmsh's website were followed [81], to get to know the .msh file structure. Given that absolutely all elements were going to be manually defined, the first decision to take was the type and number of elements to employ, because this could not be easily changed later. Knowing that the main idea was to create the body with the smallest possible number of elements, it has been decided to use ellipses with just 12 points (nodes). And we have chosen exactly this number because our idea of conception was to use volumetric quadratic hexahedron elements (see Figure 6.5), and this number of nodes fitted to use them.

Hexahedron27:

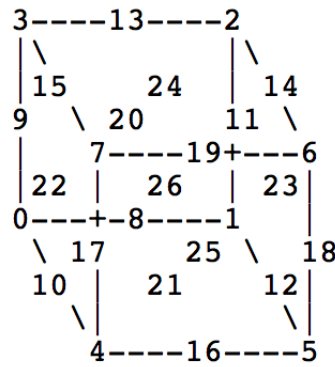


Figure 6.5: Element type hexahedron, 27 nodes [81]

An advantage of this way of coding is also that it is not necessary to define all the lines and all the surfaces to define a volumetric element (as it was required in the .geo file). Here, to make the conversion to .her format, it is just necessary to define the nodes and then, the volumetric elements.

Using this kind of element (6.5), and being the ellipse composed of twelve nodes, two hexahedral quadratic elements need to be placed per layer. Also, even if joints were not being considered yet, a "small prevision" was made. The future idea at this point was to use a "frontal" hexahedron and a "back" hexahedron, and in the case of joints (in those places of the dummy), to define different laws of behavior for traction and compression (different materials) for the two hexahedrons to block or permit the movements in the desired senses. This will be better explained in the corresponding section.

Obviously, using such a small quantity of elements, to give the body a realistic shape the elements could not preserve an hexahedral allure. However, although the elements

were quite distorted in some model's parts, it was checked that the calculation worked anyway (what was not evident a priori). An example can be observed in figure 6.6, where they can be seen the two hexahedral elements corresponding to the right ankle. Notice that the visualization module in Gmsh only shows the facetized surfaces that do not allow to appreciate the quadratic shapes.

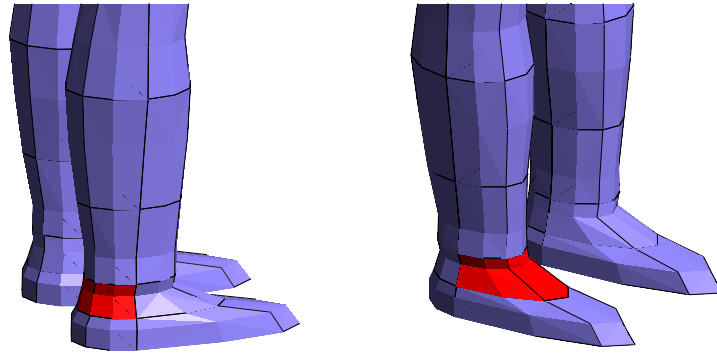


Figure 6.6: Marked in red: hexahedral element corresponding to the rear (left) and frontal (right) parts of the right ankle

The procedure to create the dummy was placing nodes with the desired elliptical shape. To easily create the ellipses, several functions were created in C++ that automatically placed the nodes. After having three consecutive layers of ellipses, it was possible to define a volumetric hexahedral element (in figure 6.5 we can observe that three heights are needed, at least). And repeating this, the dummy could be created adding layers or "slices" composed by couples of two elements (frontal and rear).

To obtain a Gmsh mesh file, an element is defined by indicating: first of all, the type of element (in this case hexahedron 27) and later, after a few other parameters concerning the possibility of creating groups of elements, the nodes that compose the element. The main difficulty in this element definition is to write correctly the nodes which compose it by preserving the correct established order by Gmsh (following the image 6.5 extracted from its website). To ensure that a mistake was not made, it is convenient to check in Gmsh graphical interface right after the addition of a new layer. To be able to visualize the mesh, it was enough to compile the C++ file, and execute the result, and a .msh file was directly obtained.

During the mesh creation, we remarked that as important as defining the nodes in a correct order, was the fact of respecting a certain orientation of the hexahedra.

In the model parts where the extremities ended (basically the trunk, neck and head), four elements per slice were used, to keep a "continuity". At the shoulders, where the arms should start to be created, an auxiliary ellipse was placed at around 45°.

Finished the modeling, and in order to check that the mesh was properly parameterized, a small modification test was made. The result of the test is showed in Figure 6.8, where

three different kinds of morphology were created as an example showing some of the capabilities of the parameterization.

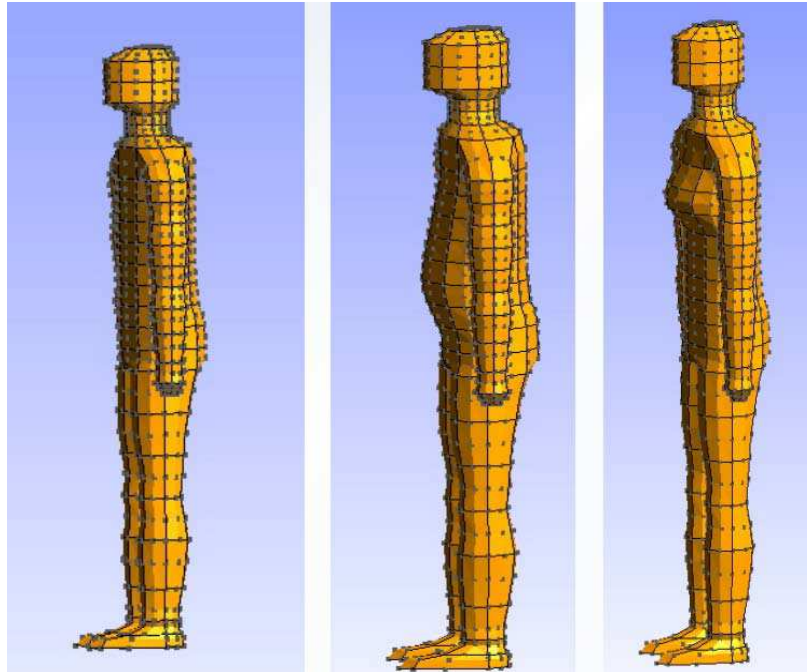


Figure 6.7: (a) Base body shape, (b) fatter body, (c) woman's body

Finally, the obtained model consists in a mesh with only 156 volumetric elements, complying thus with the requirements of parameterization and fast calculation.

6.6 Dummy's design improving

6.6.1 General dimensions

During the creation of the model, no attention was paid to the size of each body member, but to the proportions. Since the created model is parameterized, dimensions can be corrected when needed. The decision of giving the model the shape actually has was only approximative, just looking if it presented a coherent morphology.

For giving it a more realistic shape, further studies should be made. For example, Baca [101] proposed a procedure to determine anthropometric dimensions by image processing. Also, it exists some anthropometric study in the literature, as the one from A.R. Tilley [102], where a very complete information can be found about the sizes of the parts of the human body, depending on the age and gender of the person, statistically calculated.

6.6.2 Joints

Until here, the whole body could be somehow compared with a beam, but with a human allure. However, even if the human to model is supposed to be unconscious and immobile, the joints can allow a certain flexion. However, it is not easy to make a simple model which gives as result the natural movements of human joints.

Looking back to the figure of the three planes in a human body (6.2), they could be defined the different movements:

- **Sagittal plane:** The movements in this plane correspond to flexion/extension. Flexion corresponds to a decrease in the angle between two segments, and vice-versa.
- **Coronal plane:** Movements in this coronal plane are abduction, adduction en radial deviation. The abduction consists in the remoteness from the spine of a segment (and vice-versa for the adduction). The radial deviation movements correspond to wrist flexion towards the interior and exterior.
- **Transverse plane:** The movements in this plane are the internal and external rotations. they correspond to a rotation to the interior or the exterior of the body. For the arms, this movements are called pronation and supination.

Considered solutions

To model the joints, several methods have already been proposed in the works of Troufflard [79]. The more realistic way to model the body would be to define a skeleton inside the dummy. This would allow to have a 3D envelope to calculate external efforts applied to the body that would be related to a second entity which limits the possible movements of the dummy. To restrict the movements Troufflard [79] thought of defining energetic parameters in the joints. He proposed to create just another mesh with 1-D, with just articulated beams. Generally, rotations are defined around a center of rotation, and they are decomposed according to the three planes sagittal, coronal and transverse. In order to calculate these angles, they can be used, for example, the Euler angles. This method is not applied for biomechanics; usually it is applied in other domains such as robotics. The most common problem that could be found in the calculation of angles is the so called "gimbal lock", which occurs when two of the axes of rotation of are driven into the same place, and the joint would loose a dimension of rotation. This loss of information would end in singularities in calculations which would cause problems that could be found later on.

Probably the most simple method would be to decompose the movements vectorially and to calculate the angles between them. It could be fine to constrain directly the movements defining particular relations that should be respected by the degrees of freedom of certain nodes in the joints. The implantation of relationships between degrees of freedom of nodes in Herezh++ is already made, so this could be a good choice. The idea was that each joint is composed by two segments, mobiles one against each other

by a center of rotation; and the movement between them would be governed by means of relations between the degrees of freedom of certain nodes. The angles should stay in an interval depending on the considered joint. The way to respect this interval could be the introduction of energetic terms whose expression depends on the limit angles. Since these energetic terms depend on the degrees of freedom, they would be considered for the calculation of the stiffness matrix.

A first approach to these energetic terms was made by Troufflard [79] but the results were not completely satisfying. The complex studies and time required to carry this out forced us to discard this option. Even though this would probably be the best way, it is not the objective of this work to model a real body with all its real movements, but to model a body which behaves in a realistic way, and it is not necessary for it to be exactly real.

Applied solution

The applied idea was to use a different material (softer) in the areas where joints are supposed to be. During the fall into water, the dummy is considered inert. In this case, the absence of resistance in joints could be modeled by a very flexible material, to permit the body members to displace.

A material behavior would be used to define the physical properties of dummy's body, and another one would be used to define the behavior in the joints. The first point was to choose the material behaviors. For the body, it could be applied a material behavior corresponding to the stiffness properties of a human bone, since they are the most rigid component of the body. This is real concerning the stiffness of the body parts, but the exterior "skin" of the dummy would also have the properties of a bone, which is not very appropriate. However, for what we look for in this work, it can be good enough, because our interest lies in the global behavior, and not the local behavior. Searching in literature, the properties of a human bone were found in a physics book by David Jou [82], and they are the following:

- **Young's modulus** : $E = 16 \text{ GN}/m^2$ in traction, and $9 \text{ GN}/m^2$ in compression
- **Tensile strength** : $200 \text{ MN}/m^2$

And for the material in the joints, properties can be chosen randomly with values, for example, of 1/100 of the bones' properties. Since there was not a reference, the used properties were those that, after calculation, showed a coherent result in the movements of the joints in simulations.

If a deeper study of the joints is made, there are some references for the human joints' possible movements, as the book of Deborah Roche [83], which gives a detailed description and images of all joints' possible movements, also indicating where are the common limits in a normal person. A compilation of the values taken as a reference are shown in the table 6.1. This work doesn't cover a study of the joints, but this can serve as a first reference for a deeper study.

Shoulder extension	Ranges 5-25° less likely to have shoulder injuries
Shoulder flexion/extension	A normal value for flexion is 180° and for ext 45°
Shoulder abduction	For abduction is 180° and for adduction 0°
Shoulder int/ext rotation	90° for internal and 70° for external rotation
Elbow flexion	A normal value is 145°
Elbow extension	A normal value for exbow extension is 0°-10°
Hip flexion	A normal value for hip flexion is 125°
Hip extension	A normal value for extension is 10°
Hip abduction	A normal value for hip abduction is 45°
Hip int/ext rotation	For internal rotation 45° and 45° also for external
Knee flexion	A normal value for knee flexion is 140°
Knee extens/hyperextens	A normal value for knee extension is 0°-10°
Ankle dorsiflex/plantarflex	Normals are 45° and 20° for plantar and dorsiflexion

Table 6.1: Maximum angles in joint movements [83]

To define the emplacement of the joints, since the body mesh was composed of several volumetric elements, and knowing that Herezh++ (among the parameters of its input file) permits to associate a different material to each element independently, the method to assign the materials was just choosing the elements (27 nodes hexahedrons) placed where the joints are supposed to be, as it is shown in the figure 6.8 .

In the image, all the elements that compose dummy’s body are shown (just the external faces are visible). Marked in yellow are the elements that have been assigned a different (softer) material, corresponding to the different joints. As it can be observed in the figure, they have been considered: ankles, knees, hip, shoulders, neck and wrists. Given this configuration, a good material’s choice should give as a result a behavior coherent with reality ¹.

Once the joints were ”placed”, it was necessary to try the new configuration’s behavior. For this, two different calculations have been carried out in Herezh++. The first one corresponding to a dummy without considering the joints, and the second one considering them. The same loading conditions, etc, have been applied, with the aim to compare the behavior of the joints and to check if the new configuration of the joints behaved ”better” than the initial one.

The loads chosen for both files were the same and random, just horizontal forces, and applied as following:

- A horizontal force applied in the right hand, pointing backwards.
- A horizontal force applied in the left hand, pointing forward.
- A horizontal force applied in the right foot, pointing forward.

¹Since we dispose of several integration points, we could also think of a different behavior for each one of them, defining different stiffnesses

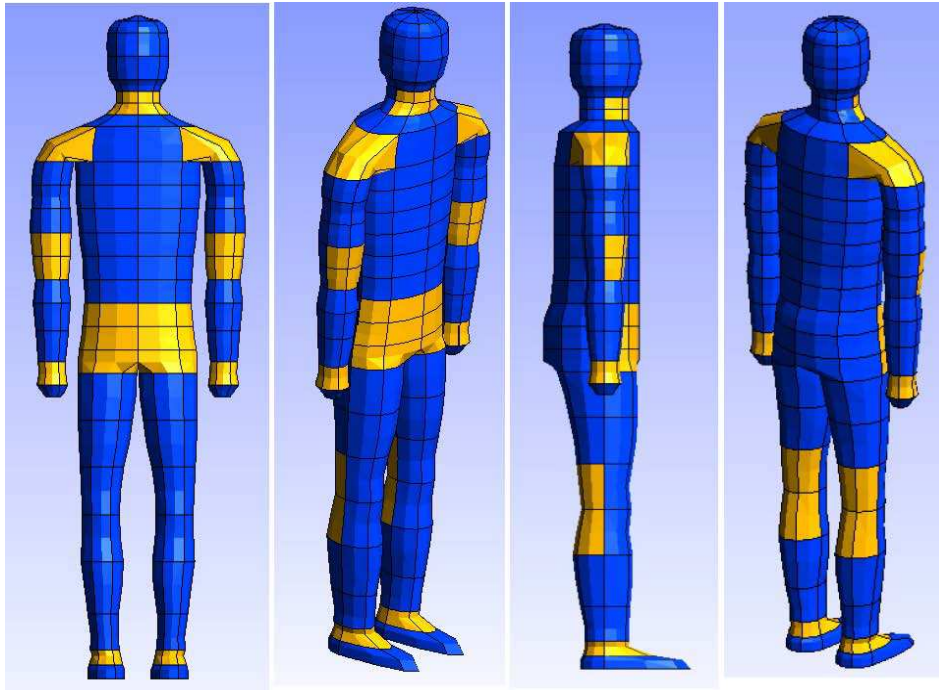


Figure 6.8: Different joint elements in the dummy

- A horizontal force applied in the left foot, pointing backwards.

Since the joints' material is softer, the biggest deformations should occur in the joints. That is what we intended to check. After calculating the simulation in Herezh++, the result could be seen in Gmsh post-processor. In the figure 6.9 they are represented the displacement fields. As it can be observed, displacements are bigger in the case where joints are considered. While displacements were limited by the rigid material in the first case, in the new one, the softer material allowed to move the extremities (as it could happen in reality).

Also, it can be observed a very large deformation in the right ankle, which could lead to some problem in the calculation, but instead the calculation worked out normally. After these results, no more improvements were made in the joints.

6.7 Conclusions and discussion

In this chapter, the procedure of creation of a human body model is presented. The aim was to create a simple model, with a small amount of elements and fully parameterized. The presented model has only 156 volumetric quadratic finite elements with 27 nodes (that can be converted to linear elements with 8 nodes by means of Gmsh, obtaining a simpler model that can be used for faster simulations), and all its dimensions can be modified by means of five parameters introduced in the C++ program that generates the mesh. Therefore, the requirements are fulfilled.

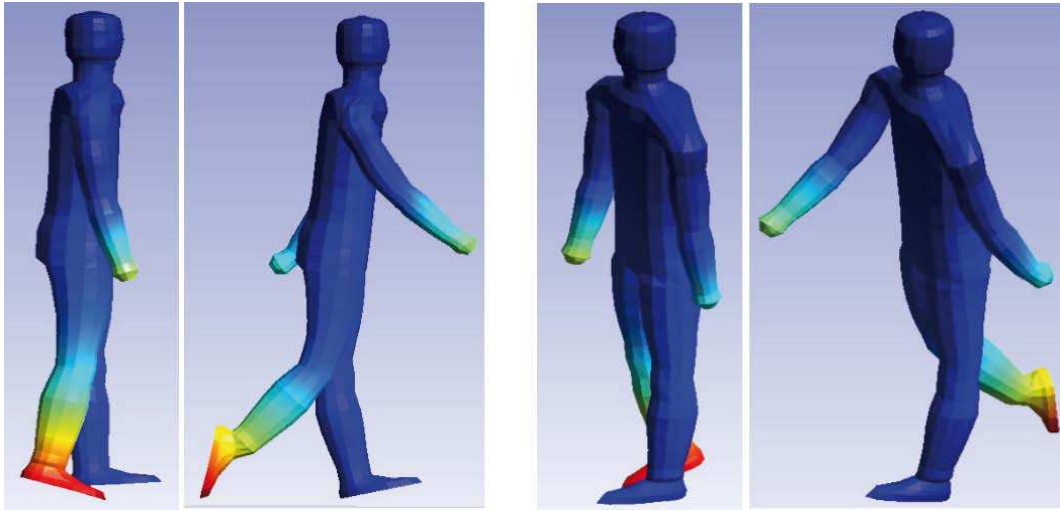


Figure 6.9: Comparison between the model without modifying joints (left images) and the model doing it (right images), in two different views

However, the model could be still improved. Concerning the parameterization, at this stage, the ellipses' dimensions must be modified individually. This allows a perfect control of the final morphology, but it requires a certain time to get to the desired results. Some kind of function could be added that allowed to modify the ellipses' dimensions by body parts, all at once, for example. Another possible improvement concerns the joints, where a deep study of their behavior could be made, but it escaped the aim of this work.

Chapter 7

Lifejacket modeling and contact mechanics

7.1 Introduction

As an industrial application for the dynamic relaxation methods presented along this thesis work, the simulation of the inflation of a commercial lifejacket manufactured by Plastimo is carried out. Previously, we developed the needed tools (dynamic relaxation method, fabric characterization, etc) and now we can apply all this studies to carry out this complex simulation.

The inflation of the lifejacket occurs automatically when the mannequin enters into water. At this moment, a CO_2 gas cylinder discharges the gas inside it, permitting the inflation (see figure 7.1).



Figure 7.1: Lifejackets manufactured by Plastimo, in their folded position and final inflated shape

This is a difficult simulation, because it implies large displacements in a short time (of the order of tenths of second). A good mesh is very important to reach a good speed in the computation convergence. Another difficulty will appear when the lifejacket will be

worn by the mannequin, since contact mechanics is another complicated component of the simulation.

7.2 Creation and meshing of the lifejacket model

Before taking into account the contact mechanics, we will carry out simulations with only the lifejacket. Plastimo’s inflatable lifejackets are usually folded (for a higher comfort for the user), but in this first approach, we will study the unfolded case. Therefore, the simplest design of the lifejacket is just two layers of textile which are welded along their perimeters.

Among the three types manufactured by Plastimo, the one of 150N (buoyancy aid) will be considered in the first approach. The manufacturer provides a certain design for the lifejackets exported from Catia. By means of a script created by Julien Troufflard during his thesis works [1] (consisting in a code in Perl that given the geometry and some parameters, meshes the model), a mesh in Gmsh format is obtained to view the resulting mesh and a mesh in Herezh++ format to carry out the simulation.

The example result of using this code is the showed in the figure 7.2. The design provided by the manufacturer is only the lifejacket’s contour. In the figure, they can be observed two different images, corresponding the left one to a mesh with big-sized elements (showed in order to ease the visibility of the mesh). The second image, corresponds to the mesh used to calculate the inflation, with smaller elements, looking for precision in the results. The mesh used in calculations is a mesh that has 31089 dof.

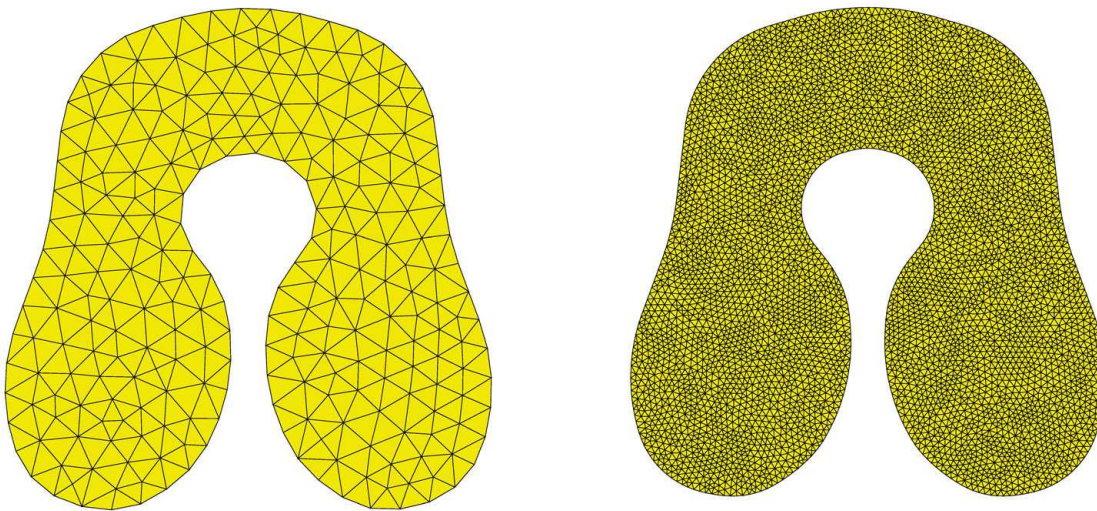


Figure 7.2: Mesh created by the code Perl developed by Julien Troufflard, and visualized in Gmsh. Two mesh sizes, one where elements are clearly visible (left), and the one used in the calculations of this chapter (right)

Even though it is not possible to appreciate it in the figure, both layers of textile are represented, but in the "initial" position, they are supposed to be coincident.

7.3 Numerical simulation of inflation

Once the mesh is ready, the following step is to proceed with the calculation in Herezh++. For this, in an input file, the calculation parameters will be defined.

Among the parameters, we need to define the material properties. In a first stage, the tests will be made with an elastic behavior, following the properties indicated by the manufacturer. The physical properties used in this approach were:

- **Young's modulus** : 125 MPa
- **Poisson's ration** : 0.4
- **Density** : 10^{-9} ton/mm^3
- **Thickness** : 0.27 mm
- **Pressure** : 0.015 MPa

To simulate the CO_2 cartridge's gas, even not being exactly the same behavior, an uniform pressure was applied in the internal faces of the lifejacket. The aim is to obtain the final volume of the lifejacket, what would condition the buoyancy aid, and, finally, its effectiveness. Therefore, we suppose the calculation has finished when the volume is stable.

The result of the simulation can be seen in the figure 7.3 and a comparison with a real lifejacket can be seen in the figure 7.4, where the displacement field is shown. There, it can be seen that the result is very similar, being able even to capture eventual wrinkles all over the lifejacket. For this example, linear triangular **membrane elements** were used. The calculation times are in the order of 5 minutes to obtain this result (mesh with around 30 000 dof; and calculation carried out with one processor in a 2.93 GHz, 16 GB RAM Mac Pro).

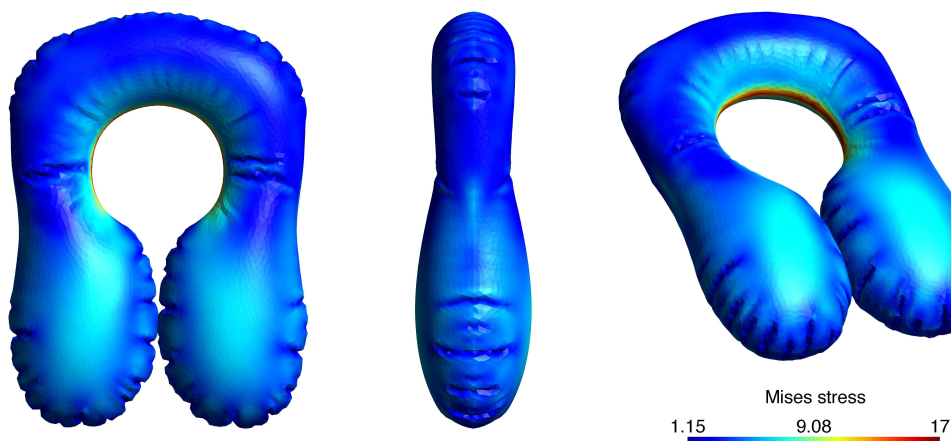


Figure 7.3: Different views of the simulation result (displacement field is shown)



Figure 7.4: Comparison between a real inflated lifejacket (left) and the field of displacement resulting of the simulation (right)

Concerning the volume, that is probably the most important result of a simulation, because it will condition the buoyancy aid, a value of around 20.6 L has been obtained. We can observe in the figure 7.5 a comparison of the volume evolution when using KDR or oDR methods, and also a comparison of kinetic energies on each case. We can observe that the final volume is achieved faster with the KDR method, while the kinetic energy presents much higher peaks; the oDR method appears to be more "progressive" and therefore closer to reality (what we had already remarked in the second paper presented).

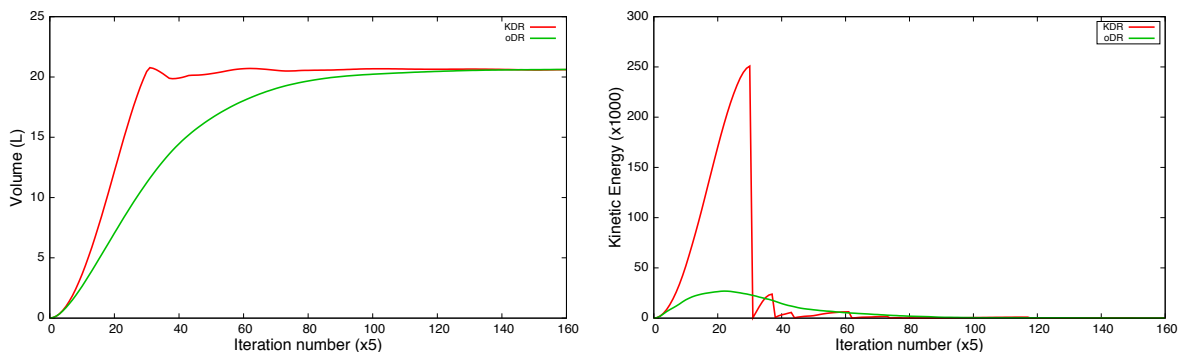


Figure 7.5: Volume (left) and kinetic energy (right) evolution when using KDR or oDR methods

We also wanted to check if there was a difference in the volume when using shell (SFE) instead of membrane elements (taking thus flexion into account). The resulting volume when using SFE elements was 19.71 L, which means a difference of less than 5%. This difference can be due to the different distribution of wrinkles over the lifejacket, being less and bigger in the case of shell elements. This fact is in agreement with the works

presented by Onate on shell elements [126]. We can observe this difference in the wrinkles in the figure 7.6, where a more precise mesh has been used (242 712 dof).

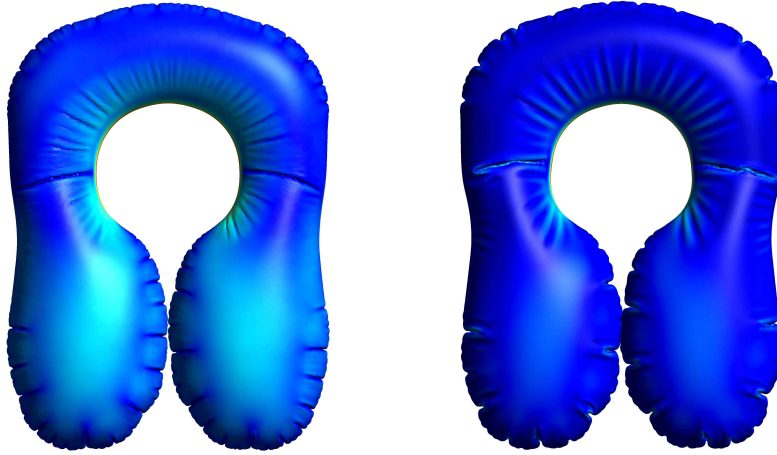


Figure 7.6: Result of inflation when using membrane elements (left) and shell elements (right)

7.4 Contact mechanics

Since the lifejacket will be worn by a mannequin while inflating, here we will include the contact in the calculation. First of all, we will make a brief presentation of the contact mechanics in Herezh++ and the parameters used in our calculations, and then some numerical examples will be shown.

7.4.1 How contact is implemented

The contact method currently implemented in Herezh++ is the penalty method. Its results are similar to Lagrange multipliers but with the advantage of not introducing extra degrees of freedom. A disadvantage is the existence of a small penetration and the need to "calibrate" the penalty parameter.

In the penalty method, the so called "master" and "slave" surfaces are defined, and when entering into contact, a reaction force appears, being this force bigger when the penetration of slave surface into the master surface is also bigger. A penalty parameter is defined, that can be interpreted as a spring stiffness in the contact interface between the master and the slave surfaces [127].

Since the contact mechanics is a very complex problem, different parameters are implemented in order to better control it and also to be able to optimize it. The parameters included in Herezh++ are detailed in the following. Note that only the parameters that are relevant for our calculations are mentioned, but some other are implemented. The

figure 7.7 will be used as a support to illustrate them ¹. There, $\vec{X}(t)$ and $\vec{X}(t + \Delta t)$ represent the position of a node belonging to a slave triangular element at two different time steps and \vec{V} represents the direction and velocity of the slave element approaching to a curved master surface.

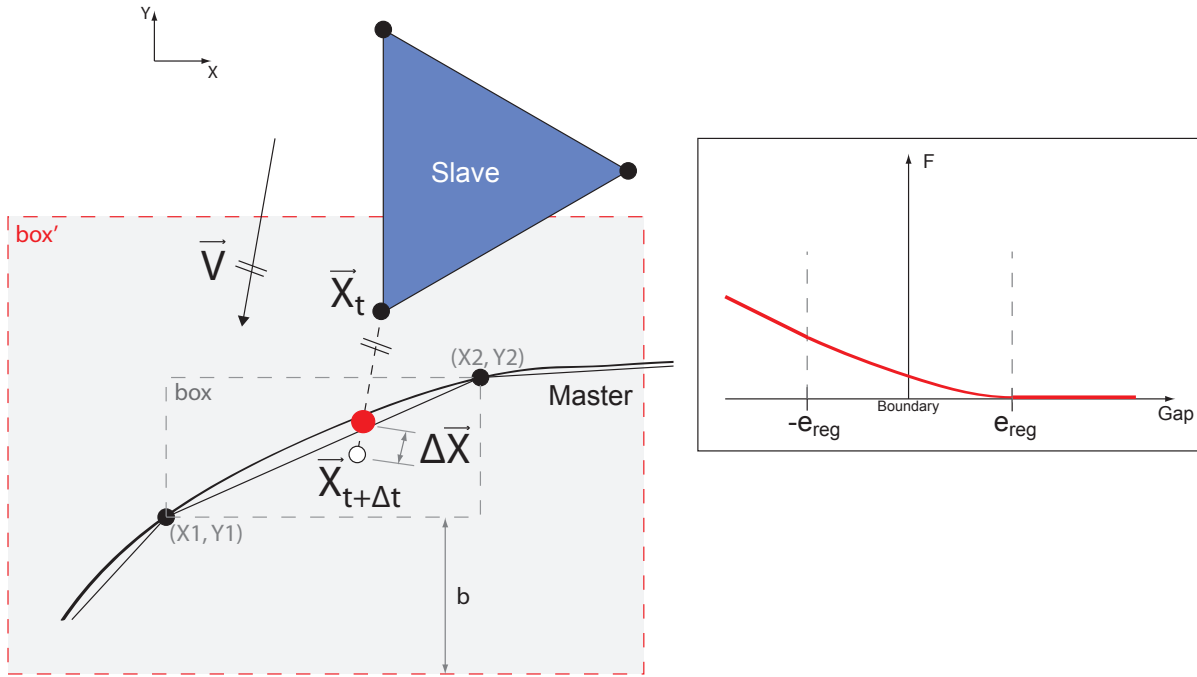


Figure 7.7: Image displaying how the contact mechanics is considered in Herezh++, by representing a 3-node slave element that enters in contact with a curved master surface (left) and the gap-contact force curve (right)

The first step is the search for contact, that is a very time-consuming process. In order to improve it, apart from being able to define the required precision for this process, they can be defined the elements that are susceptible of entering into contact in master and slave surfaces (by means of nodes' references). Another implemented feature is the possibility of defining a "prelocalization box" (*box'* in the figure), that consists in defining an envelope around the master surface inside which is supposed to happen the contact. Outside this envelope, contact is not considered. This envelope is generated as following. Several steps are made in the master surface:

- In a first stage, the limits of each of the elements along each of the reference axis are determined. For example, in the figure 7.7, for the considered master element, the limits are $X_{min} = X1, X_{max} = X2, Y_{min} = Y1, Y_{max} = Y2$. Thus, a first envelope *box* is defined.

¹All kind of elements can be used in a contact problem; in the case of non-flat elements, the real curved shape of the element is used

- Then, since the slave element is moving at a speed \vec{V} , it could happen that it passes through the defined *box* into the master surface and, existing a contact, it is not considered. In order to prevent this, the *box* is oversized. The maximum possible displacement (depending on the speed and the time step) is added in all the directions, obtaining a bigger envelope.
- In order to prevent unexpected problems, another parameter that can be manually chosen is added, obtaining finally a new bigger envelope *box'* (distanced a certain value *b* from the original *box*), inside which the contact will be taken into account.

The idea of this envelope is that no contact will be searched out of it; only if the contacting surfaces (master and slave) are inside the envelope, the contact will be taken into account.

Once the contact has been detected inside the *box'*, the next step is determining the penalty force. In Herezh++, for a penetration $\Delta\vec{X}$ this force is defined as:

$$\vec{F} = -\alpha\beta\Delta\vec{X} \quad (7.1)$$

where $\alpha\beta$ is the penalty parameter, being α an adjusting parameter accessible to the user, $\Delta\vec{X}$ is the penetration, and β is a parameter that depends on the behavior of the contacting bodies (for example, if the stiffness of the master body is higher, so will be this parameter).

Notice that the penetration distance is determined differently than usual in commercial codes. Instead of projecting the slave node in a direction perpendicular to the master surface (the shortest distance), it is projected along the displacement direction (determined by the velocity). Therefore, in the figure 7.7, they are represented the positions of the slave node at a times t and at $t + \Delta t$; and the resulting penetration $\Delta\vec{X}$ will be the used to calculate the penalty force.

The parameter β is calculated as following (the method is the presented by LS-DYNA [28]). There are two different cases: either the slave node impacts a solid element or it impacts a surface element. In the case of impacting the surface A_e of a solid element of volume V_e with a volumetric compressibility modulus K_e , a β_{base} is calculated as:

$$\beta_{base} = \frac{K_e A_e^2}{V_e}$$

In the case of impacting a shell element with a surface A_e with a volumetric compressibility modulus K_e , β_{base} is calculated as:

$$\beta_{base} = \frac{K_e A_e}{\max(\text{distance between nodes})}$$

Since "hard" contact does not happen in the nature, but a smooth contact due to the roughness of the surfaces, a regularized force-displacement curve has been implemented. This curve starts at a certain distance e_{reg} from the exterior of the master surface, and it continues until a distance $-e_{reg}$ inside the master surface (see figure). This feature allows

to have a more progressive evolution of the contact force. Another application for this kind of contact could be the simulation of bodies coated with paint [128]. This curve is defined in the following way from right to left according to the curve in figure 7.7 (right) $-e$ represents the gap between slave and master surfaces-:

- When $e > e_{reg} \rightarrow \beta = 0$
- When $-e_{reg} \leq e \leq e_{reg} \rightarrow \beta = \beta_{base} \frac{(e-e_{reg})^2}{(e_{reg})^2}$, being this way β_{base} multiplied by a value between 0 and 1.
- When $e < -e_{reg} \rightarrow \beta = \beta_{base}$

Finally, a "detachment" of the slave surface from the master surface can eventually happen. This is supposed to happen when one of the following two things occur (one of them can be chosen by means of a parameter m): when the contact force becomes positive, or when the contact force becomes positive and also the distance between master surface and slave node is bigger than $m \times e_{reg}$.

Defined the mean parameters concerned in contact mechanics in Herezh++, we can now define the parameters we used in our calculations where contact has been considered:

- $\alpha = 2$
- $e_{reg} = 3mm$
- Prelocalization box \rightarrow Oversize box of 1.05
- Security value added to obtain the final distance b of $box' = 0.001$
- Detachment $\rightarrow m = 1$

7.4.2 Numerical examples of contact (validation tests)

The contact mechanics has be recently implemented, and in order to validate its correct functioning, several numerical examples of different contact situations were carried out, including the contact between two solids, and between membranes and solids.

First of all, the simplest test made was the contact between two solid hexahedron. For example, in figure 7.8, it can be seen the contact between a fixed big hexahedron and a small hexahedron to which it was applied a vertical descendent displacement, in order to make it enter in contact with the flexible inferior one.

Then, to test the good functioning of contact when working with membrane structures, the classical draping test was carried out (an example of this test can be found in [129]) with a membrane with lifejacket's technic textile material properties see figure 7.9. Notice that self-contact was not considered.

In order to consider the contact in the case of inflatable structures, a first test was made consisting in an squared airbag that finds a rigid obstacle while inflating. This example

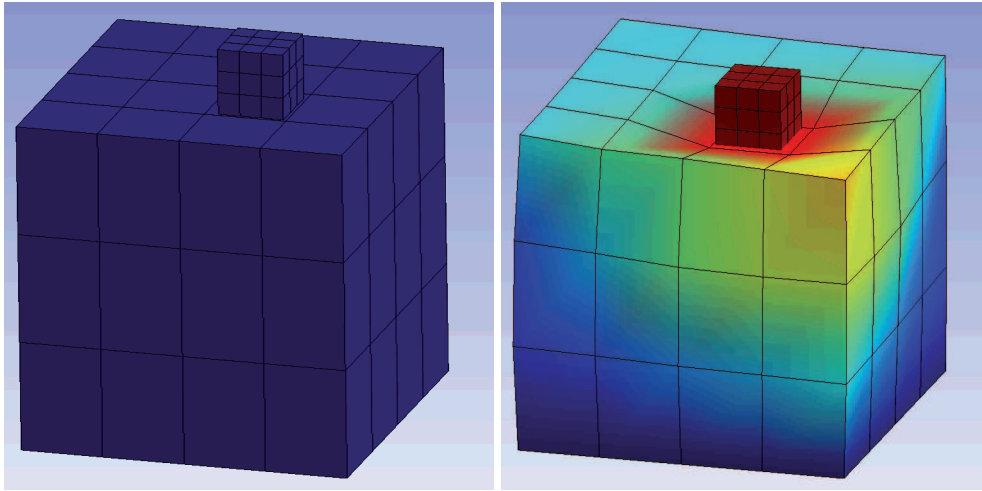


Figure 7.8: Displacement field for a small hexahedron entering in contact with a flexible hexahedron after being applied a vertical displacement

can be observed in figure 7.10. As usual, material properties of the membrane are those of a lifejacket’s technic textile.

Finally, in order to test the contact in the case of the lifejacket’s model, a lifejacket’s mesh was placed over a rigid cylinder, and it was attached by using three attachment elements, with enough stiffness (randomly chosen) to hold the lifejacket when the contact takes place (otherwise, the penalty forces together with the inflating pressure could eject it far from the cylinder). The result can be seen in figure 7.11.

Since all these tests were carried out considering a deformable slave body in contact with a non-deformable body, we tested the same test than the previous one (lifejacket and cylinder) but with a deformable cylinder (with a low stiffness). Thus, we could observe that the implemented contact can also work in the case of contact between two deformable bodies. The result is shown in figure 7.12.

7.4.3 Application to the case of lifejacket and mannequin

After having checked the good functioning of contact in all the showed case studies, a practical application of all the studied concepts (dynamic relaxation applied to the inflation of a lifejacket, human body modeling and contact mechanics), we carried out the inflation of a lifejacket while equipped by the created human body model.

One of the complicated aspects of this simulation is how to attach the lifejacket to the mannequin, but the aim of this chapter is only to prove that all the developed concepts work and can have a practical application; therefore, we attach the lifejacket in some random points (but close to the used in reality) without trying to reproduce exactly the reality. For that, it would be necessary to fold the lifejacket ”arms” and put them attached close to each other, requiring this to consider self-contact.

In order to place the lifejacket on the mannequin, we just leave it fall under the effect

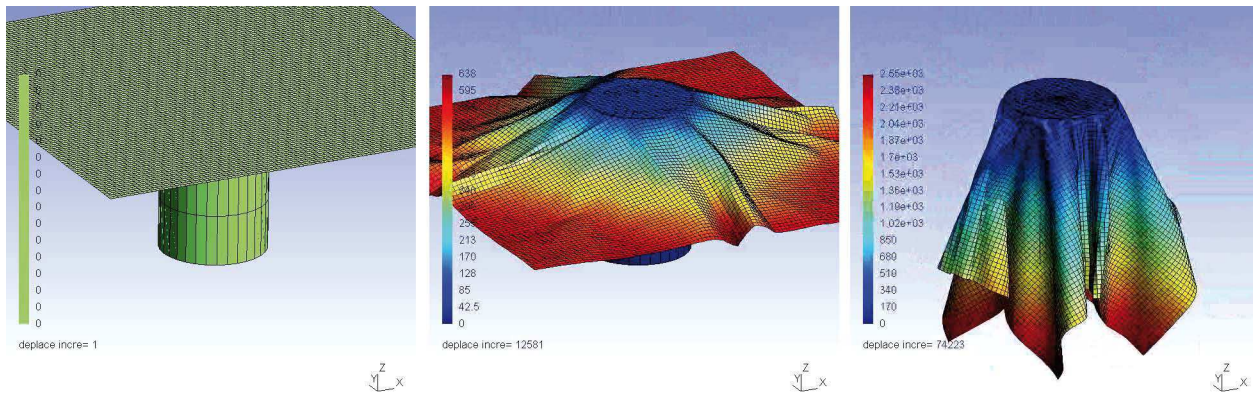


Figure 7.9: Draping test carried out with membrane elements and technic textile’s material properties

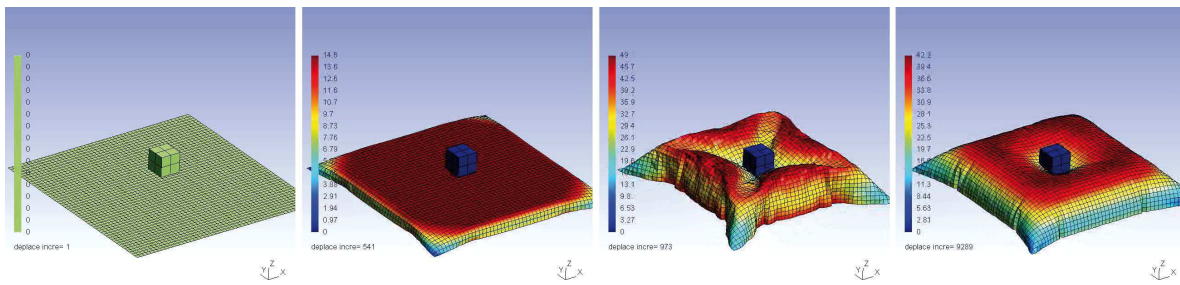


Figure 7.10: Contact test where an inflating air bag encounters a rigid obstacle

of gravity, and once this first stage of calculation has converged and the lifejacket is still on the mannequin; a new calculation stage is done where some anchor points are defined and fixed (so the lifejacket remains attached to the body) and the inflation pressure is applied. As a result, we obtain a simulation of the inflation of the lifejacket being worn by the mannequin. The different stages of this simulation can be seen in the figure 7.13.

A very interesting feature of this simulation is that it can allow to obtain, for example, the stresses in the attachments and specially the reaction forces acting on the head of the person, what can be a very important conception factor.

We can see the final state of the inflated lifejacket in the image 7.14; and if we set the same scale for the Mises stress that we had previously had set for the simulation of only the inflation of the lifejacket (figure 7.15), we can observe that the solicitations are quite different within usage conditions compared to those obtained without considering the mannequin porting it.

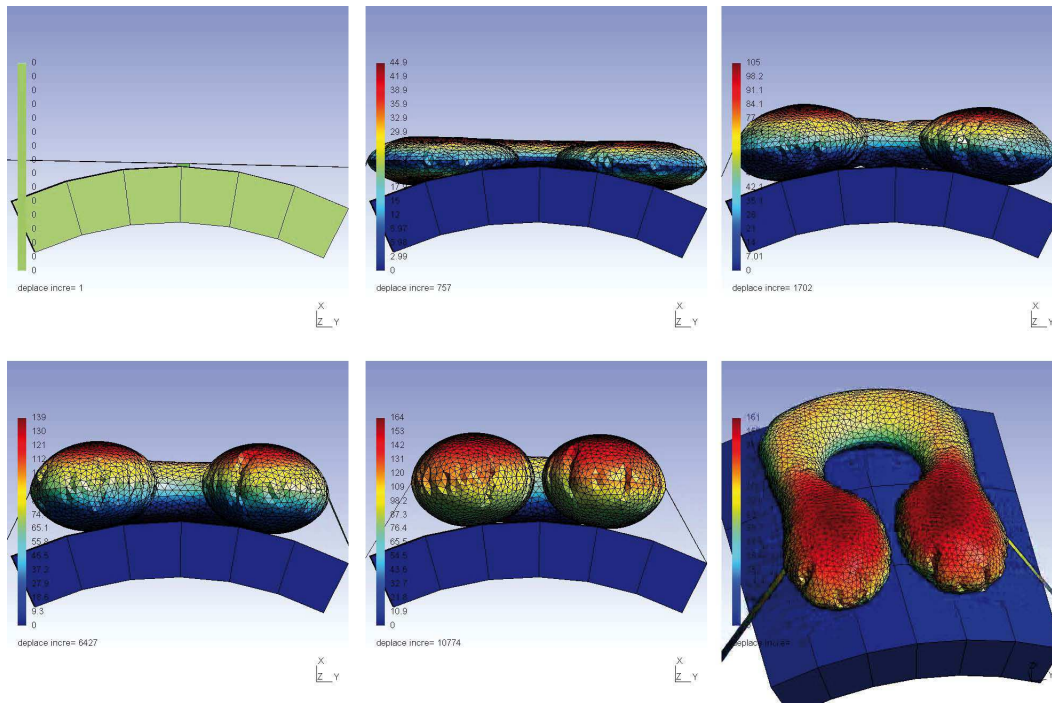


Figure 7.11: Contact test consisting in the inflation of a lifejacket placed on a rigid portion of cylinder and virtually attached to it

7.5 Conclusions and discussion

In this chapter, we proved the applicability of the presented dynamic relaxation methods to the form-finding of a commercial inflatable lifejacket. Also, by using the created mannequin and considering the contact mechanics, we have been able to observe the different behavior of the lifejacket when it is worn by a person. Therefore, some results that can be very interesting for the conception phase in the industry can be observed here.

Taking the contact mechanics into account within the simulation of inflation of the lifejacket is an important as well as difficult task, specially the management of the contact parameters, but we proved that we succeeded on this.

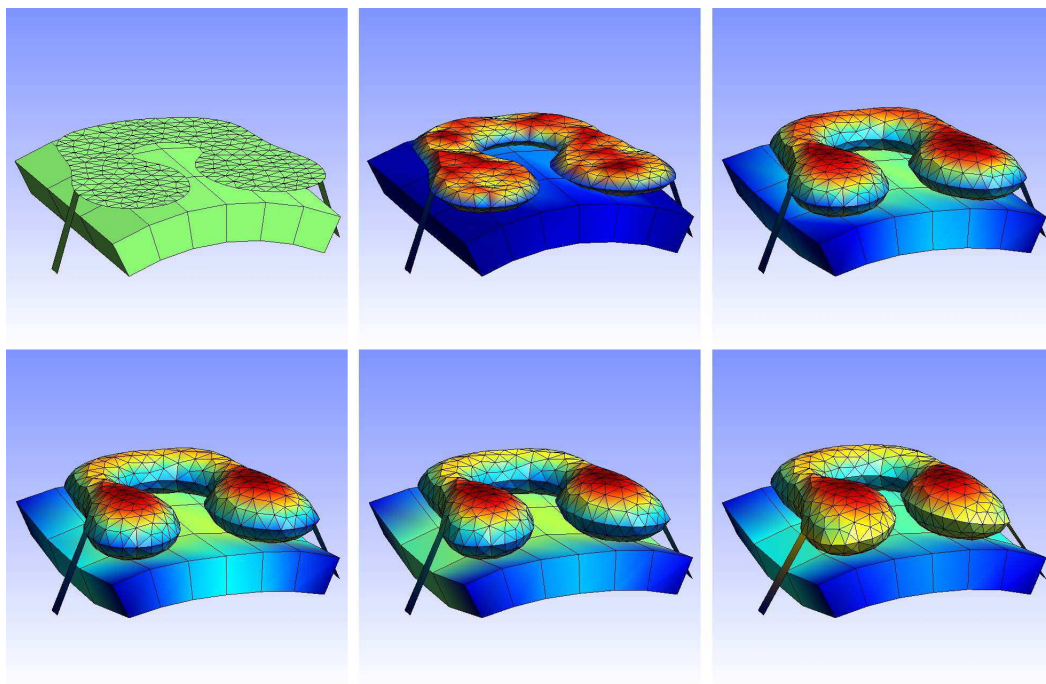


Figure 7.12: Contact test consisting in the inflation of a lifejacket placed on a deformable portion of cylinder and virtually attached to it

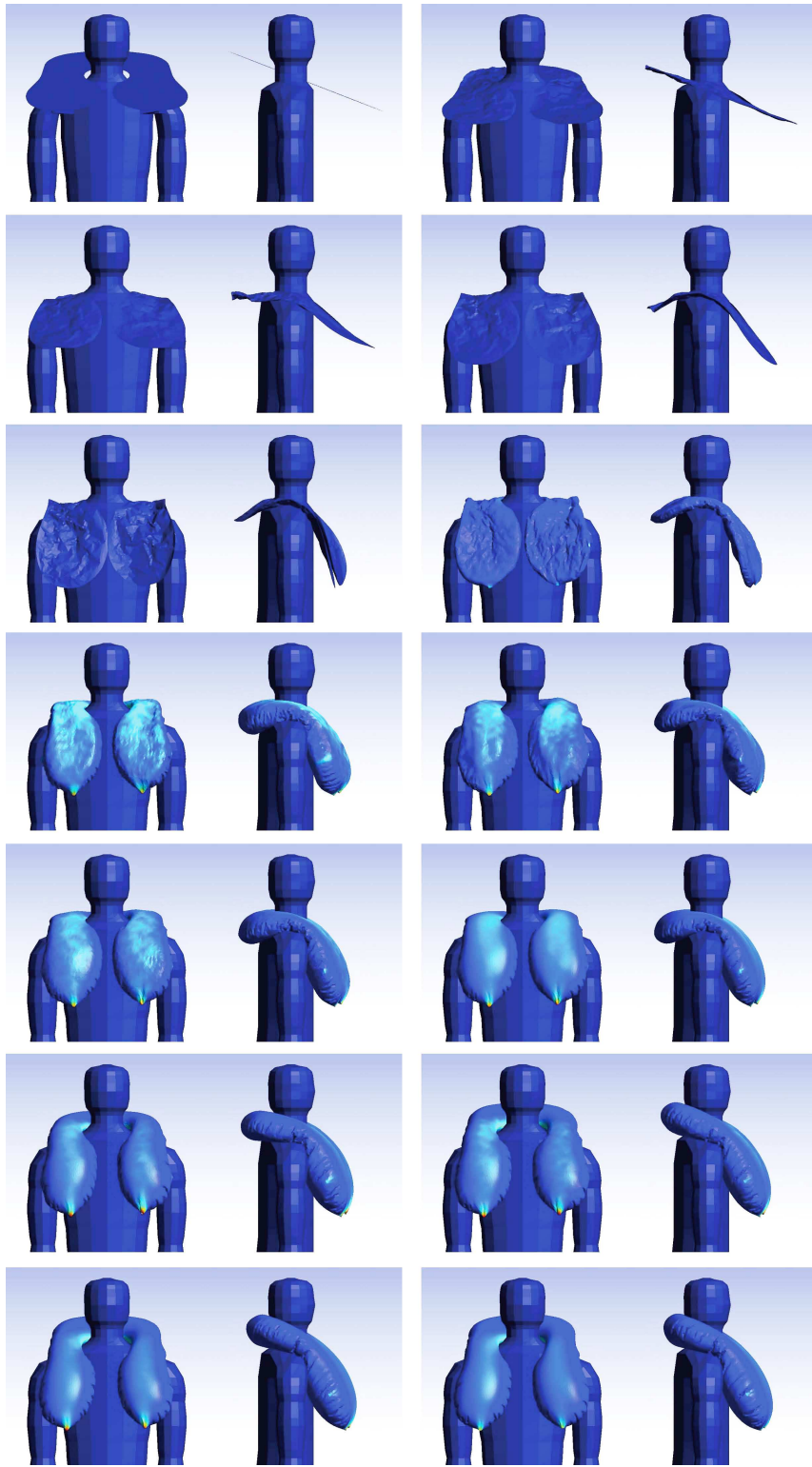


Figure 7.13: Simulation of the inflation of a commercial lifejacket inflating while worn by a person

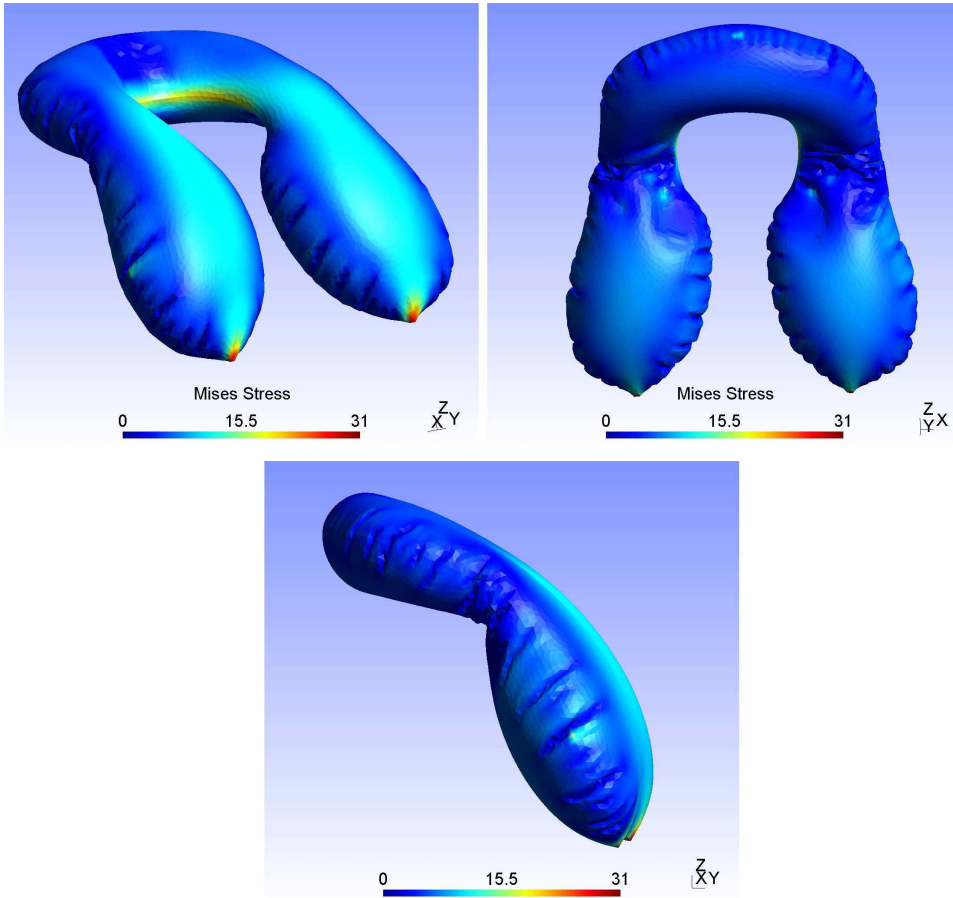


Figure 7.14: Final form of the lifejacket when it is attached to the mannequin

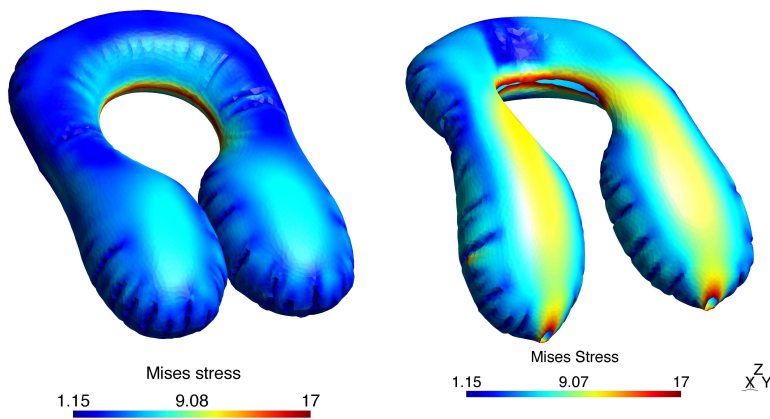


Figure 7.15: Comparison of Mises stresses when the lifejacket is just inflated, and when it is inflated being worn by the mannequin (Note: elements under stresses higher than 17 MPa are hidden)

Chapter 8

Water modelling

8.1 Introduction

The numerical simulation of a mannequin that falls into water includes, obviously, a component of fluid dynamics. However, fluid dynamics is a very wide field, and a deep study of this part of the simulation could be the subject of a whole thesis itself.

The aim of this chapter is just to present a *first approach* to the study of the influence of the forces acting on a body that falls freely into water.

In the context of a simulation to test the operation of a lifejacket worn by a person that falls into water, a correct modeling of the hydrodynamic forces is the key to obtain a realistic and reliable result, since there are several parameters that will be influenced by these forces: the mannequin's speed inside water, the depth it will reach, the lifejacket's inflation time, and finally (and as a result of all these parameters), the time needed for the mannequin to get back to the water's surface. However, it is not our aim to reproduce exactly the reality. As it was indicated in the general introduction of this thesis, the aim is to have a numerical tool that takes into account the approximative different physical phenomena involved and that can serve to obtain tendencies of behavior of each conceived lifejacket model.

A first work on the modeling of water forces had been presented by Troufflard [79]. To calculate the behavior of a body inside water, it would be necessary to determine the efforts applied by the water by means of a fluid/structure interface. The usual procedure for this is to define the fluid domain around the studied body. However, in this case the simulation starts with the body outside the water, so it would be necessary to redefine the fluid frontiers during the calculation, while the dummy is immersing into water, and that would be very difficult. Also the needed calculation time using a fluid/structure interface would be high. Finally, the developments to include this kind of interface in Herezh++ would be long.

Due to all this, it has been decided to calculate the efforts produced by water on each of the finite elements' external faces of the body. The idea is then to represent the hydrostatic and hydrodynamic efforts by forces acting in the surface of the mannequin's mesh.

The main difficulty of this task is that almost all the literature focuses in the pursuit of reducing the hydrodynamic forces, and proposes and analyses mainly aerodynamic shapes; but we could not find studies that could be directly exploitable for geometries such as a lifejacket's one. This means that in this first approach we can only propose what we think is a good modeling of these efforts.

In the following sections, the different efforts that we considered to be relevant will be presented: hydrostatic pressure, hydrodynamic forces and the force of impact with water. Also, an introduction will be made to the concept of added mass.

8.2 Hydrostatic pressure

In equilibrium, at every point in a fluid, the hydrostatic pressure is given by the weight per unit of area of the column of fluid above it, plus any eventual pressure acting on the surface of the fluid.

Therefore, in our particular case study of a person who falls into water, this is the force that will push the person upwards. Pressure acts perpendicularly to all the body's surfaces, but it is bigger in the surfaces that are deeper in the water. To justify this, let's apply Newton's law for a body inside a fluid:

$$\rho \mathbf{a} = \mathbf{f}_{pressure} + \mathbf{f}_{gravity} + \mathbf{f}_{viscous} = -\nabla p + \rho \mathbf{g} + \mu \nabla^2 \mathbf{V} \quad (8.1)$$

where ρ represents the fluid's density, g represents the gravity, μ is the coefficient of viscosity, and \mathbf{V} and \mathbf{a} represent velocity and acceleration, respectively.

If we forget about the speed and acceleration and we focus in the hydrostatic problem, the equation (8.1) becomes:

$$\nabla p = \rho \mathbf{g} \quad (8.2)$$

The general solution for this hydrostatic problem is [122]:

$$p_2 - p_1 = - \int_1^2 \gamma dz \quad (8.3)$$

where 1 and 2 are two points of the body's surface, located at different heights z_1 and z_2 , respectively (see figure 8.1). P_1 and P_2 are the pressures at these points, and γ is the specific weight of the fluid.

Considering that liquids are nearly incompressible, we can neglect density variations (actually, water density increases only around 4.5% at the deepest part of the ocean). With this assumption of constant density, we have then:

$$p_2 - p_1 = -\gamma(z_2 - z_1) \quad \Rightarrow \quad p_2 = p_1 - \gamma(z_2 - z_1) \quad (8.4)$$

Since z_2 is placed deeper than z_1 , being the free surface of water considered as the reference of height, the term $(z_2 - z_1)$ will be negative, and then $-\gamma(z_2 - z_1)$ will be

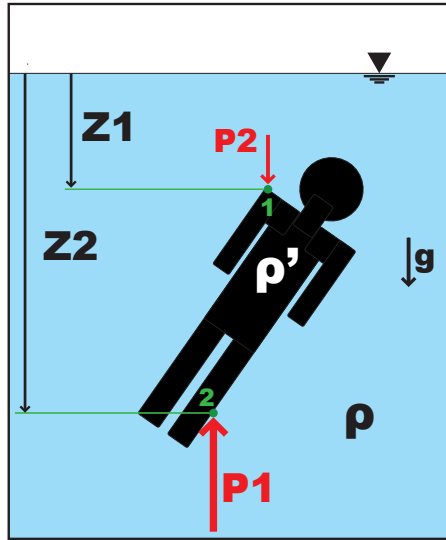


Figure 8.1: Scheme representing the parameters for the calculation of hydrostatic forces

positive, so p_2 is always bigger than p_1 and the resultant pressure on the body will push it upwards.

The hydrostatic pressure has already been implemented in Herezh++. To define the hydrostatic pressure, three parameters need to be defined:

- **Specific weight.** It is the result of multiplying the density and the gravitational acceleration. The fluid studied in this work is water, but, even if slightly, its properties can vary depending on its temperature and salinity. Since the simulation of our case study intends to consider sea water, in the literature we can find its specific weight, for example in the book from F. White [122] (see table 8.1). Thus, we consider $\gamma = 10.05 \text{ N/m}^3$
- **Position and orientation of fluid surface:** Defined by means of a point belonging to the surface and a normal vector. It could be even possible to define a function instead of a point's coordinates, what would allow to simulate waves, for example, if the surface follows a sinusoidal movement.
- **Application area:** The external surface of the mannequin (what will be in contact with water) must be referenced here¹.

8.3 Hydrodynamic forces

Apart of the hydrostatic pressure, when a body is traveling at a speed V through a real fluid initially still, it suffers from the fluid a resistance which opposes the movement.

¹Herezh++ has a function to automatically create a reference that includes all the external surfaces of a body

Fluid	Specific weight γ at 68°F = 20°C	
	lbf/ft ³	N/m ³
Air (at 1 atm)	0.0752	11.8
Ethyl alcohol	49.2	7,733
SAE 30 oil	55.5	8,720
Water	62.4	9,790
Seawater	64.0	10,050
Glycerin	78.7	12,360
Carbon tetrachloride	99.1	15,570
Mercury	846	133,100

Table 8.1: Table showing the specific weight of different fluids at 20 °C [122]

Newton concluded, in a qualitative study, that this resistance should be proportional to ρSV^2 , being ρ the density of the fluid, V the body's speed, and S the projected frontal surface [117].

This resistance offered by the fluid can be considered as a resultant force. The component of this resultant force that is parallel to the free-stream velocity is called the drag force. The drag is a flow loss and must be overcome if the body is to move against the stream. Similarly, the lift force is the component of the resultant force that is perpendicular to the free stream [121]. In our particular case study, these forces will tend to decelerate the mannequin when it falls into water, and then, they will offer a certain resistance for it to get back to the surface. As Newton suggested, these forces depend on the velocity, so they will be more important during the fall.

The hydrodynamic forces and moments on the body are due to only two basic sources (independently of the complexity of the morphology of the immersed body):

- *Pressure distribution* over the body surface
- *Shear stress distribution* over the body surface

The only mechanisms nature has for communicating force to a body moving through a fluid are pressure and shear stress distributions on the body surface. Both pressure p and shear stress τ have dimensions of force per unit area; p acts normal to the surface, and τ acts tangential to the surface. Shear stress is due to the "tugging action" on the surface, which is caused by friction between the body and the fluid [119].

The different forces that can be found in a body which is displacing through a fluid are shown in the figure 8.2.

The most important force is the form drag. The form drag or pressure drag, arises because of the form of the object. Size and shape of the body are the most important

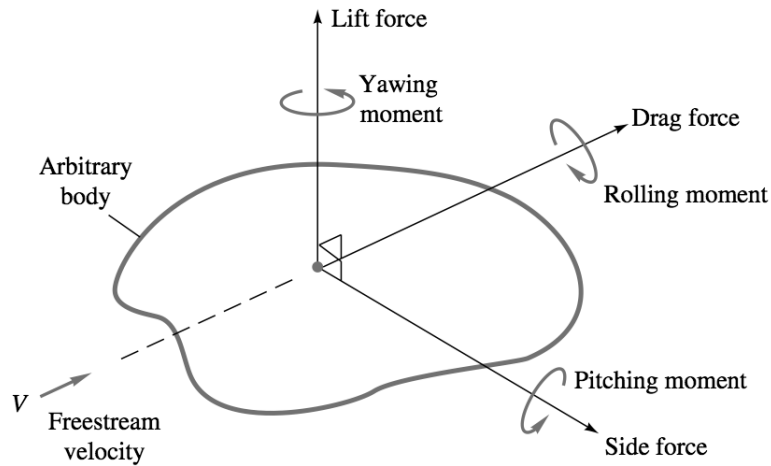


Figure 8.2: Forces and moments on a body immersed in a uniform flow [122]

factors in form drag (the larger the apparent cross-section, the higher the drag). [123]
 Form drag follows the drag equation:

$$F_D = \frac{1}{2}\rho V^2 C_D A$$

where:

- F_D is the force of drag (force component in the direction of the flow velocity)
- ρ is the mass density of the fluid
- V is the velocity of the object relative to the fluid
- A is the reference area, and
- C_D is the drag coefficient, a dimensionless constant

The reference area A is defined as the area of the orthographic projection of the object on a plane perpendicular to the direction of motion. Due to this, A can be much larger than the area of any cross section along any plane perpendicular to the direction motion. Looking at the equation it can also be observed that the fluid drag increases with the square of velocity.

In low speed flows, the drag coefficient should be a function of the body Reynolds number

$$C_D = f(Re)$$

The Reynolds number is a function of the free-stream velocity V and a characteristic length L of the body, usually the length parallel to the stream (we consider low Re numbers in order to simplify the problem):

$$Re = \frac{VL}{\nu}$$

Drag coefficients are defined by using a characteristic area A which may differ depending upon the body shape:

$$C_D = \frac{drag}{\frac{1}{2}\rho V^2 A}$$

The area A is usually one of three types:

- *Frontal area*, the body as seen from the stream; suitable for thick, stubby bodies, such as spheres, cylinders, cars, missiles, projectiles, and torpedoes.
- *Planform area*, the body area as seen from above; suitable for wide, flat bodies such as wings and hydrofoils.
- *Wetted area*, customary for surface ships and barges.

Theory of drag is weak and inadequate except for the flat plate. This is due to the flow separation. Boundary-layer theory can predict the separation point but cannot accurately estimate the pressure distribution in the separated region. The difference between the high pressure in the front stagnation region and the low pressure in the rear separated region causes a large drag contribution called pressure drag. This is added to the integrated shear stress of friction drag of the body [122]:

$$C_D = C_{D.press} + C_{D.fric}$$

Their relative contribution depends upon the body's shape, especially its thickness. Since the aim of this work is not to make an exhaustive study of the hydrodynamics in the simulation, we will use the C_D proposed by F. White [122], showed in the table 8.2.

It also can be observed that there is a different C_D for each of the orientations of the person in the flow (vertical or horizontal). In Herezh++, a solution to manage this could be to compare the direction of the movement with the orientation of the body, and then interpolate between the two available values to obtain the "real" C_D .

Concerning the lift force, analogous to drag force, can be defined as:

$$L = \frac{1}{2}\rho V^2 A C_L \tag{8.5}$$

where C_L is the lift coefficient. Its value is the "complementary" value of C_D . For example, looking at the values indicated in the table 8.2, if $C_D = 9ft^2$, then $C_L = 1.2ft^2$, and vice-versa.

Body	C_D based on frontal area	Body	C_D based on frontal area																					
Cube:	1.07	Cone:	<table border="1"> <tr> <td>θ:</td> <td>10°</td> <td>20°</td> <td>30°</td> <td>40°</td> <td>60°</td> <td>75°</td> <td>90°</td> </tr> <tr> <td>C_D:</td> <td>0.30</td> <td>0.40</td> <td>0.55</td> <td>0.65</td> <td>0.80</td> <td>1.05</td> <td>1.15</td> </tr> </table>	θ :	10°	20°	30°	40°	60°	75°	90°	C_D :	0.30	0.40	0.55	0.65	0.80	1.05	1.15					
θ :	10°	20°	30°	40°	60°	75°	90°																	
C_D :	0.30	0.40	0.55	0.65	0.80	1.05	1.15																	
	0.81	Short cylinder, laminar flow:	<table border="1"> <tr> <td>L/D:</td> <td>1</td> <td>2</td> <td>3</td> <td>5</td> <td>10</td> <td>20</td> <td>40</td> <td>∞</td> </tr> <tr> <td>C_D:</td> <td>0.64</td> <td>0.68</td> <td>0.72</td> <td>0.74</td> <td>0.82</td> <td>0.91</td> <td>0.98</td> <td>1.20</td> </tr> </table>	L/D :	1	2	3	5	10	20	40	∞	C_D :	0.64	0.68	0.72	0.74	0.82	0.91	0.98	1.20			
L/D :	1	2	3	5	10	20	40	∞																
C_D :	0.64	0.68	0.72	0.74	0.82	0.91	0.98	1.20																
Cup:	1.4	Porous parabolic dish [23]:	<table border="1"> <tr> <td>Porosity:</td> <td>0</td> <td>0.1</td> <td>0.2</td> <td>0.3</td> <td>0.4</td> <td>0.5</td> </tr> <tr> <td>$\leftarrow C_D$:</td> <td>1.42</td> <td>1.33</td> <td>1.20</td> <td>1.05</td> <td>0.95</td> <td>0.82</td> </tr> <tr> <td>$\rightarrow C_D$:</td> <td>0.95</td> <td>0.92</td> <td>0.90</td> <td>0.86</td> <td>0.83</td> <td>0.80</td> </tr> </table>	Porosity:	0	0.1	0.2	0.3	0.4	0.5	$\leftarrow C_D$:	1.42	1.33	1.20	1.05	0.95	0.82	$\rightarrow C_D$:	0.95	0.92	0.90	0.86	0.83	0.80
Porosity:	0	0.1	0.2	0.3	0.4	0.5																		
$\leftarrow C_D$:	1.42	1.33	1.20	1.05	0.95	0.82																		
$\rightarrow C_D$:	0.95	0.92	0.90	0.86	0.83	0.80																		
	0.4	Average person:	<p>$C_D A \approx 9 \text{ ft}^2$ $C_D A \approx 1.2 \text{ ft}^2$</p>																					
Disk:	1.17	Pine and spruce trees [24]:	<table border="1"> <tr> <td>U, m/s:</td> <td>10</td> <td>20</td> <td>30</td> <td>40</td> </tr> <tr> <td>C_D:</td> <td>1.2 ± 0.2</td> <td>1.0 ± 0.2</td> <td>0.7 ± 0.2</td> <td>0.5 ± 0.2</td> </tr> </table>	U , m/s:	10	20	30	40	C_D :	1.2 ± 0.2	1.0 ± 0.2	0.7 ± 0.2	0.5 ± 0.2											
U , m/s:	10	20	30	40																				
C_D :	1.2 ± 0.2	1.0 ± 0.2	0.7 ± 0.2	0.5 ± 0.2																				
Parachute (Low porosity):	1.2																							

Table 8.2: Drag of three-dimensional bodies in a turbulent flow [122]

The hydrodynamic loading has also been implemented in Herezh++, and it includes both drag and lift forces, and also a force due to the shear (to use when this part is very important, such as in the case of liquid polymers). The parameters to be defined are the following:

- A reference for all the body's external surfaces (similar to the case of hydrostatic pressure).
- The drag coefficient C_D
- The lift coefficient C_L
- The fluid's density

8.4 Added mass and impact force

Besides hydrostatic pressure and hydrodynamic forces, there are another phenomena that could be considered, but that escape the aims of this work. One of this phenomena is the *added mass*. Added mass is a concept used in hydrodynamic engineering, and it is applied to objects accelerating through liquids, and is a direct link to how much the liquid resists the acceleration (the objects inertia).

Explained with an example [110], we can imagine a box down into the sea. To be able to move the box up and down, it is necessary to overcome both the water's friction along the sides of the box (drag; dependent on velocity), but it is also necessary to move the water at the top and bottom of the box (added mass; dependent on acceleration). What happens in practical terms is that when the box is moved down, a lump of water becomes part of the object and moves with it, while water flows around the box and this enclosed water. This enclosed water is called added mass, and it affects the inertia of the object. If an object has a large body of added mass one needs to spend a much larger force to achieve the same acceleration:

$$\begin{aligned}
 F_1 &= m_1 a_1 \\
 F_2 &= (m_1 + m_2) a_2 \\
 a_1 = a_2 &\Rightarrow F_2 = F_1 \left(1 + \frac{m_2}{m_1} \right)
 \end{aligned}$$

where m_1 is the object's mass, and m_2 is the added mass.

The size of the added mass (the enclosed area) depends much on the geometry of the object. For example, a suction anchor will have a large added mass as it encloses much water inside its bucket, while a streamlined object will have nearly zero added mass, because there is little for the water to hold on to.

However, even if this effect could be have some importance in our case study, it would require a long development to make a full study of added mass, and it might require a fluid/structure interface, what escapes the aims of this work (simplicity and small calculation times).

8.4.1 Impact force

Up to this point, only two forces were considered acting in the interaction between water and the mannequin: the hydrostatic pressure and approximated hydrodynamic forces (several assumptions are made to be able to use basic theoretical equations, such as uniform fluid around the body, no losses due to bubbles, etc).

When we carried out the first simulations of an object falling into water in Herezh++, we realized that the mannequin felt very deep into the water. This could be due to our simplifications, but also to some important phenomenon or force that had not been taken into account. It was not being considered another factor that might be important: the impact of the body with water. This impact could generate important forces that could change the "initial conditions" when the body enters into water (a sudden deceleration occurs, and then the velocity inside water would be inferior).

Studying this phenomenon is very complex and even if existing, we were not able to find any works studying the efforts appearing when a person impacts with water. The most similar works found were concerning naval engineering, to study the impact of ships' forebody with water, phenomenon known in literature as *slamming*.

The objective in this part is to find an estimation of these impact forces. We only intend to find a force in the order of magnitude of the real one, and not precise values, since it would be very long and complex, and also very time-consuming in the simulations, all according to the existing literature.

8.4.1.1 Slamming

According to Constantinescu [114], the slamming phenomenon designs the impact that takes place between a solid body and the free surface of water, being the interaction duration very short. This impact is a highly non-linear and random phenomenon, and it can depend on several impact conditions (direction, speed of impact, shape of the body,...), among other phenomena which can occur (air traps, waves, etc).

The resultant hydrodynamic force of the slamming exhibits a characteristic time history. While the drop velocity decays, causing a decrease of the slamming pressure, the wetted area increases, creating an opposite effect. The force increases from its initial zero value to a maximum hydrodynamic force F^* at a time t^* . Later, the velocity reduction effect definitively prevails and the hydrodynamic force is progressively reduced to zero. The resultant non-dimensional curve is shown in the figure 8.3.

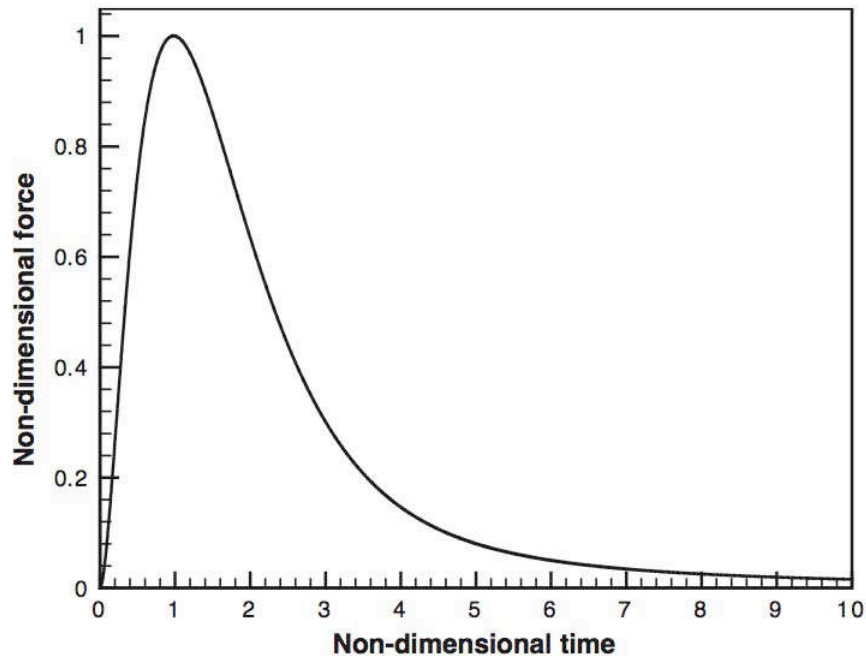


Figure 8.3: Non-dimensional time history of the hydrodynamic force [112]

Slamming has been studied especially in naval hydrodynamics. Pioneering research has been carried out by von Karman and Wagner. The first studies were interested on the loads on seaplane floats. Later on, the slamming has been studied in ship design, especially in the case of flat bottoms of large ships (such as oil tankers); and nowadays

the interest concerns fast ships where light structures impact at high speed on the rough sea with a high frequency of impacts emphasizing the fatigue damage to the materials [112].

The main difficulty of the study of slamming lies in the fact that boundaries of the different domains (solid, fluid and air) are unknown in advance and they must be considered as well as unknowns in the problem. We are not going that deep in this thesis, but it's worth mentioning and discussing some of the findings for possible future works.

First studies of slamming phenomenon The first studies of slamming lead to the work of von Karman, who worked on a 2D model of a dihedral for simulating the pressure exerted in the floats of hydroplanes during the water landing. He proposed the following expression for the impact force [124]:

$$F = \frac{v_0^2 \cot \beta}{\left(1 + \frac{\rho \pi d}{2m}\right)^3} \rho \pi d$$

where m is the mass per length unit, β is the incidence angle, and v_0 is the speed just before the contact. Note that he took into account the added mass, by considering that it should be included in the global formula ($m_a = \frac{1}{2} \pi \rho d^2$, with d being the wetted half-length). Thus, the expression of the maximum pressure that he proposed was:

$$P_{max} = \frac{\rho v_0^2}{2} \pi \cot \beta$$

where the first part ($\frac{\rho v_0^2}{2}$) represents the dynamic pressure corresponding to the speed v_0 , the second part ($\pi \cot \beta$) is a theoretical factor. In his model, Von Karman neglected the increase of the wetted surface, and it is suitable for big angles of incidence β .

While Von Karman is considered the pioneer in the study of slamming, Wagner is considered a reference. Wagner is the formulated a more realistic model for the hydrodynamic impact theory, also suitable for small angles β . Opposite to Von Karman, Wager supposes that the wetted surface and the added mass must be bigger during the impact.

Wagner studied the water impact on rigid two-dimensional bodies by approximating the bodies with a flat plate and taking into account the water uprise on the body in a simplified way. What he did was a linearization of both the wetted and free surface, that are projected on the initial free surface at rest. Because of the blunt body approach, the bodies are assumed to have small deadrise angles in the range of 4 up to 20 degrees [125]. When deadrise angles are smaller than 4 degrees, an air cushion is formed, which reduces the pressure on the structure and as a result, Wagner theory overestimates the pressure by a large margin [113]. In fact, Wagner's model, in its original form, predicts both infinite pressure and speed in the surroundings of the contact point. Some corrections were proposed by other researchers to solve this problem in following works.

General assumptions in slamming phenomenon Usually, in the study of slamming, due to the complexity of the problem, some basic assumptions are made at the beginning of the impact:

- *Gravitational acceleration is negligible* compared to the deceleration of the impacting body. Therefore, gravity is often neglected.
- The acoustic pressure $p_{ac} = \rho cv$ is more important than hydrodynamic pressures occurring. Consequently, the fluid can be considered as *incompressible*.
- Times are considered shorts, so the boundary layer, with a thickness $e = \sqrt{\nu t}$, doesn't have time enough to be developed (being ν the cinematic viscosity). The *fluid* can be considered as *perfect*.
- The flow is *irrotational* in the beginning of the contact, and it stays similar in the following.
- The thickness of the body is big enough to *neglect superficial tension* in the fluid [113].
- In works where the sea is concerned, the volume of fluid is big enough to *neglect the border effects*.
- Another consideration concerns the *water jet* in the moment of the impact. The jet appearing in the impact of a body into water is neglected. This hypothesis is admissible in the sense that the contribution of this jet to the efforts applied to the impacting body are negligible. Also, just a little fluid is ejected in the jet. Anyway, the ejection speed is very high, so from an energetic point of view, the jet should be maybe taken into account [114]. In the case of this work, we are just interested in the efforts applied on the body, so we consider this assumption as valid.
- Generally, slamming theories don't consider the eventual *existence of air* in the impact zone. But in reality, due to the small angles β it exists an air layer between the body and the surface of water. The presence of prisoned air carries to a diminution of the pressure level and decreases this way the negative effects of slamming. Consequently, the presence of air has a very important role in these slamming phenomena. According to the bibliography, the effects of air compression appear for very small β angles. Wagner theory seems no be not valid in the case of $\beta < 4^\circ$ [114]. However, some researchers, such as Bagnold [116], developed theories taking this effect into account. His model supposes the existence of a layer of air, having a damping effect, as shown in the figure 8.4

Recent works in slamming As mentioned previously, the studies of slamming begun around 1931 with the works of Wagner. Even nowadays, works concerning this phenomenon still study the 2D case, trying to find a fast way to calculate the pressure distribution in the impact considering the variation of the wetted surface. The study of the impact in 3D begins in the extension of Wagner's work with axisymmetric bodies.

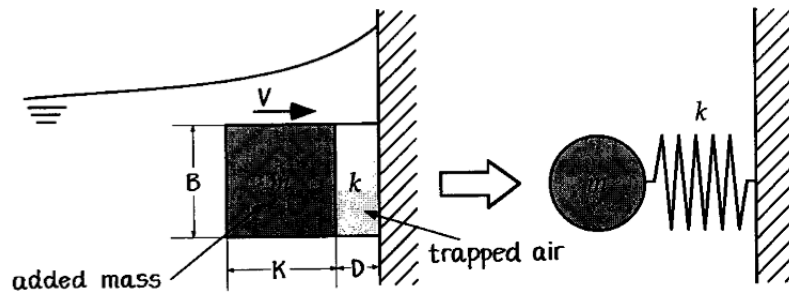


Figure 8.4: Bagnold's model [114]

These cases could be solved by two-dimensional theories of slamming. Some authors developed a 3D theory from the 2D model of Wagner. There is a classification for the study of different categories of slamming of flat structures [114]:

- Impact type Wagner, for the penetration of inclined flat bottom. This kind of slamming is typical in slow-speed ships.
- Impact type Bagnold, for a vertical penetration ($\beta = 0$). Important effects of compressibility are observed in this case.
- Impact type Wagner for perpendicular entering ($\beta = 0$). Small effects of air compressibility are observed. This kind of slamming is just observed for high-speed ships

A bibliographic review shows that for the three-dimensional case, theoretical aspects are far from being solved. The 3D analysis use 2D models empirically corrected (axisymmetric models). This kind of solutions are needed because the numerical 3D simulations are still limited by the huge deformations of fluid's mesh [114].

Carcattera and Ciappi [112] carried out impact tests in order to validate their analytical model, using a rigid structure (dihedral angle $\beta = 30^\circ$). They measured the historical of the effort during the impact and the elastic response of the system. To avoid tridimensional effects, the geometric characteristics of the structure respected certain conditions.

Malleron [115], in his thesis work, uses the generalized Wagner model to precisely study the impact of rigid sections of arbitrary shape sections (symmetrical or not) into a fluid surface. This method allows to avoid the hypothesis of small angle established by Wagner. But he still works with the 2D case, and he indicates that to extend the application to three-dimensional bodies, the first task would be the study of axisymmetric bodies, which would permit to simplify the problem just considering the generator defining the body.

Hydroelastic coupling in slamming The main difficulty of coupling is that the structure deformation must be calculated at the same time that the hydrodynamic problem

unknowns (local loadings and wetted surface). So, even if the hydrodynamic model is linearized, the problem keeps highly non-linear.

Calculations carried out by Malleron [115] indicate that while calculation times for rigid bodies are made in around one minute, for hydroelastic bodies, they rise to the order of hours. It is due to this that in the present work, as we told previously, we are not interested in a "deep" study of the hydrodynamics efforts.

Slamming applied to the mannequin's simulation Seen the slamming phenomenon, it can be thought that something similar occurs when a person impacts into water. Of course, the complexity in the case of a human body shape is much higher. In most of the slamming works, the case considered is two-dimensional, and even symmetrical. There are just a few researchers who worked with three-dimensional models, but almost all of them were axisymmetrical.

Also, all the seen works concerning slamming made some assumptions that are not directly applicable to the case of the mannequin, such as a small incidence angle (β); in our case, this angle is random, because the mannequin can fall in any position, and the mesh elements can impact against water with any angle. It is also possible that due to the complex body's shape, they appear air traps, being the pressure distribution importantly modified.

Since this work's aim is not to make a detailed study of fluid mechanics of the fall into water, but to seek for a trend in the simulation tests, the path to follow will be to estimate an impact force based on the theoretical and experimental works found. Two options matched our requirements of simplicity (in terms of ease of implementation in our FE software) and were finally considered: von Karman's proposal and Carcaterra's one. Von Karman's has already been presented previously, and we will present Carcaterra's proposal in the following.

8.4.1.2 Impact force by Carcaterra [112]

Carcaterra considered a rigid-body impacting the water surface with a given initial velocity. He found that hydrodynamic force exhibited the characteristic time history shown in the figure 8.3. His theoretical model was the shown in the figure 8.5.

where ζ is the depth (postivie downward), S_F is the free water surface and S_B the water-body interface, and the angle β is assumed to be small.

In his analysis, Carcaterra, makes an analytical development and he obtains the maximum impact force F^* and the time t^* when it occurs (see figure 8.5):

$$F^* = F_h(\zeta^*) = \left(\frac{5}{6}\right)^3 \frac{v_0^2}{\tan\beta} \sqrt{\frac{2\pi}{5} \rho \gamma^2 m} \quad (8.6)$$

$$t^* = t(\zeta^*) = \frac{16}{15} \sqrt{\frac{2m}{5\pi\rho\gamma}} \frac{\tan\beta}{v_0} \quad (8.7)$$

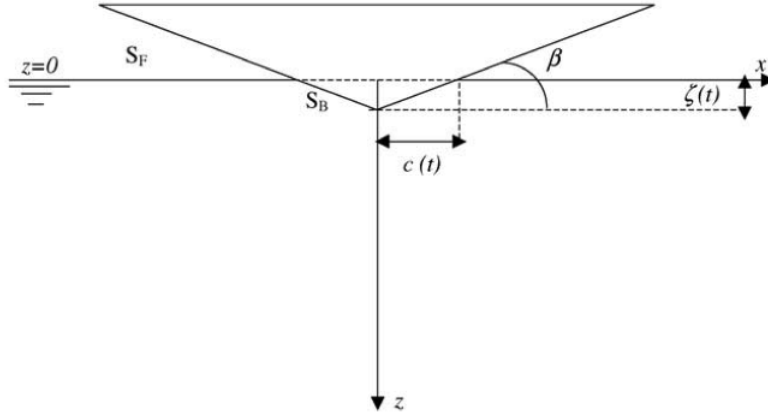


Figure 8.5: Sketch of the section and definition of the principal parameters [112]

and

$$\zeta^* = \frac{15}{16} v_0 t^* \quad (8.8)$$

where ζ^* is the depth at which the maximum occurs.

Finally, simple mathematics leads to $F^* t^* = \frac{20}{81} m v_0 \approx 0.247 m v_0$.

Also, Carcaterra proposed to use a suitable non-dimensional form of the hydrodynamic load. Rewriting in terms of non-dimensional variables: $\tilde{t} = t/t^*$, $\tilde{\zeta} = \zeta/\zeta^*$, $\tilde{F}_h = F_h/F^*$, the hydrodynamic force takes the form below:

$$\begin{aligned} \tilde{F}(\tilde{t}) &= \frac{81}{20b} \left[\frac{2}{2 + \tilde{\zeta}^2/b} \right]^3 \tilde{\zeta} \\ \tilde{\zeta}(\tilde{t}) &= -\frac{2}{\sqrt{2\gamma/5} Q^{1/3}} + \frac{Q^{1/3}}{\sqrt{2\gamma/5}} \\ Q(\tilde{t}) &= 3a\tilde{t}\sqrt{8 + (3a\tilde{t})^2} \\ a &= \sqrt{2\gamma/5} \frac{16}{15}, \quad b = \frac{5}{2} \left(\frac{15}{16} \right)^2 \end{aligned} \quad (8.9)$$

In the analysis made by Carcaterra, γ is constant and has a value $\gamma = \pi/2$. However, more accurate investigations of this point show that this is accurate only when the deadrise angle tends to zero.

With this non-dimensional equations, a single time history of the hydrodynamic force is determined, being each possible impact case determined by suitably scaling the force and time axes. The curve given by these equations is the one presented previously (8.3).

8.5 Conclusions and discussion

Hydrostatic pressure and hydrodynamic forces have been successfully implemented in Herezh++ and the different simulations present that a body defined to be inside water behaves in a way close to reality (results are not presented here since it can be appreciated only in animations).

However, concerning the impact forces, we did not get to good results. Using either formulae or Von Karman's model could be a good choice because they seem easy to apply them directly to our case (just by substituting parameters), but the necessary assumptions in our case induce to think that maybe the result would be inexact: both Von Karman and Carcaterra work in 2D, with a small deadrise angle, without considering air traps, etc, and as mentioned previously this features could have a big influence in the impact force. Also, a first approximation was tried to be made substituting the parameters in the equations by ours, and the maximum force obtained was too high (order of tens of kN).

Therefore, further studies and improvements must be made in this field. However, we consider that the impact force is important only if we need to carry out a simulation that reproduces reality, what is not the aim: the aim is to see the different behavior of lifejackets' concepts; and since most of the times the lifejacket is folded when the person enters into the water, the behavior of the lifejacket can only be seen when the person is already inside water. The simulation could be therefore started from this point: a mannequin inside water, that can be placed at random chosen depths and orientations.

Chapter 9

General conclusion and perspectives

9.1 Conclusions

The background of this work was the contribution to the creation of a numerical tool usable in the industry that allowed to test the behavior of different inflatable lifejacket's models in their usage conditions, i.e., when a person falls into water and it inflates to provide a buoyancy aid. With that objective in the background, several developments were made in different fields of the simulation.

The main contribution of this thesis is made in the field of form-finding of inflatable structures. Particularly, an exhaustive study of dynamic relaxation (DR) has been made. Two scientific papers are presented on this subject; a first one where two new proposals of dynamic relaxation with kinetic damping are made; and a second one where a comparison of different dynamic relaxation methods in the field of form-finding of inflatable structures is made (including our presented new proposals).

In the first paper, our first proposal was an extension of the DR method proposed by Barnes, Han and Lee. The advantage of our proposal is the wider range of applicability: while Barnes-Han-Lee proposed a DR method usable with triangular elements in elastic behavior, we proposed a modification of their method that showed efficiency with *any kind of element* (2D or 3D, with linear or quadratic interpolation) and *any reversible behavior*. Also, using an incremental formulation, we proved that it could be an useful alternative to the classic Newton's method in the cases where instabilities are found. Our second proposal was based on the works of Underwood and its efficiency and reliability has also been proved.

In the second paper, our two proposals were compared with some relevant existing methods in the literature (from the earlier works of Underwood to the latest developments found in DR). Therefore, after a full review of the existing literature, we worked on several case studies. Our proposals proved to have an efficiency similar to the existing methods, and even better under certain conditions.

By means of an image correlation software (Aramis) and a simple inflatable air bag, we made a rough comparison between the inflated final form of the real air bag and the result of our simulations when using DR methods. Despite of the different limitations in

the setup of the experimental 3D measuring, a good correlation between simulation and reality has been shown.

Also, some tensile tests have been made on the technic textile used by Plastimo in the manufacturing of their lifejackets. The aim was to observe the behavior of the technic textile. In the different tests made, we could observe that an elastic behavior could be not enough to describe the real behavior. We have put in evidence the existence of hyperelasticity, viscosity and an orthotropic behavior.

In order to contribute to the creation of the numerical tool permitting to test the behavior of the lifejackets' conceptions, a parameterized human body model has been created. The creation procedure in C++ has been described in detail. The aim was to obtain a simple human model made with the lowest possible amount of finite elements (in order to have fast calculations). The created model has only 156 elements that, by means of some introduced parameters, can be given any shape, being virtually possible to model any kind of human shape.

The simulation of the inflation of the commercial lifejacket has been presented. A good correlation with the real final inflated lifejacket could be observed. The studied DR methods have shown once again their correct functioning when dealing with a complex shape. Also the contact mechanics in Herezh++ have been studied, carrying out the simulation of different case studies, in order to test the good working. Finally, and as the final application, we attached the lifejacket to the previously created mannequin, and we carried out the inflation of the lifejacket. That simulation allowed to observe that the stress distribution on the lifejacket is very different when it is worn by a person than when it is just inflated. Having succeeded with this simulation proves that it is also possible to approximate the reaction forces that the lifejacket exerts on the person wearing it.

Finally a first approach to water dynamics has been made. The hydrostatic pressure and basic hydrodynamic forces already implemented in Herezh++ have been successfully tested. We also introduced another different problem, that is the impact with water, presenting a compendium of some relevant studies on it.

9.2 Perspectives

Academic perspectives

In the study on DR method, future research will be made in order to validate the presented DR proposals when using different complex laws of behavior (with non-reversible behaviors e.g. elasto-plasticity, viscosity, etc). This is a work that we plan to do in a short term.

Also, In the case of the 3D measuring, the limitations can be tried to be overcome, by conceiving an appropriate support for the air bag. Better results can probably be obtained in this case that allow to compare simulation and reality. The final aim would be to compare the transient part of the inflation, by using the DR methods combined with an incremental formulation (to obtain different stages of the inflation).

We showed the complex behavior of the technic textile. Therefore, a complex behavior describing this could be implemented in Herezh++ in order to obtain simulation results closer to the real behavior of the textile. Also, it could be a good idea to make tests at different controlled temperatures, with the aim of checking the behavior under the influence of higher temperatures. It is currently possible to model in Herezh++ a visco-hyperelastic behavior with temperature-dependent parameters, what would probably improve the transient part of the simulation. In order to use this model, it would be necessary only to identify the parameters.

A deeper study of water dynamics could be made, or even the possibility of doing a coupling fluid-structure could be studied. However, this would make the simulations considerably longer. This way, the impact force between the person and the water could be probably better studied.

Industrial perspectives

We are currently working on tests that try to simulate the mannequin inside water wearing the lifejacket that inflates, to observe its behavior and how it floats back to the surface.

The parameterized mannequin could be improved by studying the articulations in a different way. Probably considering the modeling of an internal "skeleton" that managed the kinematics, so that the external surface of the body acted only as the "interface" with the environment. Another point to work in is the behavior of the mannequin. For the moment, an approached behavior has been defined for it; however, on this behavior depends the deformation of the mannequin with the lifejacket. It would be probably interesting to have several different behaviors; a first one that concerns the most external part of the mannequin that would allow to obtain realistic local deformations; then, another layer of elements that would manage the global deformations. However, the aim is not to obtain a very realistic mannequin, but a global behavior close to reality, and locally exact in order to check the influence of the lifejacket on it.

Concerning the simulation of the lifejacket, a next stage of improvement could be the integration of self-contact in the software with the aim of being able to fold the lifejacket and therefore simulating its deployment.

Bibliography

- [1] J. Troufflard, "Etude numerique et experimentale des structures gonflables: application aux gilets de sauvetage gonflables". Universite de Bretagne-Sud; March 2011.
- [2] G. Rio, H. Laurent and G. Bles, "Asynchronous interface between a finite element commercial software Abaqus and an academic research code, Herezh++". *Advances in Engineering Software*, vol. 39, no. 12, pp. 1010-1022, 2008 (ISSN 0965-9978).
- [3] A. Soive, "Apports a la methode des elements finis appliques aux calculs de structures en dynamique rapide et amortissement numerique". PhD thesis, Universite de Bretagne-Sud, 2003.
- [4] G. Rio, A. Soive and V. Grolleau, "Comparative study of numerical explicit time integration algorithms". *Advances in Engineering Software*, vol. 35, pp. 252-265, 2005.
- [5] L. Mahéo, V. Grolleau, G. Rio, "Damping efficiency of the Tchamwa-Wielgosz explicit dissipative scheme under instantaneous loading conditions". *Comptes Rendus Mécanique*, vol. 337, no. 11-12, pp. 722-732, Nov. 2009
- [6] L. Mahéo, G. Rio, V. Grolleau, "On the use of some numerical damping methods of spurious oscillations in the case of elastic wave propagation". *Mechanics Research Communications*, vol. 38, no. 2, pp. 81-88, 2011.
- [7] "Pressure vessels". College of Engineering, Colorado State University. <http://www.engr.colostate.edu>. Direct link to the document: www.engr.colostate.edu/~dga/mech325/handouts/pressure_vessels.pdf
- [8] R. Courant, K. Friedrichs, H. Lewy, "On the partial differential equations of mathematical physics". *IBM Journal*, March, 1967.
- [9] Gilbert Strang, "Linear Algebra and Its Applications", vol. 30, Oct. 1976.
- [10] Stanley P. Frankel, "Convergence rates of iterative treatments of partial differential equations". *Electronic Engineering*, vol. 20, no. 30, pp. 208-213, 1950.
- [11] J.M. Biggs, "Introduction to structural dynamics". McGraw-Hill, New York, 1964.

- [12] M. Papadrakakis, "A method for the automatic evaluation of the dynamic relaxation parameters". *Computer Methods in Applied Mechanics and Engineering*, vol. 24, no. 1, pp. 35-48, Jan. 1981.
- [13] A. K. Chopra, "Dynamics of structures. Theory and applications to earthquake engineering". Prentice Hall Upper Saddle River, New Jersey, 1995.
- [14] R. Clough and J. Penzien, "Dynamics of structures". Computers and Structures, Inc. Third Edition, 1995.
- [15] J. Rodriguez, G. Rio, J.M. Cadou, J. Troufflard, "Numerical study of dynamic relaxation with kinetic damping applied to inflatable fabric structures with extensions for 3D solid element and non-linear behavior". *Thin-Walled Structures*, vol. 49, no. 11, pp. 1468-1474 (2011).
- [16] Lewis WJ. *Tension Structures, Form and Behavior*. T. Telford; 2003.
- [17] J. Thomas, Wielgosz C., "Deflections of highly inflated fabric tubes". *Thin-Walled Structures* 2004;42:1049-66.
- [18] Rio G. Herezh++: FEM software for large transformations in solids. Laboratoire d'ingénierie des matériaux de Bretagne (UEB-UBS); dépôt APP (Agence pour la Protection des Programmes) - Certification IDN.FR.010.0106078.000.R.P.2006.035.20600; 2011.
- [19] Vandembroucke A, Laurent H, Hocine N, Rio G. A hyperelasto-visco-hysteresis model for an elastomeric behavior: Experimental and numerical investigations. *Computational Materials Science* 2010;48:495-503.
- [20] H. Laurent and G. Rio. Formulation of a thin shell finite element with continuity and convected material frame notion. *Computational Mechanics*, 27(3):218-232,2001. ISSN 0178-7675.
- [21] S.E. Han and K.S. Lee, "A study of the stabilizing process of unstable structures by dynamic relaxation method". *Computers & Structures*, vol. 81, no. 17, pp. 1677-1688, Aug. 2003
- [22] T. Wu and E. Ting, "Large deflection analysis of 3D membrane structures by a 4-node quadrilateral intrinsic element". *Thin-Walled structures*, vol. 46, no. 3, pp. 261-275, Mar. 2008.
- [23] G. Ramesh, "Geometrically non-linear analysis of plates and shallow shells by dynamic relaxation". *Computer Methods in Applied Mechanics and Engineering*, vol. 123, no. 1-4, pp. 15-32, June 1995.
- [24] C. Russell, "Deployment simulation of inflatable tensegrity structures". *International Journal of Space Structures*, vol. 23, no. 2, pp. 63-77, 2008.

- [25] R. Wood, "A simple technique for controlling element distortion in dynamic relaxation form-finding of tension membranes". *Computers & Structures*, vol. 80, no. 27-30, pp. 2115-2120, Nov. 2002.
- [26] M. Rezaiee-Pajand and M. Taghavian Hakkak, "Nonlinear analysis of truss structures using dynamic relaxation". *International Journal of Engineering B: Applications*, vol. 19, no. 1, Dec. 1996
- [27] M. Rezaiee-Pajand and J. Alamatian, "The dynamic relaxation method using new formulation for fictitious mass and damping". *Structural Engineering and Mechanics*, vol. 34, no. 1, pp. 109-133, 2010.
- [28] J.O. Hallquist, "LS-DYNA Theoretical manual". Livermore Software Technology Corporation, May 1993.
- [29] G.R. Joldes, A. Wittek, and K. Millner, "Computation of intraoperative brain shift using dynamic relaxation". *Computer Methods in Applied Mechanics and Engineering*, vol. 198, no. 41, pp. 3313-3320, Sept. 2009.
- [30] M.R. Barnes, "Form-finding and analysis of prestressed nets and membranes". *Computers & Structures*, vol. 30, no. 3, pp. 685-695, 1988.
- [31] M. Rezaiee-Pajand, M. Kadkhodayan, J. Alamatian and L.C. Zhang, "A new method of fictitious viscous damping determination for the dynamic relaxation method". *Computers & Structures*, vol. 89, no. 9-10, pp. 783-794, May 2011.
- [32] P.A. Cundall, "Explicit finite difference methods in geomechanics", in *E.F. Conference on the Numerical Methods in Geomechanics*, Blacksburg, VA, 1976.
- [33] B.H.V. Topping and A.I. Khan, "Parallel computation schemes for dynamic relaxation". *Engineering Computations*, vol. 11, no. 6, pp. 513-548, 1994.
- [34] P.D. Gosling and W.J. Lewis, "Optimal structural membranes. Form-finding of prestressed membranes using a curved quadrilateral finite element for surface definition". *Computers & Structures*, vol. 61, no. 5, pp. 885-895, Dec. 1996.
- [35] D. Wakefield, "Engineering analysis of tension structures: theory and practice". *Engineering Structures*, vol. 21, no. 8, pp. 689-690, Aug. 1999.
- [36] M.R. Barnes, "Form finding and analysis of tension structures by dynamic relaxation". *International Journal of Space Structures*, vol. 14, no. 2, pp. 89-104, 1999.
- [37] S. Adriaenssens, "Tensegrity spline beam and grid shell structures". *Engineering Structures*, vol. 23, no. 1, pp. 29-36, Jan. 2001.
- [38] B. Domer, E. Fest, V. Lalit and I.F.C. Smith, "Combining dynamic relaxation method with artificial neural networks to enhance simulation of tensegrity structures". *Journal of Structural Engineering*, vol. 129, no. 5, pp. 672, 2003.

- [39] N.B.H. Ali, L. Rhode-Barbarigos and I.F.C. Smith, "Analysis of clustered tensegrity structures using a modified dynamic relaxation algorithm". *International Journal of Solids and Structures*, vol. 48, no. 5, pp. 637-647, Mar. 2011.
- [40] N.B.H. Ali, L. Rhode-Barbarigos and I.F.C. Smith, "Active tensegrity structures with sliding cables-static and dynamic behavior", *csma2011.lmgc.univ-montp2.fr*, pp. 1-8, 2011.
- [41] C. Douthe, O. Baverel and J.F. Caron, "Form-finding of a grid shell in composite materials". *Journal-International association for shell and Spatial Structures*, vol. 150, pp. 53, 2006.
- [42] J. Troufflard, J.M. Cadou and G. Rio, "Recherche de forme des gilets de sauvetage gonflables". *Mecanique & Industries*, vol. 11, no. 2, pp. 117-122, Sept. 2010.
- [43] K.S. Lee, S.E. Han and T. Park, "A simple explicit arc-length method using the dynamic relaxation method with kinetic damping". *Computers & Structures*, vol. 89, no. 1-2, pp. 216-233, Jan. 2011.
- [44] P. Underwood, "Dynamic Relaxation", in *Computational Methods for Transient Analysis*, T. Belytschko and T. J.R. Hughes, Eds, vol. 1, chapter 5, pp. 245-265. Elsevier Science Publishers B.V., 1983.
- [45] J. Bardet and J. Proubet, "Adaptative dynamic relaxation for statics of granular materials". *Computers & Structures*, vol. 39, no. 3-4, pp. 221-229, 1991.
- [46] D. Hegyi, I. Sajtos, G. Geiszter and K. Hincz, "Eight-node quadrilateral double-curved surface element for membrane analysis". *Computers & Structures*, vol. 84, no. 31-32, pp. 2151-2158, Dec. 2006.
- [47] M. Kadkhodayan, J. Alamatian and G.J. Turvey, "A new fictitious time for the dynamic relaxation (DXDR) method". *International Journal for Numerical Methods in Engineering*, vol. 74, no. 6, pp. 996-1018, 2008.
- [48] G. Turvey, "DR large deflection analysis of sector plates". *Computers & Structures*, vol. 34, no. 1, pp. 101-112, 1990.
- [49] G. Turvey and M. Salehi, "Annular sector plates: comparison of full-section and layer yield predictions". *Computers & Structures*, vol. 83, no. 28-30, pp. 2431-2441, Nov. 2005.
- [50] M. Salehi and H. Aghaei, "Dynamic relaxation large deflection analysis of non-axisymmetric circular viscoelastic plates". *Computers & Structures*, vol. 83, no. 23-24, pp. 1878-1890, Sept. 2005.
- [51] F. Alshawi and A. Mardirosian, "An improved dynamic relaxation method for the analysis of plate bending problems". *Computers & Structures*, vol. 27, no. 2, pp. 237-240, 1987.

- [52] D. Ghelli and G. Minak, "Numerical analysis of the effect of membrane preloads on the low-speed impact response of composite laminates". *Mechanics of Composite Materials*, vol. 46, no. 3, pp. 1-18, 2010.
- [53] B. Kilic and E. Madenci, "An adaptive dynamic relaxation method for quasi-static simulations using the peridynamic theory". *Theoretical and Applied Fracture Mechanics*, vol. 53, no. 3, pp. 194-204, June 2010.
- [54] D. Oakley, "Adaptive dynamic relaxation algorithm for non-linear hyperelastic structures Part I. Formulation". *Computer Methods in Applied Mechanics and Engineering*, vol. 126, no. 1-2, pp. 67-89, Sept. 1995.
- [55] L.G. Zhang and T.X. Yu, "Modified adaptive dynamic relaxation method and its application to elastic-plastic bending and wrinkling of circular plates". *Computers & Structures*, vol. 33, no. 2, pp. 609-614, 1989.
- [56] J. Teng, "Elastic-plastic large deflection analysis of axisymmetric shells". *Computers & Structures*, vol. 31, no. 2, pp. 211-233, 1989.
- [57] P. Frieze, R. Hobbs and P. Dowling, "Application of dynamic relaxation to the large deflection elasto-plastic analysis of plates". *Computers & Structures*, vol. 8, no. 2, pp. 301-310, Apr. 1978.
- [58] M. Kadkhodayan, L.C. Zhang and R. Sowerby, "Analyses of wrinkling and buckling of elastic plates by DXDR method". *Computers & Structures*, vol. 65, no. 4, pp. 561-574, 1997.
- [59] I. Pasqualino, "A nonlinear analysis of the buckle propagation problem in deepwater pipelines". *International Journal of Solids and Structures*, vol. 38, no. 46-47, pp. 8481-8502, Nov. 2001.
- [60] H.K. Dang and M.A. Meguid, "Evaluating the performance of an explicit dynamic relaxation technique in analyzing non-linear geotechnical engineering problems". *Computers and Geotechnics*, vol. 37, no. 1-2, pp. 125-131, Jan. 2010.
- [61] M. Rezaiee-Pajand and J. Alamatian, "Nonlinear dynamic analysis by dynamic relaxation method". *Structural Engineering and Mechanics*, vol. 28, no. 5, pp. 549, 2008.
- [62] M. Rezaiee-Pajand and S.R. Sarafrazi, "Nonlinear dynamic structural analysis using dynamic relaxation with zero damping". *Computers & Structures*, vol. 89, no. 13-14, pp. 1274-1285, May 2011.
- [63] J.R. Kommineni and T. Kant, "Pseudo-transient large deflection analysis of composite and sandwich shells with a refined theory". *Computer Methods in Applied Mechanics and Engineering*, vol. 123, no. 1-4, pp. 1-13, 1995.

- [64] S. Qiang, "An adaptive dynamic relaxation method for nonlinear problems". *Computers & Structures*, vol. 30, no. 4, pp. 855-859, 1988.
- [65] L.C. Zhang, M. Kadkhodayan and Y.W. Mai, "Development of the maDR method". *Computers & Structures*, vol. 52, no. 1, pp. 1-8, 1994.
- [66] C. Geuzaine and J.-F. Remacle, "Gmsh reference manual". *A Finite Element Mesh Generator with Built-in Pre-and Post-Processing Facilities*, vol. 79, no. 11, pp. 1309-1331, 2006.
- [67] http://kleger.univ-ubs.fr/Herezh/attachments/2/benchmark_mesh.zip
- [68] <http://www.gom.com/metrology-systems/system-overview/aramis.html>
- [69] ARAMIS User Manual - Software. Gom, 2007.
- [70] http://www.photron.com/index.php?cmd=product_general&product_id=7
- [71] H. Laurent, "Etude en grandes transformations d'une nouvelle famille d'éléments finis coque triangulaire à trois degrés de liberté par noeud. Application à la simulation numérique de l'emboutissage". Thesis, Université de Bretagne Sud, 1996.
- [72] H. Laurent, G. Rio, "Formulation of a thin shell finite element with continuity C^0 and convected material frame motion". *Computational Mechanics*, vol. 27, no. 3, pp. 218-232, 2001. ISSN 0178-7675.
- [73] S. Adanur, "Handbook of Weaving - Fabric Structure, Properties and Testing". Pp. 361-373. Sulzer Textil Limited Switzerland, 2001.
- [74] J. Hu, "Fabric testing". Woodhead Publishing Limited, 2008.
- [75] V. Quaglini, C. Corazza, C. Poggi, "Experimental characterization of orthotropic technical textiles under uniaxial and biaxial loading". *Composites Part A: Applied Science and Manufacturing*, vol. 39, no. 8, pp. 1331-1342, 2008.
- [76] NORME INTERNATIONALE ISO 1421:1998(F). Supports textiles revetus de caoutchouc ou de plastique - Détermination de la force de rupture et de l'allongement à la rupture.
- [77] B. Dauda, S. Olutunde Oyadiji, P. Potluri, "Characterising mechanical properties of braided and woven textile composite beams". *Applied Composite Materials*, vol. 16, pp. 15-31, 2009.
- [78] S. Thuillier, P. Manach, "Comparison of the work-hardening of metallic sheets using tensile and shear strain paths". *International Journal of Plasticity*, vol. 25, no. 5, pp. 733-751, 2009.

- [79] Julien Troufflard. "Simulation du comportement d'un homme à la mer muni d'un gilet de sauvetage gonflable". Rapport de stage DESS/DEA.
- [80] Wikipedia. <http://en.wikipedia.org>
- [81] Gmsh website. <http://geuz.org/gmsh/>
- [82] David Jou and Josep Enric Lebot. "Fisica para ciencias de la vida".
- [83] Deborah Roche. "Guidelines for Athlete Assessment in New Zealand Sport. Flexibility and muscle balance assessment"
- [84] Franck Multon, "Controle du mouvement des humanoïdes de synthèse". Thesis, Université de Rennes 1, France, 1998.
- [85] L. Nedel, D. Thalmann, "Modeling and deformation of the human body using an anatomically-based approach". Computer Animation 99, Proceedings, p. 34-40, Philadelphia, Pennsylvania, 1998.
- [86] L. Porcher Nedel, "Simulating virtual humans", Simposio brasileiro de computação gráfica e processamento de imagens, Rio de Janeiro, 1998.
- [87] C. Oliver, A. Cruz, "Introduction to biomechanics and kinesiology", UP Manila-College of Allied Medical Professions, 1998.
- [88] W.S. Erdmann, "Geometric and inertial data of the trunk in adult males", Journal of biomechanics, vol. 30, no. 7, pp. 679-688, 1997.
- [89] H. Veeger, B. Yu, K. An, "Parameters for modeling the upper extremity". Journal of biomechanics, vol. 30, no. 6, pp. 647-652, 1997.
- [90] V. Zordan, J. Hodgins, "Tracking and modifying upper-body human motion data with dynamic simulation". Computer animation and simulation 99, 1999.
- [91] R. Willinger, H. Kang, B. Diaw, "Développement et validation d'un modèle mécanique de la tête humaine". Comptes Rendus de l'Académie des Sciences de Paris, Série II b, pp. 125-131, 1999.
- [92] J. Park, D. S. Fussel, "Forward dynamics based realistic animation of rigid bodies". Computers and Graphics, vol. 21, no. 4, pp. 483-496, 1997.
- [93] L. Dekker, I. Douros, B. Buston, "Building symbolic information for 3D human body modeling from range data". Second International Conference on 3D Digital Imaging and Modeling, Ottawa, Canada, 1999.
- [94] A. Savenko, S. Jan, G. Clapworthy, "A biomechanics-based model for the animation of human locomotion". Montfort University, Milton Keynes, UK, 1999.

- [95] G. Andreoni, C. Rigotti, G. Baroni et al., "Quantitative analysis of neutral body posture in prolonged microgravity". *Gait and Posture*, vol. 12, no. 3, pp. 235-242, 2000.
- [96] A. Maciel, L. Nedel, C.M. Dal Sasso Freitas, "Anatomy-based joint models for virtual humans skeletons". *Brasil Computer Animation, Conference Proceedings*, 2002.
- [97] B. Allen, B. Curless, Z. Popovic, "The space of human body shapes: reconstruction and parameterization from range scans". *ACM SIGGRAPH 2003*, San Diego, USA, 2003.
- [98] K. Choi, H. Ko, "Research problems in clothing simulation", *Computer-aided design*, vol. 37, no. 6, pp. 585-592, 2005.
- [99] A. Perez del Palomar, B. Calvo, J. Herrero et al., "A finite element model to accurately predict real deformations of the breast". *Medical engineering and physics*, vol. 30, no. 9, pp. 1089-1097, 2008.
- [100] F. Oshita, K. Omori, Y. Nakahira, "Development of a finite element model of the human body", *7th International LS-DYNA Users Conference*, vol. 14, no. 2, pp. 205-212, 2002.
- [101] A. Baca, "Precise determination of anthropometric dimensions by means of image processing methods for estimating human body segment parameter values". *Journal of biomechanics*, vol. 29, no. 4, pp. 563-567, 1996.
- [102] A. Tilley, Henry Dreyfuss Associates, "The measure of man and woman: human factors in design, Volume 1". Ed. John Wiley and Sons, Inc, 2002.
- [103] I. Watanabe, "Development of practical and simplified human whole body FEM model". *JSAE Review*, vol. 22, no. 2, pp. 189-194, 2001.
- [104] J. Delotte, M. Behr, L. Thollon et al., "Femme enceinte et accidentologie routiere: interet de l'approche numerique. Application a un choc frontal au troisieme trimestre de la grossesse avec analyse de l'effet de la ceinture de securite". *Journal de gynecologie obstetrique et biologie de la reproduction*, vol. 36, no. 6, pp. 577-581, 2007.
- [105] B. Kayis, P. Iskander, "A three-dimensional human model for the IBM/CATIA system". *Applied Ergonomics*, vol. 25, no. 6, pp. 395-397, 1994.
- [106] J. Gourret, N. Magnenat-Thalmann, D. Thalmann, "Modeling of contact deformations between a synthetic human and its environment". *Computer Aided Design*, vol. 23, no. 7, pp. 514-520, 1991.
- [107] E. Haug, H. Choi, S. Robin et al., "Human models for crash and impact simulation". *Handbook of Numerical Analysis*, Vol. XII, pp. 231-452.

- [108] R. Comolet. "Mécanique expérimentale des fluides" Tomes I et II. 4ème édition. Ed. Masson.
- [109] Etienne Guyon, Jean-Pierre Hulin, Luc Petit. "Hydrodynamique physique". Savoirs actuels, InterEditions/Editions du CNRS.
- [110] Added mass. <http://everything2.com/title/Added+mass>
- [111] James Mark Oliver. "Water entry and related problems". Thesis submitted for University of Oxford, 2002.
- [112] A. Carcaterra, E. Ciappi. "Hydrodynamic shock of elastic structures impacting on the water: theory and experiments". Journal of sound and vibration. Elsevier, February 2003.
- [113] G. De Backer, M. Vantorre, C. Beels, J. De Pré, S. Victor, J. De Rouck, C. Blommaert, W. Van Paepegem. "Experimental investigation of water impact on axisymmetric bodies". Applied Ocean Research. Elsevier, July 2009.
- [114] Adrian Constantinescu. "Modélisation 2D de l'impact d'une structure sur l'eau. Initiation de l'endommagement". Thesis for Université de Bretagne Occidentale, 2006.
- [115] Nicolas Malleron. "Contribution à l'étude des interactions fluide-structure pour l'analyse de l'impact hydrodynamique d'un système de flottabilité d'hélicoptère". Thesis for Université d'Aix-Marseille, April 2009.
- [116] Bagnold R., "Interim report on wave pressure research", J. Ind. Civil Eng., Vol. 12, 1939.
- [117] R. Comolet. "Mécanique expérimentale des fluides" Tomes I et II. 4ème édition. Ed. Masson.
- [118] Edward J. Shaughnessy Jr, Ira M. Katz, James P. Schaffer. "Introduction to Fluid Mechanics". Oxford University Press.
- [119] Anderson. "Fundamentals of aerodynamics". Ed. Mc Graw-Hill.
- [120] Etienne Guyon, Jean-Pierre Hulin, Luc Petit. "Hydrodynamique physique". Savoirs actuels, InterEditions/Editions du CNRS.
- [121] Clayton T. Crowe, Donald F. Elger, John A. Roberson, Barbara C. Williams. "Engineering fluid mechanics". 9th Edition.
- [122] Frank M. White. "Fluid Mechanics". WCB McGraw-Hill, Fourth Edition.
- [123] Wikipedia. www.wikipedia.org
- [124] T. Von Karman, "The impact on seaplane floats during landing". NACA TN, vol. 321, pp. 2-8, 1929.

- [125] N. Malleron, Y. Scoln, A. Korobkin, "Some aspects of a generalized Wagner model". 22nd IWWFEB, Plitvice, Croatia 2007.
- [126] E. Onate, F. Flores, "Advances in the formulation of the rotation-free basic shell triangle". Computer Methods in Applied Mechanics and Engineering, vol. 194, no. 21-24, pp. 2406-2443, 2005.
- [127] P. Wriggers, "Computational contact mechanics". Springer Verlag, 2006.
- [128] S. Sicklinger, "Formulation and object-oriented implementation of a nonlinear node-to-surface mechanical contact algorithm". Master's Thesis, Technische Universitat Munchen, 2010.
- [129] D. Zhang, "Cloth simulation using multilevel meshes". Computers and Graphics, vol. 25, no. 3, pp. 383-389, 2001.

Annexes

Appendix A: Calculation of radius and thickness of a inflated sphere by means of Scilab

```
//RADIUS AND THICKNESS RESOLUTION

//Variables initialization
r = 300;
nu = 0.41;
P = 0.01;
e = 0.27;
E = 150;

//The new radius after deformation will be denoted as r2 (initial value r)
r2 = r;
//The new thickness will be denoted as e2 (initial value e)
e2 = e;

//Definition of a epsilon for the error (looking for a good precision)
tol = 10**(-12);

//Definition of a maximum number of iterations (in case of divergence)
nmax = 100;

//Radius error verification variable initialisation
v1 = 1;
//Thickness error verification variable intialisation
v2 = 1;

//Counter initialisation
n = 0;

//Definition of the values X(i) initially:
Xi = [r ; e];
```

```

//Definition of a vector to check the precision by the residual and
//initialization of the variable containing its maximum value
deltaXi = [0. ; 0.];
maxresidu = 1000000;

//Calculate all in this boucle. Do it while the error in radius and thickness
//is superior to our epsilon, the iteration number is inferior to the
//stablished max and the relative residual is superior to the specified
//tolerance

while (maxresidu > tol & v1 > tol & v2 > tol & n < nmax),

    //Definition of rigidity matrix:
    K = -[ ((r**2)/(r2**3))-((1-nu)*P)/(2*e2*E), ((1-nu)*P*r2)/(2*E*e2**2) ;
          -(P*nu)/(E*e2), -e**2/e2**3 + (P*nu*r2)/(E*e2**2)];

    //Calculation of the inverse of matrix K:
    Kinv = inv(K);

    //Definition of residual
    R = [(1/2)-((r**2)/(2*r2**2))-((1-nu)*P*r2)/(2*e2*E) ;
          ((e**2)/(2*e2**2))-((P*nu*r2)/(E*e2))+(0.5*P/E - 1/2)];

    //Calculation by Newton of the new values X(i+1) of radius and thickness:
    deltaXi= Kinv*R;
    Xi = Xi + deltaXi;

    //Verification of precision using the values stored in vector Xi:
    v1 = abs(deltaXi(1,1)/Xi(1,1));
    v2 = abs(deltaXi(2,1)/Xi(2,1));

    //Iteration number increment
    n=n+1;

    //Assignment of new values for radius and thickness to continue iterating
    r2 = Xi(1,1);
    e2 = Xi(2,1);

    //Relative residual calculation for stopping criterion
    maxresidu = abs (max(R))/r;

```

```
end;
```

```
//Display of results:  
disp('Final solution of [r2; e2]:');  
Xi
```



TEXTANE A/B 210 (240 g) XF

Temporary data sheet

product manufactured and tested in compliance with en 393+396 and 399. "In any case, the above mentioned fabric remains subject to test and checks as requested for the verification of the strength of inflatable life jackets and personal buoyancy aids"

1 - MATERIALS		
INNER COATING	PU ether 100% (extrusion process) hydrolysis, low temperatures and hydrocarbons resistant low gas permeability	weight $\geq 110 \text{ g/m}^2$
ADHESIVE	PU ether 100% (spreading process) hydrolysis, low temperatures and hydrocarbons resistant	weight $\geq 10 \text{ g/m}^2$
FABRIC	Nylon 100% width $150 \pm 2 \text{ cm}$ rubbing dry and wet ISO 105 X 12 1987 minimum class 3 - test in process sea water resistance ISO 105 E02 1989 minimum class 4 - test in process	warp ends $27/\text{cm} \pm 2 \text{ cm}$ weft picks $21/\text{cm} \pm 2 \text{ cm}$
TOTAL WEIGHT		$240 \pm 7\% \text{ g/m}^2$

2 - TECHNICAL DATA	VALUES	VALUES
BREAKING STRENGTH ISO 1421 CRT 4.3.2.e	warp $\geq 1000 \text{ N/5cm}$	weft $\geq 750 \text{ N/5cm}$
BREAKING STRENGTH WET 1 DAY ISO 1421 CRT 4.3.2.f	warp $\geq 850 \text{ N/5cm}$	weft $\geq 600 \text{ N/5cm}$
ELONGATION AT BREAK ISO 1421 CRT 4.3.2.g	warp • 60%	weft • 60%
ELONGATION AT BREAK WET 1 DAY ISO 1421 CRT 4.3.2.h	warp • 60%	weft • 60%
DOUBLE TONGUE TEAR ISO 4674 METHOD A1	warp $\geq 40 \text{ N}$	weft $\geq 36 \text{ N}$
COATING ADHESION (RF WELD) FILM TO FILM ISO 2411	$\geq 150 \text{ N/5 cm}$	
COATING ADHESION (RF WELD) FILM TO FILM WET 14 DAYS - 70 C° ISO 2411	$\geq 50 \text{ N/5 cm}$	
RESISTANCE TO FLEXING ISO 7854 METHOD A	Test in process	

* Please note that listed values are "typical (average) values"

SO.L.TER. s.r.l.

Via Massari Marzoli, 7 bis - Zona Industriale sud ovest - 21052 Busto Arsizio (VA) - Italy
Tel. +39 0331 341913 - Fax +39 0331 341921 - info@solter.it